Doctoral Dissertation

Synthesis and Application of Covalent Organic Frameworks (COFs) and COF Derived Carbons

Chao Yang

Supervisor: Shinya Maenosono

Graduate School of Advanced Science and Technology
Japan Advanced Institute of Science and Technology
(Materials Science)

September 2019

Abstract

As an emerging class of ordered conjugated organic polymer materials, covalent organic frameworks (COFs) possess many unique properties such as predictability, inherent porosity, structural periodicity, large surface area, and high stability. The design and synthesis of COFs are based on the reticular chemistry and geometry of building blocks, which play a very significant role on the formation, topology and porosity of COF. Due to simultaneous polymerization and crystallization, it is key to keep the balance between dynamic error correction and non-covalent interlayer interaction. In this regard, the linkers in 2D COFs via [3 + 2], [3 + 3], [4 + 2] or [6 + 2] pathways should be small molecules in order to tune the free movement of monomers as well as thermodynamic and kinetic of system. However, forming 2D COFs via [4 + 4] pathway in the solution phase remains a big challenge when both of building units are tetrafunctional so that they can not twist or bend in a large range like bi- or tri-functional building blocks. On the other hand, stable and porous 1D COFs have not been reported due to the lack of relevant knowledges of controlling the covalent interaction and non-covalent interaction. However, tuning the dimension is an important and fundamental issue because 1D nanostructures always exhibit a distinct property with their 2D or 3D counterparts. In addition, owing to the thermal stability and designable heteroatoms, COFs also might be ideal precursors for metal-free carbon nanomaterials as electrocatalysts.

In this thesis, various 2D [4 + 4] COFs and 1D COFs were synthesized and characterized by Fourier transform infrared (FT-IR), solid-state NMR, powder X-ray diffraction (PXRD), high resolution transmission electron microscope (HR-TEM), X-ray photoelectron spectra (XPS), nitrogen sorption, computing simulation and so on.

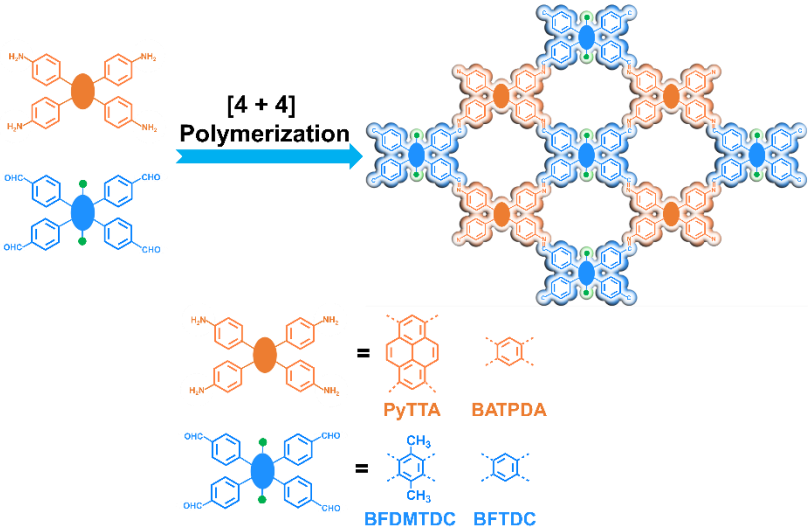

Scheme 1. Schematics for the synthesis of 2D [4 + 4] COFs.

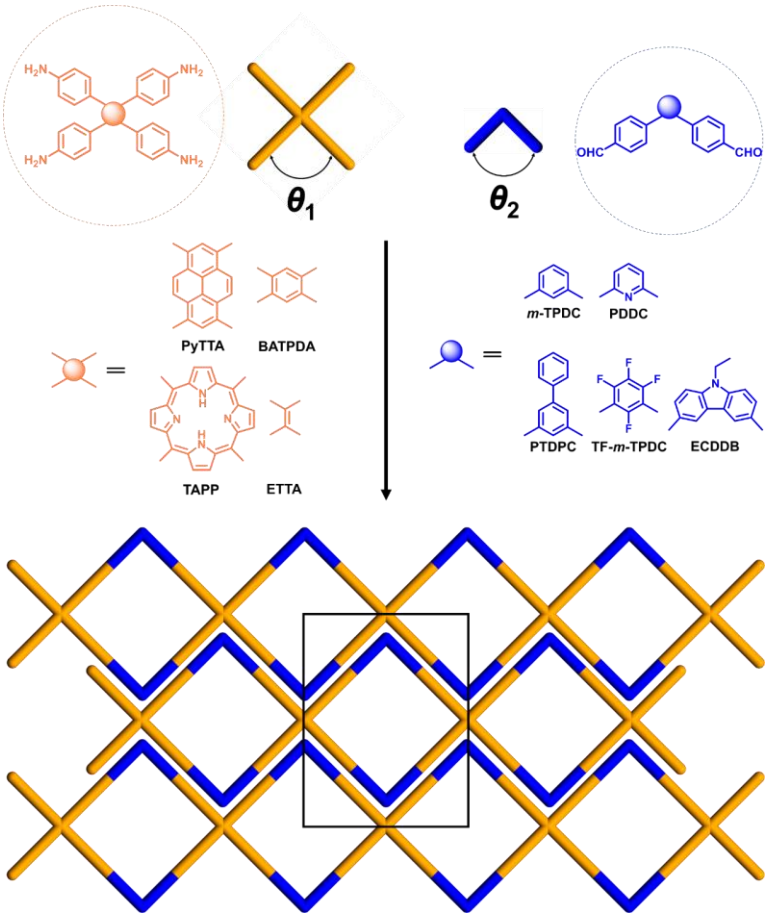

Scheme 2. A general designing strategy of 1D COFs.

2D [4 + 4] COFs were successfully synthesized in solvothermal method. Due to the good matching between building blocks, trade off between interlayer interaction and crystallization, and special connection patyway, high porosity (BET surface areas:

650~1100 m^2 g^{-1}) and micropores (~1 nm) can be achieved. In addition, methyl groups can be decorated to modify the pore surface of 2D [4 + 4] COFs.

Moreover, 1D COFs were first reported. By designing a series of bifunctional V-type linkers to combine with tetragonal knots, the covalent extension is limited in only one direction. These microporous 1D COFs are very designable since they can be modified by various heteroatoms and functional groups and tuned by the angle of building blocks. Due to the high microporosity, 1D COF exhibits a good performance for CO_2 separation.

2D [4 + 4] COFs also exhibit good performances for CO_2 capture. Methyl group decorated COFs achieve an enhanced capture (100 mg g^{-1}) and separation (w/w, 26/1, CO_2 over N_2) of CO_2 at 1 atm and 273 K due to the increased microporosity and the strong affiliation between COFs and CO_2 induced by methyl groups.

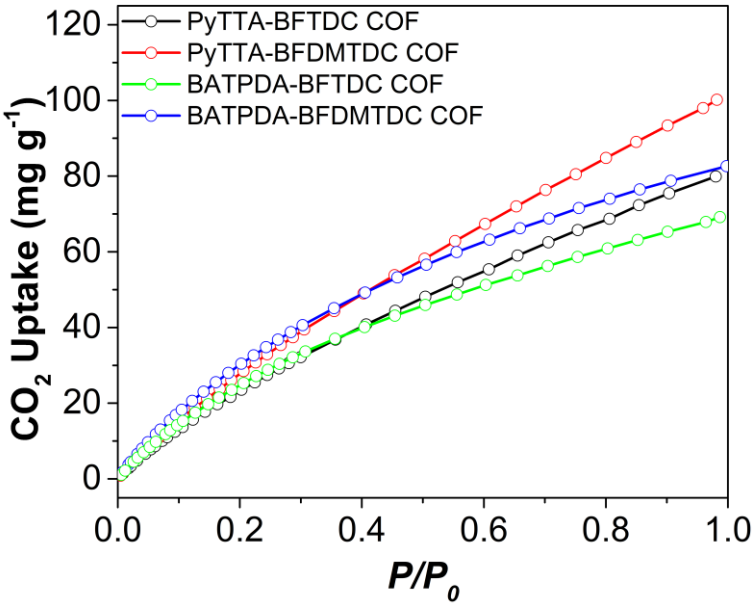

Scheme 3. CO_2 uptake curves at 273 K for 2D [4 + 4] COF.

Porous and metal-free N,P co-doped carbons via carbonizing and phosphorizing 2D [4 + 4] COFs and TAPB-DMTA COF exhibit remarkable performances as ORR/HER electrocatalysts with the half-wave potential of 0.81 V vs. RHE in alkaline medium and overpotential of 260 mV at 10 mA cm^{-2} in acid medium.

Various 2D and 1D COFs were designing and successfully synthesized under solvothermal conditions mainly considering the geometry, angle, functional group and symmetry of building blocks. The topology, dimension and pore surface can be tuned

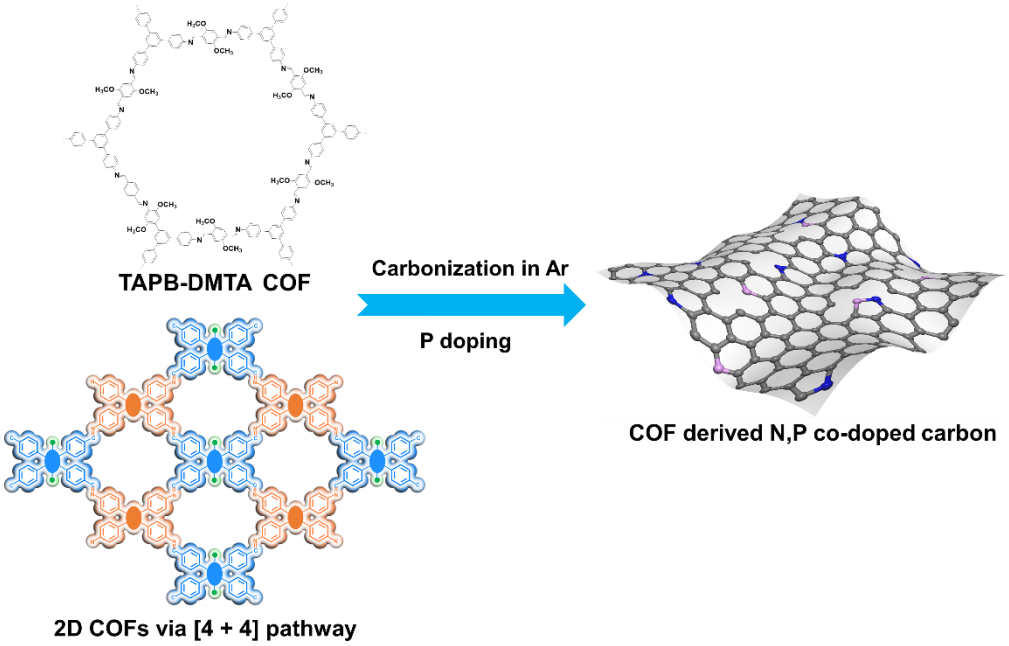

Scheme 4. Fabrication process of 2D COF derived N,P co-doped carbon.

controllably. Especially, the finding of 1D COFs will overturn the traditional view that COFs are 2D and 3D rather than 1D. This will much enrich the diversity of COFs and promote the development of chemistry of COFs. Moreover, microporous 2D [4 + 4] COFs with methyl groups and 1D COFs show a good performance for CO_2 capture and separation, suggesting the promising prospect of these COFs and the effect of methyl groups for CO_2 application. On the other hand, the remarkable electrochemical performance of N,P co-doped carbons derived from 2D COFs will open a new way to synthesize high-performance metal-free electrocatalysts and broaden the application of emerging COF-derived carbons.

Keywords: Covalent organic frameworks; Topology; CO_2 capture; Dimension; Doped carbon.

Contents

Chapter I: Introduction

1. General description of the areas of concern

The development of human society's history is essentially the history that human use, discovery and create various materials continuously. Stone, bronze and iron become the main materials of tools for the stone age, bronze age, and iron age, respectively. Therefore, developing of a kind of new materials always means the start of a new stage of human society. For nowadays, someone regard it as the silicon age because clips consisting of silicon become indispensable parts of mobile phones, computers, scientific instruments and soon on. Some others think it is the polymer age as the result of various plastic and rubber products here and there. It is controversial to say which material is the most important, but various advanced materials indeed make our life more and more convenient, efficient, safe, and colorful. With the demand of human beings increasing and the natural resources consumed faster and faster, more advanced materials with various functions need to be developed.

Among these materials, porous materials have great importance in the production of modern industry and everyday life. For example, activated carbon with a high specific area is often used to absorb the contained organic compound in sewage treatment plants. And in fact, the human skeleton consists of more than two hundred porous bones. There are so rich various pores in these bones that the human skeleton is light-weight.

Based on the definition of IUPAC, porous materials can be classified into three categories according to pore diameter: those with pore diameters less than 2 nm are microporous; pore sizes between 2 and 50 nm are mesoporous; and pore diameters greater than 50 nm are macroporous. [1]

Porous metals, [2] metal oxides [3] and hydroxides, [4] zeolites, [5] porous carbon materials, [6] conjugated microporous polymers (CMPs), [7] polymers of intrinsic microporosity (PIMs), [8] porous organic cages, [9] porous liquids, [10] covalent organic frameworks (COFs), [11] metal-organic frameworks (MOFs) [12] have been paid much attention due to their unique properties on the structure and function. These porous materials have great potential in

many applications, such as gas separation and storage, molecular sieves, heterogeneous catalysts or catalyst supports, sensing, drug delivery, and energy storage and conversion. [13-16] Their advantageous properties include large surface areas, controllable pore sizes, surface functionalities, and tunable compositions.

2. Background

Crystalline porous polymers are a class of unique materials that possess periodic ordered structures and well-defined pores. Similar with other polymers such as biopolymers, universal linear polymers and hyper-branched polymers, in these crystalline porous polymers, each unit is linked by covalent bonds or coordinated bonds. [17-20] What make crystalline porous polymers unique is their precisely high-ordered structures in molecule along with micro- and/or meso- porosities, which are hardly achieved in other amorphous polymers.

Among crystalline porous polymers, COFs are a kind of typical materials explored very well. COFs are built up from organic units (building blocks) with strong covalent bonds. [21] The structure and pore size can be predesigned according to the reticular topology, different from those of amorphous polymers and inorganic porous materials. Therefore, the linking units and bonds formed between those units upon reticulation are so various that the type of COFs reach several hundred, indicating their tremendous structural diversity and tunability. Due to the unique properties such as large specific surface area, robust stability and ordered pore size, COFs are applied in various fields like gas storage, catalysts and ion conduction. [23-27]

2.1 COFs

2.1.1 Reaction and geometry

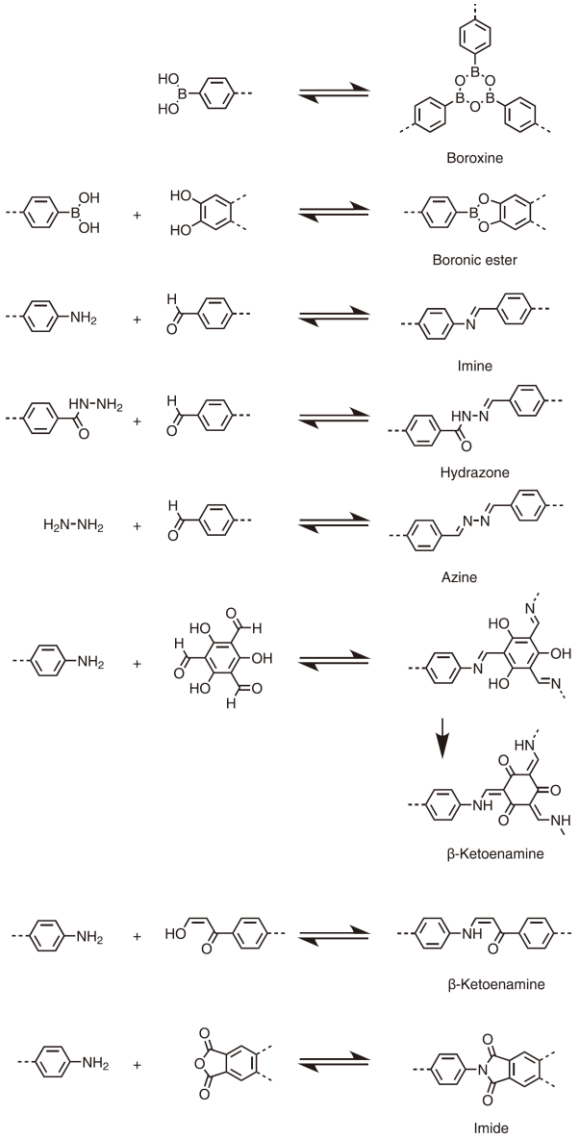

Figure 1. Chemical reactions used to synthesize COFs. [27]

Different from MOFs, reversible condensation reactions are necessary to form a crystalline structure for COFs. They enable the lattice to be repaired and rearranged repetitively to reach the final equilibrium. [28] A variety of linkage by different reactions have been successfully applied in the formation of COFs to date such as boronate ester, boroxine and borazine, imine, hydrazone, azine, imide, and so on as shown in **Figure 1**.

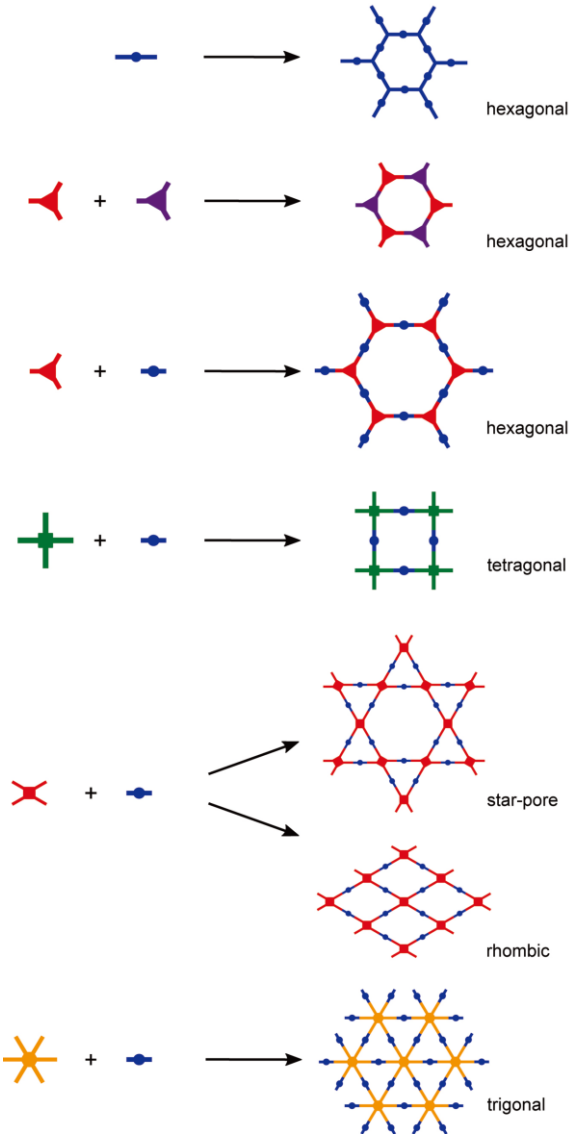

Figure 2. Design principle of COFs based on different topology diagrams. [27]

As mentioned above, the structure of COFs depends on the geometry and connectivity of the linkers. Compared with 3D COFs, 2D COFs are stacked by 2D layers. In each layer, the structure of a COF lattice is predetermined by the geometry and planar or approximately planar linkers co-condense to connect with each other into sheets with trigonal, tetragonal or hexagonal pores as shown in **Figure 2**. Whereas, 3D COFs are created from three-dimensional building blocks into ordered 3D networks.

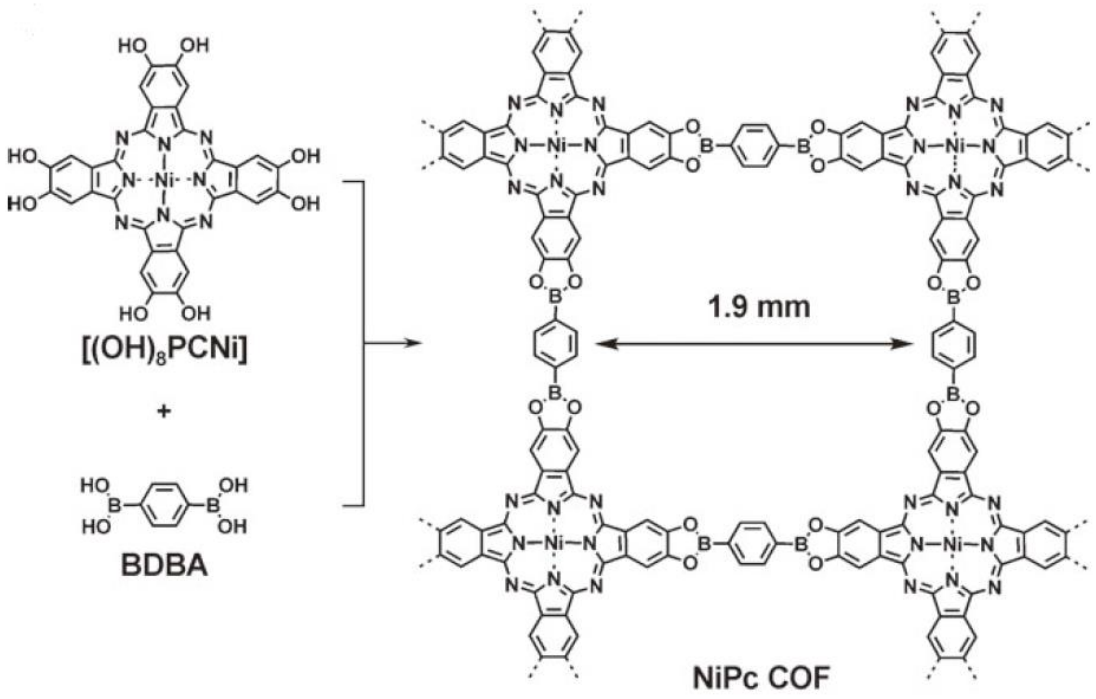

Figure 3. The synthesis of the nickel phthalocyanine covalent organic framework (NiPc COF) by a boronate esterification reaction. [29]

Unlike 3D COFs, in 2D COFs, a crystalline structure is formed only through noncovalent interactions in a direction. Large polycyclic aromatic cores such as porphyrins and pyrenes, which have a strong preference to stack in molecular crystals are beneficial to adjust the layer stacking (**Figure 3**). [29,30] Despite some slipped-stacking and staggered arrangements between layers can be formed by using knots and linkers whose special conformations can prevent eclipsed stacking of layers, eclipsed stacking order is common and can be induced through various interlayer interaction such as π-π, dipole-dipole and arene-perfluoroarene. [31-33]

Although some irreversible reactions can be used to form a COF by introducing strong stacking interactions to reduce the type and number of defects to an extent or using harsh, high-temperature crystallization conditions, [34,35] most syntheses of COFs from linkages are functionally reversible. Since the polymerization and crystallization happen simultaneously, these more reversible reactions provide additional dynamic error correction, making the thermodynamic minimum of that system more accessible. [36] In most cases, building blocks and target linkages should be conformationally flexible to ensure the freedom during the crystallization. In this view, one or both building blocks in COFs via [2 + 2], [3 + 2], [4 + 2]

and [6 + 2] pathway are small and flexible to guarantee their movement during nucleation and growth processes. [37] However, for 2D [4 + 4] COFs, it is hard to control the balance between the interlayer interaction and dynamic reversibility especially when two building blocks both have larger aromatic cores. Even though 2D single-layered COFs with four-fold symmetry via on-surface polymerization have been synthesized successfully, [38,39] forming 2D COFs via [4 + 4] pathway in the solution phase remains a big challenge.

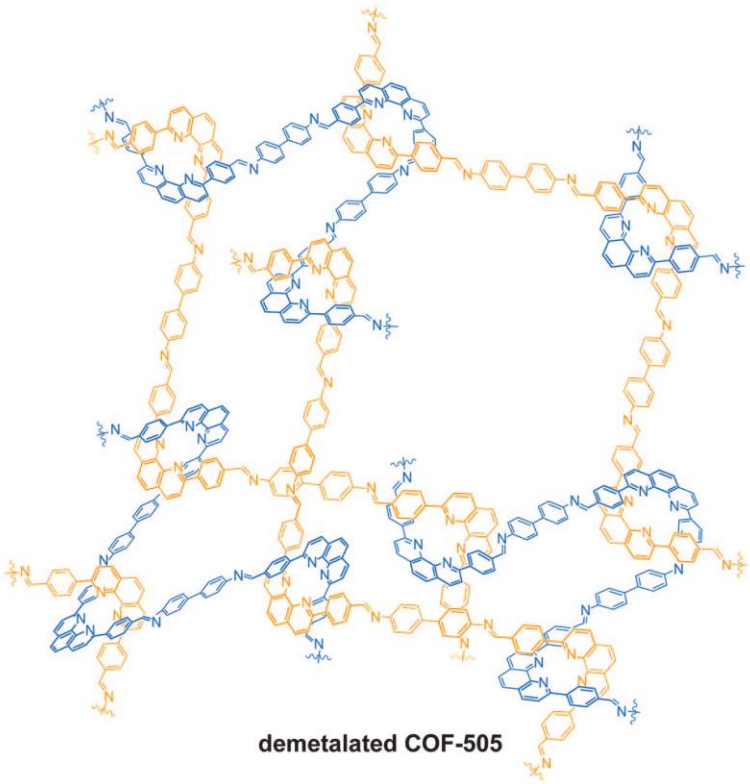

Figure 4. Demetalated COF-505 was constructed from organic threads using copper(I) as a template and subsequently demetalated. [40]

Besides 2D and 3D COFs, the ordered weaving of 1D threads can formed a COF with an extended 3D network. [40,41] Here, we need to realize the fact that non-covalent interaction plays a key role on the formation of COFs. For example, π-stacking enable the position of layers to be restricted with respect to each other and minimize stacking disorder. However, for COF-505, these structures are held together by metal-coordination interaction with each other so that the COF is flexible when the templates are removed. Therefore, the crystallinity, surface area and stability of COF-505 and demetalated COF-505 are much poor. On the other hand, 1D nanostructures always exhibit a distinct property with their 2D or 3D counterparts. For example, 2D graphene is highly conductive with a band-gap of

zero, while 1D graphene nanoribbons is semiconductive with a topologically induced band. [42-44] Therefore, synthesis of 1D COFs with high crystallinity, surface area and stability is very important to figure out fundamental issues such as the connectivity, topology and property of COFs.

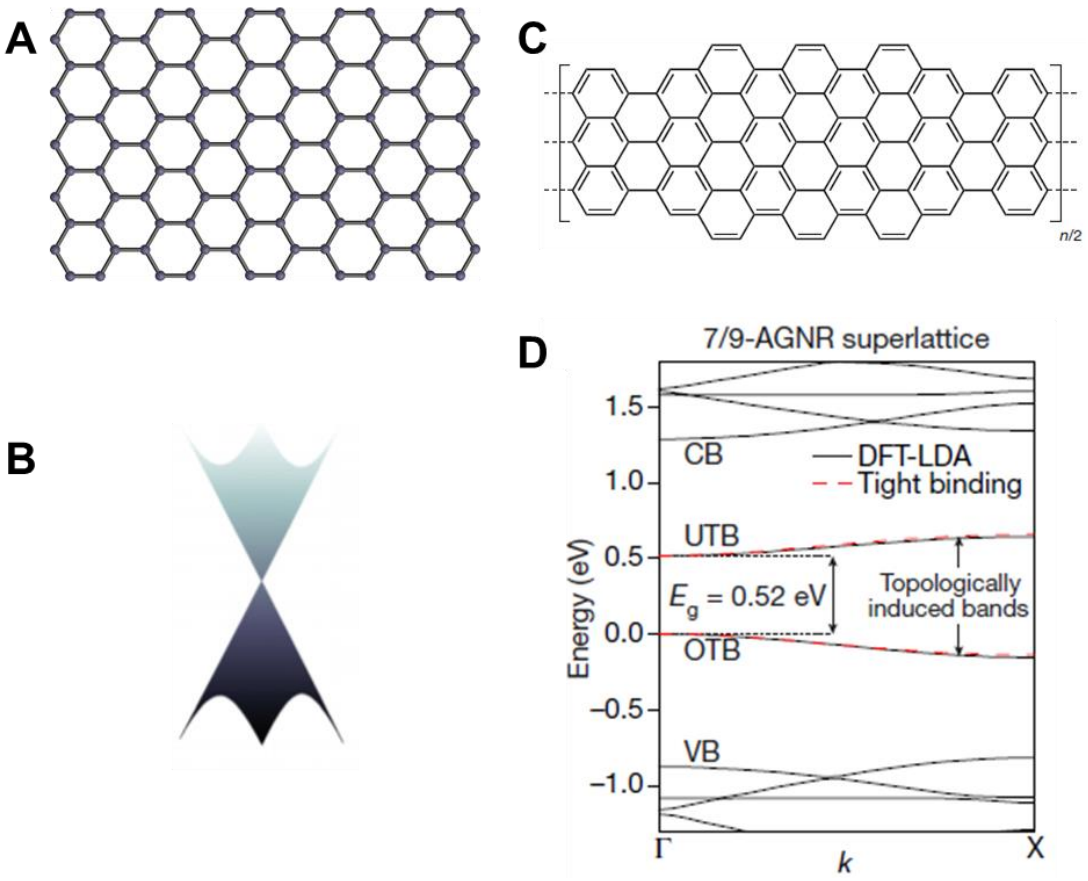

Figure 5. (A) Graphene and (B) the band structure of graphene; (C) 7/9-armchair graphene nanoribbon (AGNR) superlattice and (D) its band structure. [43,44]

Nevertheless, for some unknown COFs, extensive efforts are necessary to be applied to screen various synthetic conditions including linkers, solvent mixtures, temperature and reaction time because these factors are much relative with the reaction and reversibility.

2.1.2 Synthetic methods

2.1.2.1 Solvothermal synthesis

Most COFs are synthesized under solvothermal environment where reversible bond formation is possible without resorting to extreme temperatures or pressures. And this method to date is still the most popular and most frequently applied synthesis method for

COF formation. In practice, the small molecular byproduct such as water has limited solubility in high boiling solvents. [14] The kinetic can be controlled by adjusting the pressure in the vessel, temperature, time and additional component, leading to different crystallinity. Mesitylene, 1,4-dioxide, *o*-dichlorobenzene, *n*-butyl alcohol, benzyl alcohol, dimethylformamide, isoquinoline and N-methyl-2-pyrrolidone are common solvents for COF formation. Generally, COFs have been prepared at temperatures ranging between 60–200 °C, depending on solvents and reactants. For example, COF-1 was prepared from 1,4-benzene diboronic acid (BDBA) in mesitylene/ dioxane (1:1) at 120 °C for 3 days. [45] And PI-COF-1 was made from PMDA and TAPA in mesitylene/NMP/isoquinoline (1:1:0.1) at 200 °C for 5 days. [46] In most cases, the COF product via solvothermal method exhibits higher crystallinity and BET surface area than that in other ways. However, it remains a big challenge to achieve a scale-up synthesis via solvothermal method due to the slow reaction rate and high requirement on the equipment and reaction condition.

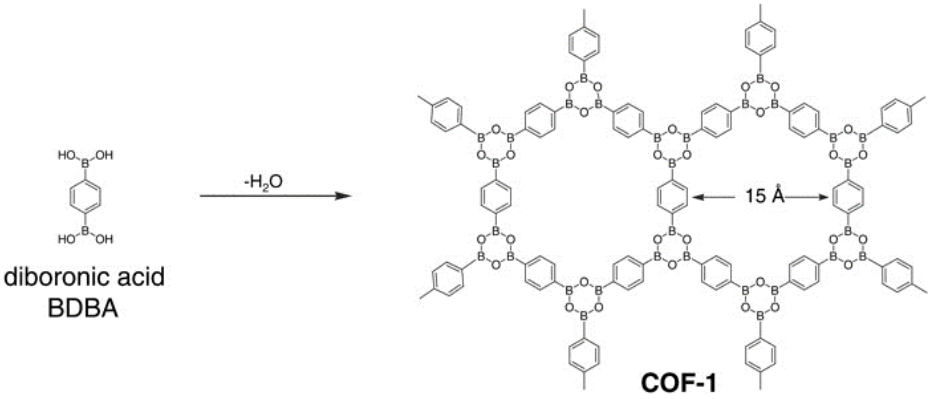

Figure 6. Self-condensation of diboronic acid to form COF-1. [45]

2.1.2.2 Microwave synthesis

In order to overcome the relatively long reaction times of the solvothermal synthesis, microwave irradiation is used to accelerate the synthesis of COFs. By microwave, specific materials for example solvent with dielectric properties absorb microwave energy and convert it into heat. However, other common solvents without a permanent dipole moment such as carbon tetrachloride, benzene, and dioxane are more or less microwave transparent. [47] Up to now, microwave method has been successfully used for the preparation of various COFs. For instance, Campbell *et al.* demonstrated microwave-

assisted COF-5 in only 20 min yielded a higher BET surface area than the that via solvothermal synthesis. [48]

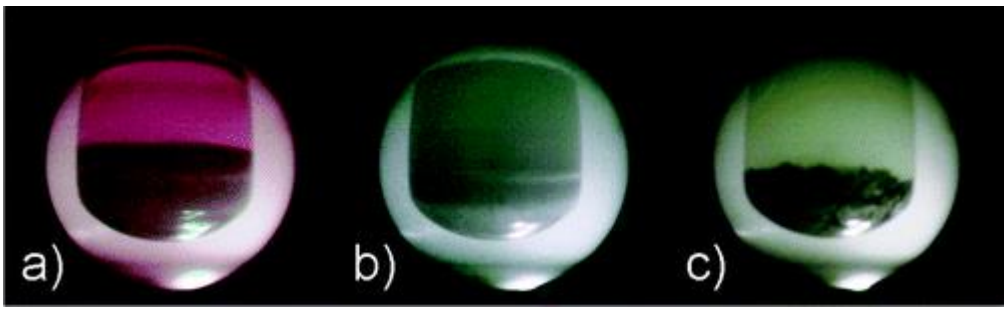

Figure 7. Digital camera images recorded from the observation port of the microwave reactor showing COF-5 reaction and purification: (a) gray-purple COF-5 powder formed after initial synthesis; (b) removal of trapped HHTP-oxidation impurities by microwave extraction process (acetone); (c) second microwave extraction results in purified gray COF-5 powder. [48]

2.1.2.3 Mechanochemical synthesis

Compared with solvothermal and microwave method, mechanochemical synthesis seems more environmentally friendly because it can be finished without any or with a small amount of organic solvents in the simple experimental devices, where the monomers are ground with mortar and pestle or ball mill. However, the low reaction rate often leads to amorphous or poorly crystalline structures. In general, monomer with more activity, additional heat or recrystallization will be helpful to increase the quality of COFs. For instance, the mechanochemical method was used to successfully synthesize TpPa-1 (MC) and TpPa-2 (MC) from high-active 1,3,5-triformylphloroglucinol (Tp), but the BET surface areas are less than 100 m^2 g^{-1}, much lower than those of the counter synthesized solvothermally. [49]

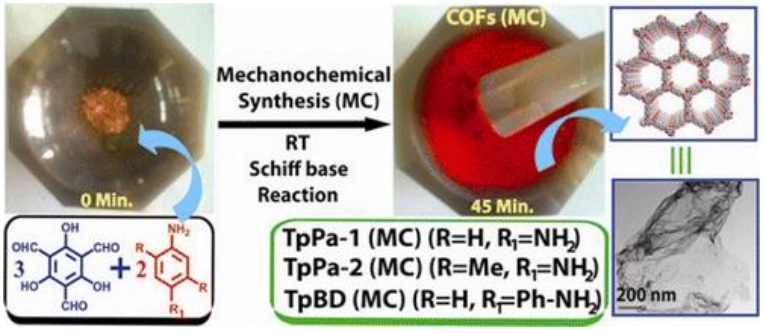

Figure 8. Isoreticular covalent organic frameworks (COFs) were synthesized via room-temperature solvent-free mechanochemical grinding. [49]

2.1.2.4 On-surface synthesis

Single-monolayered COF (sCOF) crystals are attractive because they are helpful to explore the intrinsic properties and potential applications of COFs. However, solvothermal synthesis and other methods can only produce bulk powders. By contrast, on-surface polymerization has been demonstrated to be effective for sCOF synthesis. Substrates such as metal (Ag, Cu, and Au), highly oriented pyrolytic graphite (HOPG) and graphene are often used as catalysts for carbon–carbon coupling reactions such as Ullmann coupling and Glaser coupling. [50] The interface interaction between substrate plays an important role on growth and orientation of sCOFs, and even orientates the precursors, which is helpful for growth of high-quality sCOFs. [51] Although the detailed mechanism of the reaction still remains controversial, manipulation of on-surface synthesis to various sCOFs has been reported. For example, surface covalent organic frameworks are first reported based on the dehydration of 1,4-benzenediboronic acid or BDBA and 2,3,6,7,10,11-hexahydroxytriphenylene (HHTP) on Ag(111) surface in ultrahigh vacuum. [52]

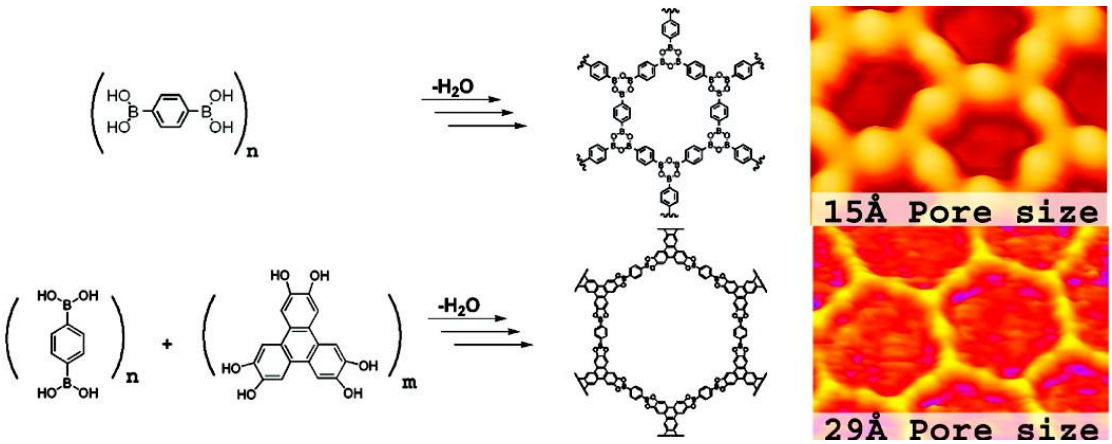

Figure 9. Two surface covalent organic frameworks deposited in extended arrays of near monolayer coverage across a Ag(111) surface. between 370 and 460 K under ultrahigh vacuum. [52]

2.1.3 Characterization methods

Powder X-ray diffraction (PXRD) is the fundamental and most useful technique since single-crystal COFs are difficult to obtain different from MOFs. By PXRD, the crystallinity and structure can be assessed preliminarily. In order to further analyze the precise lattice

parameter, computational simulation based on the reasonable topology of obtained COFs and structure refinement is necessary to be accompanied with experimental PXRD patterns. However, in practice, relative low resolution due to the large wavelength of X-ray, the complicated structure and so many other possible structures make it difficult to confirm the unit cell of COFs by PXRD. Fortunately, Ma *et al.* synthesized a variety of single-crystal 3D COFs and allowed to be large enough for single-crystal X-ray diffraction studies. [53]

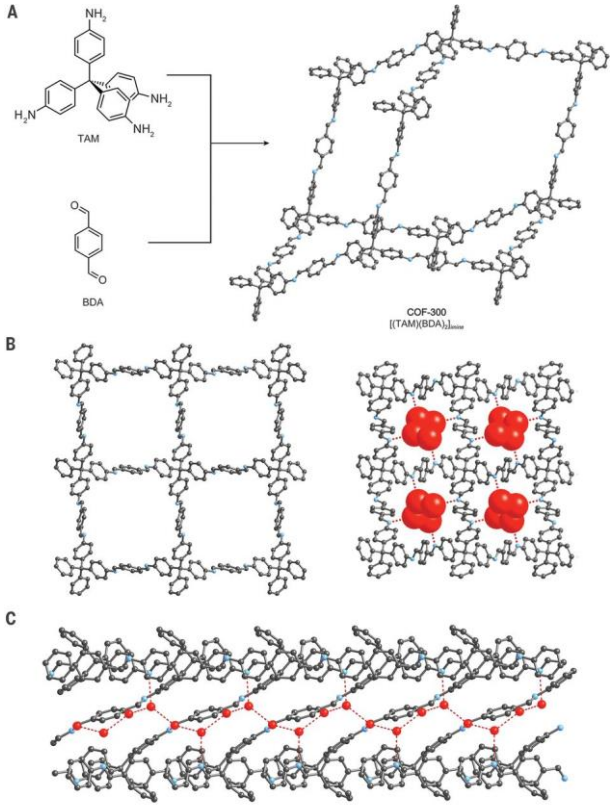

Figure 10. (A) Imine condensation between TAM and BDA produced single-crystalline COF-300. It crystallizes in the space group I41/a with dia topology and sevenfold interpenetrated framework. (B) Upon exposure to water, the crystal structure of COF-300 contracts substantially to form hydrated COF-300. This distortion is due to the formation of highly favorable hydrogen bonds between the imine functional groups and the water guests. (C) The cooperative effect of the hydrogen bonds leads to infinite chains of water guests within the channels of the framework, resulting in a much denser structure. [53]

Solid-state NMR spectroscopy is undoubtedly one of the most powerful technique which has also well been applied in characterizing other solid materials. [54] Many atoms in the COF frameworks, e.g. ^{1}H, ^{13}C, ^{11}B, ^{15}N, ^{29}Si, and ^{17}O, possess the nuclear spin *I*, which renders them NMR active. [55] However, the impurity, defect and overlapped signals decrease the role of solid-state NMR spectroscopy. Therefore, the high crystallinity and

low number of defects of single-crystal COF offer solid-state NMR signals very narrow to confirm the structure precisely at atomic level.

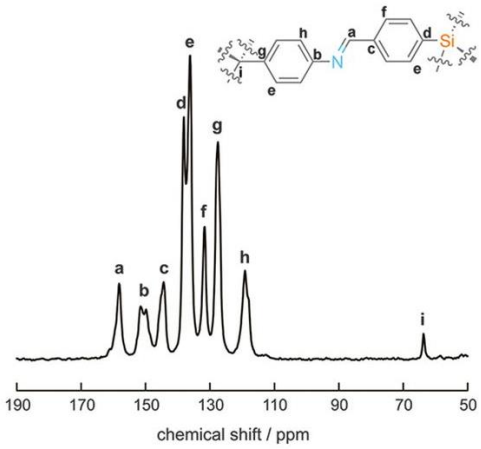

Figure 11. Solid-state ^{13}C CP/MAS NMR spectroscopy verified the anticipated covalent bonding of LZU-111 at the atomic level. [53]

Transmission electron microscope (TEM) is direct and powerful to analyze the microstructure at atomic level owing to the short wavelength of electrons. Indeed, by high-resolution TEM, clear structures of pores and layers can be observed. However, as organic composites, the bad conductivity and covalent bonds of COFs make they too sensitive to high-energy electron beams to remain the crystallinity for a long time. [56] Moreover, in most COFs, lack of elements with large atomic numbers endows a lower resolution. Therefore, some techniques such as 3D electron diffraction tomography can be used to assist with the resolution of COF crystal information. [57]

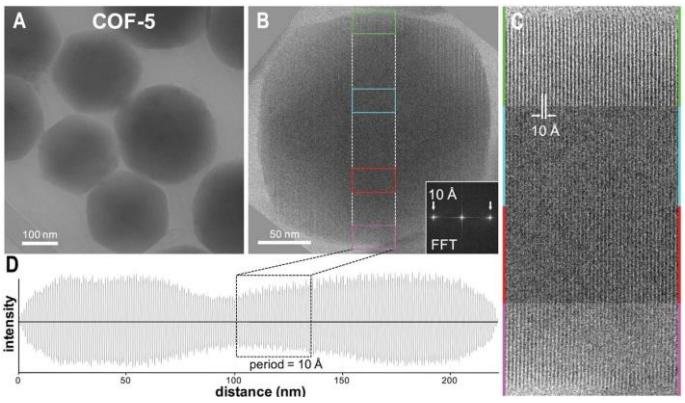

Figure 12. (A) Low-magnification images of COF-5 particles. (B) Lattice-resolution HRTEM image of a COF-5 particle with consistent lattice fringes extending across the entire particle. Inset: FFT of the image, cropped at the predominant fringe spacing (~10 Å, d_{210}). (C) Four regions of interest at higher magnification corresponding to the green, teal, red, and magenta boxed regions of the particle in (B). (D) Intensity profile plot (left to right across the particle) of the image in (B) after applying a bandpass filter. [58]

By contrast with TEM, the analysis of sorption isotherm can indirectly confirm the porosity of COFs. N_2 is the common adsorbate for its inert and relative low cost. Ar is another probe molecule in studies of porosity. Moreover, due to the nonpolarity and higher boiling point (87.29 K) of Ar at standard pressure, it can reduce localized adsorption, particularly on adsorbents with polar sites and shorten equilibrium times, leading to measuring more accurately. [59] Besides N_2 and Ar, CO_2 is an alternative probe for micropores due to the well-known diffusion limitations of N_2 in micropores. [60] Sometimes, the analysis of surface areas and pore size distribution from sorption isotherms is complicated because the unknow pore type and various models.

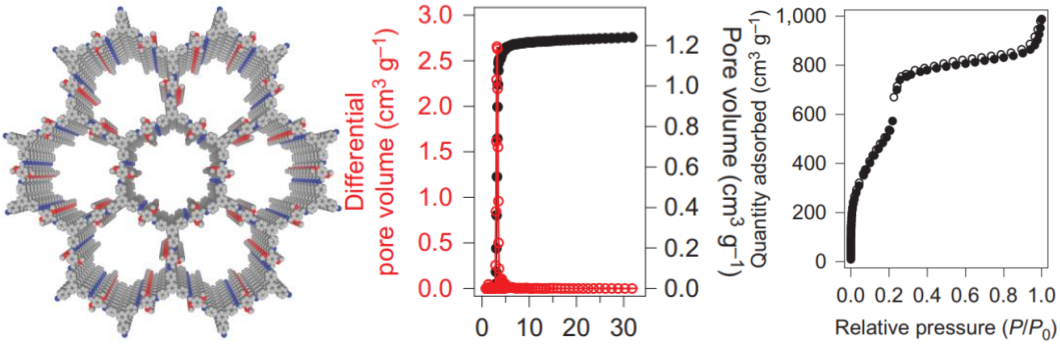

Figure 13. Structure, N_2-sorption isotherm curves measured at 77 K and pore-size distribution of TPB-DMTP-COF. [61]

Scanning tunneling microscope (STM) is another direct technique to investigate the pore structure of COFs. Different from TEM, STM is based on the tunneling current between a conducting tip and examined surface so that it does not require a good conductivity for sample and cause damage to the structure. [62] Moreover, its resolution is considered to be 0.1 nm lateral resolution and 0.01 nm (10 pm) depth resolution. [63] However, it remains a challenging technique because STM requires extremely clean and stable surfaces. In usual, thin COF films or monolayered COFs via on-surface synthesis are able to be analyzed by STM. [64]

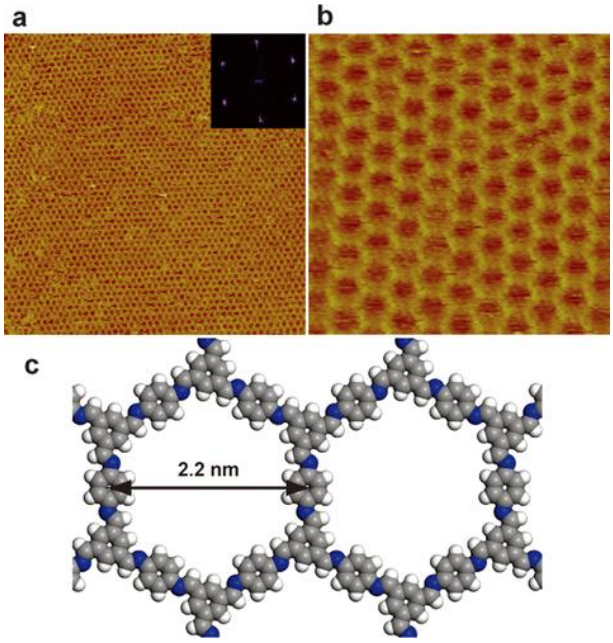

Figure 14. STM images and a structural model for SCOF-IC1. (a) Large-scale STM image (100 × 100 nm^2) of SCOF-IC1 with the inset depicting the corresponding FFT spectrum of the STM image. (b) High resolution STM image (20 × 20 nm^2) of SCOF-IC1. (c) A structural model with the measured structural parameter for SCOF-IC1. [65]

2.1.4 Application

2.1.4.1 Gas adsorption and storage

Due to the ordered structure and comprised light elements, COFs have a large specific surface area so that they exhibit brilliant performance on the storage of various gas such as hydrogen (H_2), carbon dioxide (CO_2), methane (CH_4), and ammonia (NH_3).

The very low density of H_2 in both gas (0.08 kg m^3 at STP) and liquid (70.8 kg m^3 at 20.3 K) form makes its storage a very difficult task. [66] A benchmark material should store 9 wt% of H_2 reversibly between 30 °C to 80 °C (the 2015 target by the U.S. Department of Energy (DOE)). [67] Also, durability of the storage material should be at least 1000 cycles and the refuel time should not exceed 3 min. Furukawa *et al.* studied the H_2-storage properties of various 2D COFs and 3D COFs with boroxine and boronic ester linkages at 77 K. [68] The saturation uptake of 3D COF-102 is 72.4 mg g^{-1} (7.24 wt%) at 77 K. comparable with that of MOF-177 (75 mg g^{-1}) and MOF-5 (76 mg g^{-1}). Besides physisorption, chemisorption can increase the H_2 storage capacity of a porous material investigated thoroughly in theoretical studies. In doped COFs with transition metals, Li, Na,

K, and Ca, H_2 molecule dissociates at the metal site followed by migration of hydrogen atoms to the framework of COFs. [69] For example, When Li^+ is introduced as the counterion in the COF, high gas storage capacities can be observed for H_2 (3.11 wt% H_2 at 77 K and 1 bar).

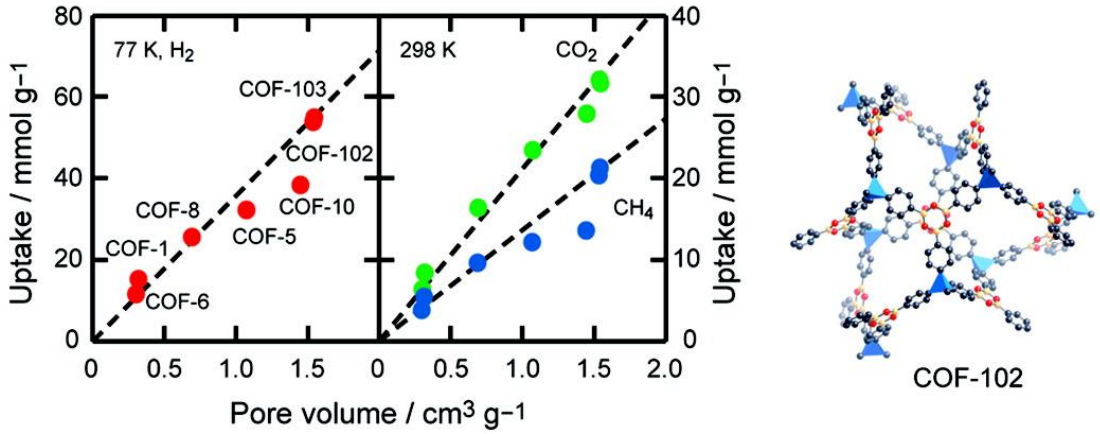

Figure 15. Relationship between absolute gas uptake and pore volume of COFs estimated from Ar isotherms. The regression lines based on the uptakes for COF-1, -6, -8, -102, and -103 are overlaid. Red, blue, and green circles represent the uptakes of H_2 (77 K, 70 bar), CH_4 (298 K, 70 bar), and CO_2 (298 K, 50 bar), respectively. [68]

CO_2 released from the combustion of fossil fuel is one of main gases causing global warming. [70] Together with other porous materials such as MOFs, COFs have also been proposed as an excellent candidate for CO_2 capture. Different from MOFs, whose performance is deteriorated in humid CO_2 due to strong bonding between metal sites and H_2O, COFs exhibit great CO_2 selectivity and repeated usage. [71] For example, perfluorinated covalent triazine-based framework (FCTF-1) shows a CO_2 capture uptake of 1.76 mmol g^{-1} at 273 K and 0.1 bar and an exceptional tolerant to water when there was moisture in the gas mixture, due to the hydrophobic nature of the introduced C–F bonds. [72]

Pore volume, pore size, and surface area are important parameters that determine the gas storage capability. At high pressure, due to multi-layer sorption, the CO_2 uptake is much relative with pore volume. For example, at 50 bar, COF-103 with a larger pore volume have a larger CO_2 uptake. At low pressure, pore size and surface area are more important to single layer interaction between CO_2 and the pore wall. Although the relationship between pore size/surface area and CO_2 uptake is still unclear, a lot of results suggest micropore and larger surface area is a prerequisite to increase gas uptake densities.

Besides, the type of linkage and building blocks is another factor of affecting the interaction between CO_2 and COFs. For example, HEX-COF-1 [73] and COF-JLU2 [74] with the azine linkage are excellent with high capacities of 20 and 21.7 wt% at 273 K and 1 bar owing to the interactions of CO_2 with the linkages through the nitrogen lone pairs. Introducing heteroatoms and functional groups such as F, alkyl chains, alcohol, ester, carboxylic acid, and amine units is useful to tune the surface of pore walls, resulting in the special interaction with CO_2. For example, although the BET surface area, pore volume and pore size decrease, the CO_2 uptake capacity $[HO_2C]_x$%-H_2P-COFs increases at 298 k and 1 bar with the increasing density of carboxylic acid groups. [75] Introducing fluorine groups to the skeleton also can enhance electrostatic interaction with CO_2 and improves the uptake. [72]

CH_4, as an abundant and inexpensive gas, stands out as a potential vehicular fuel to replace conventional fossil fuel. [76] COFs exhibit good performance for CH_4 capture. For instance, 2D COF-5 showed a CH_4 uptake capacity of 89 mg g^{-1} at high pressure (35 bar) and 298 K. At low pressure (1 bar), high CH_4 uptake was measured at 273 K for ACOF-1 with 1.15 wt% and Hex-COF-1 with 2.3 wt%. [73]

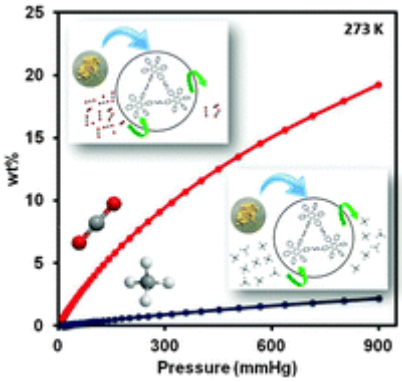

Figure 16. HEX-COF 1 has an average pore size of 1 nm, a surface area in excess of 1200 m^2 g^{-1} and shows excellent sorption capability for carbon dioxide (20 wt%) and methane (2.3 wt%) at 273 K and 1 atm. [73]

2.1.4.2 Electrochemical energy storage and conversion

COFs have been demonstrated a great potential on electrochemical energy storage and conversion such as protoncondution, CO_2 reduction reaction, hydrogen evolution reaction (HER) and Li-sulfur batteries. [77-80] For example, cationic COF EB-COF:Br achieves a

proton conductivity of 3.32×10^{-3} S cm^{-1} (98% RH, 298 K) by exchanging the counterion Br^- immobilized in the pores with $PW_{12}O_{40}^{3-}$. [81] Metalated COF-366-Co were investigated as electrocatalytic CO_2 reduction catalysts, producing 36 mL mg^{-1} of CO over the course of 24 h with an overpotential of –0.55 V and a Faradaic efficiency of 90%. [82] SB-PORPy-COF has shown the onset potential of 50 mV and the Tafel slope of 116 mV dec^{-1} but a large overpotential. [83] COF-1 was tested as polysulfide host for Li-S batteries, exhibiting a remarkable capacity and cycling stability with 929 mA h g^{-1} at 0.5 C after 100 cycles. [84]

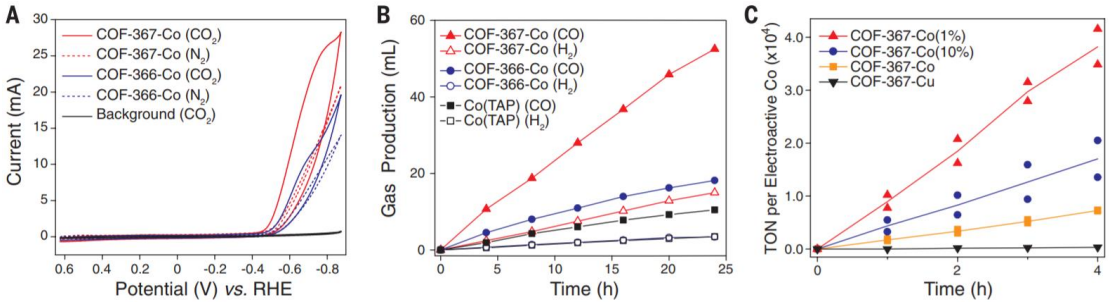

Figure 17. (A) Cyclic voltammograms of COF-366-Co and COF-367-Co in carbon dioxide–saturated medium (pH 7.2 aqueous potassium phosphate buffer (0.2 M) with additives: 0.5 M $KHCO_3$) or nitrogen-saturated medium (0.5 M $NaClO_4$). (B) Long-term bulk electrolyses at –0.67 V (versus RHE). (C) Bulk electrolyses of bimetallic COFs at –0.67 V (versus RHE). [82]

2.2 Covalent organic framework derived porous composites

The high porosity and good stability of COFs are beneficial to ion transfer, immobilization of active material and so on. However, the intrinsically poor conductivity limits the wide application in the other fields, such as oxygen reduction reaction (ORR), oxygen evolution reaction (OER), supercapacitors and Li-ion battery, which require catalysts to provide a good electron transfer during the electrochemical reaction. Many efforts have been made to improve the conductivity of COFs. For example, self-assembling pristine covalent organic polymer (COP) with reduced graphene oxide (rGO) leads to the increased electrical conductivity of the hybridized COP/rGO materials by more than seven orders of magnitude (from 3.06×10^{-9} to 2.56×10^{-1} S m^{-1}) compared with pure COPs, however, the ORR performance is still much lower than commercial Pt/C. [85] Redox-active COF (DTP-ANDI-COF) was coated on carbon nanotube (CNT) wires as a new platform for lithium-ion battery. The battery achieves a capacity of 74 mAh g^{-1} at 2.4 C because DTP-ANDI-COF

walls undergo multi-electron oxidation and reduction processes, the open mesopores facilitate the transport of ions into and out of the electrodes, and the CNTs promote electron conduction. [86] However, the performance is much lower than those of other inorganic material-based batteries.

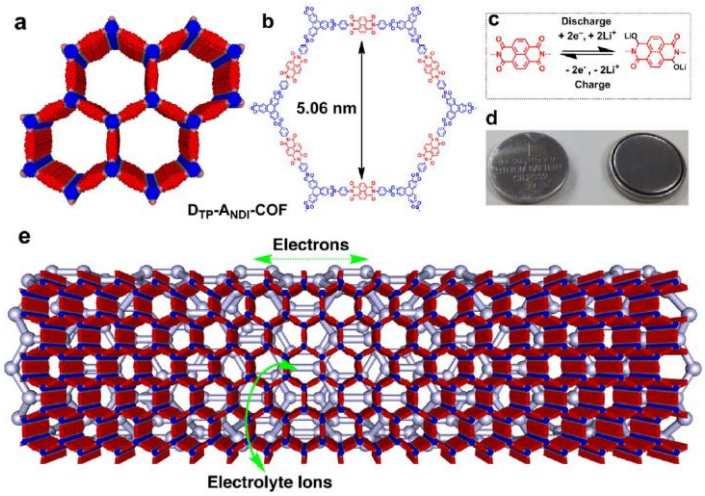

Figure 18. Structure of redox-active organic electrode materials. (a) Schematic of the AA-stacking of DTP-ANDI-COF with redox-active naphthalene diimide walls (red) and one-dimensional meso-scale channels. (b) Chemical structure of one pore in DTP-ANDI-COF. (c) Electrochemical redox reaction of a naphthalene diimide unit. (d) Photographs of a coin-type battery. (e) Graphical representation of DTP-ANDI-COF@CNTs (grey for CNTs) and electron conduction and ion transport. [86]

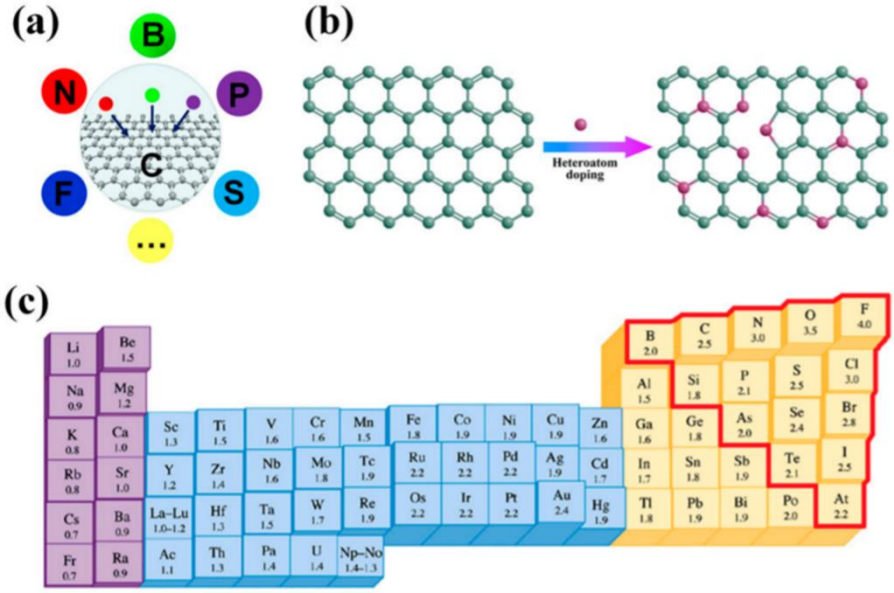

Figure 19. (a) Doping of graphitic carbon structure with heteroatoms (e.g., N, B, P). (b) Doping of graphitic carbon structure with heteroatoms (e.g., N) by post-treatment. (c) Periodic table and the corresponding electronegativity of elements. [88]

An alternative way to improve the electrochemical performance of COFs is transforming them into conductive carbons. Pure carbon materials such as graphene and

graphite are inert towards electrochemical reactions as electrocatalysts owing to the lack of active sites. [87] Doping with heteroatoms into carbon realizes electron redistribution, polariton and active defect sites because the size, electronegativity and orbital hybridization of heteroatoms are different from those of carbon. [88-90] Doped carbon often exhibits an enhanced electrochemical performance, which can be tuned by adjusting the doping mode, total dopant content and doping procedure. The nitrogen atom is the most common dopant for carbon materials including graphene because its size is similar with the carbon atom and its electronegativity is larger. [91] This means the electronic/ionic conductivity of nitrogen doped carbon will be enhanced due to the higher electronegativity of nitrogen (3.04), leading to more electrons attracted toward the doped section. [92] The boron atom can be in-plane doped into carbon by sp^2 hybridization, which retains the planar structure of graphene without distortion. [93] The relatively greater electropositivity between boron and carbon atoms enables charge polarization due to one less valence electron to the neighboring carbon, stabilizing the negatively polarized atoms. [94] The sulfur atom has a very similar negativity (2.58) with that of the carbon atom (2.55), but its larger atomic size and polarizability make it higher spin density, edge strain, and charge delocalization. [95] By contrast with nitrogen, the electronegativity of phosphorus (2.19) is lower than that of carbon; thus, the polarity of the C−P bonding is opposite to that of the C−N bonding. However, in phosphorus doped section, sp^3 hybridization is favorable because of the strong hybridization between P 3p and C 2p orbitals, giving rise to structural distortion, decreased conductivity but defects owing to the broken plane of graphene. [96] Moreover, in general, co-doped carbons and triple-doped carbons have been found to exhibit increased ORR performances compared to their single-doped counterparts. For example, the HER performance of N,S and N,P co-doped graphene (N,S-G and N,P-G) is much better than N doped graphene (N-G) determined by experimental and theoretical results. [97]

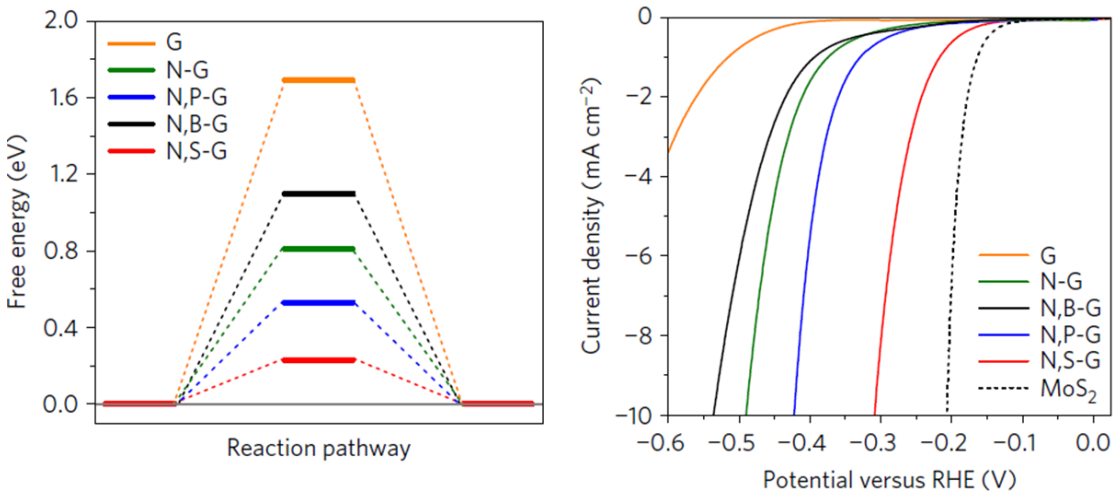

Figure 20. (Left) The three-state free energy diagram for the pure, single- and dual-doped graphene models; (Right) HER performance of various graphene-based materials. [97]

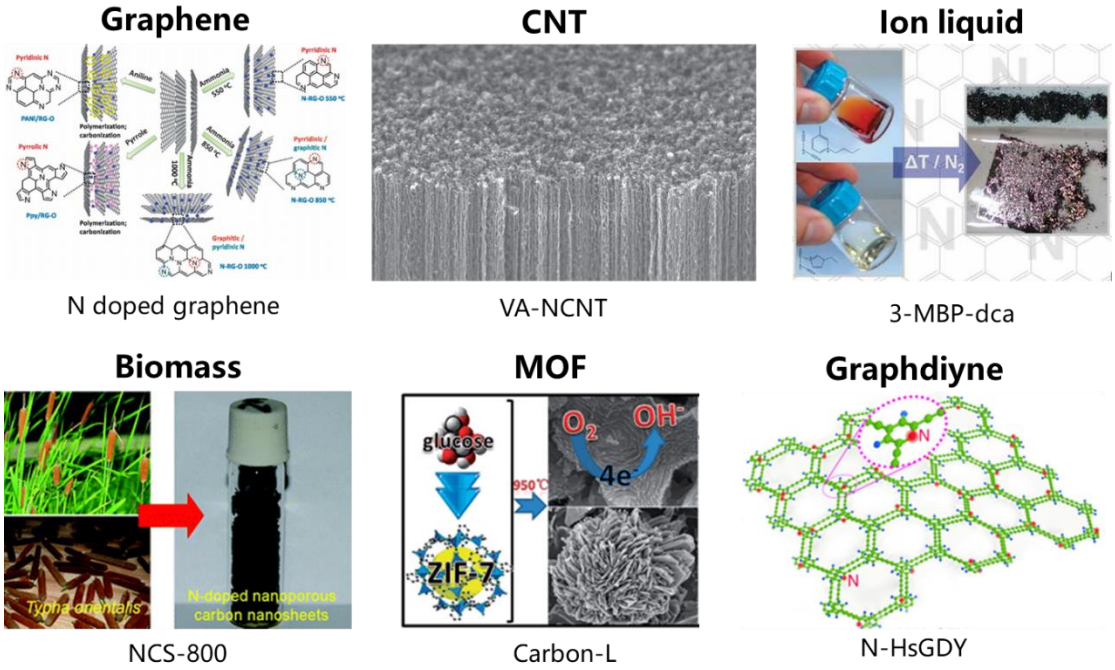

Figure 21. Various doped carbon (N doped graphene, [98] VA-NCNT, [99] 3-MBP-dca, [100] NCS-800, [101] Carbon-L, [102] and N-HsGDY [103]) from graphene, CNT, ion liquid, biomass, MOF and graphdiyne.

Recently, various precursors such as graphene, biomass, sustainable carbonaceous products, metal-organic frameworks (MOFs) and amorphous polymers have been used to fabricate doped-carbon nanomaterials by chemical vapor deposition (CVD), annealing and plasma treatment. By contrast of metal-based catalysts, especially the noble metals (Pt, Ir and Pd) or metal oxides, these metal-free catalysts have been paid much attention due to the low cost, good durability, and good immunity towards poisoning and harsh environment.

[104] Compared with these precursors, COFs are highly crystalline and thermally stable so that they can be converted into conductive graphitic carbon domains more easily from the conjugated structure. In addition, diverse active heteroatoms such as B, N and functional groups can be easily designed and incorporated into the skeleton or poral surface of COFs. [105] Thanks to the adjustable pore size and high surface area, these heteroatoms from the abundant building blocks can diffuse within the framework in a fast and uniform manner during the pyrolysis, resulting in highly porous architectures with homogeneously distributed active sites. Furthermore, different from MOFs, whose metals are prone to too strongly binding with C, N, O etc. to be removed easily after carbonization so that the ORR activity decreases gradually due to the oxidation, instability on the morphology and crystallinity and inevitable agglomeration/dissolution of the trace metals, [106] COFs as a kind of sophisticated precursors are preferable to fabricate robust metal-free doped carbon owing to non-aftertreatment of etching metals. For example, polycyclotriphosphazene-co-4,4'sulfonyldiphenol (PPZS) spheres was encapsulated by TAPT-DHTA-COF and pyrolyzed into N, P, S doped carbon, which exhibited a high capacitance of 255 F g^{-1} at 0.5 A g^{-1}. [107]

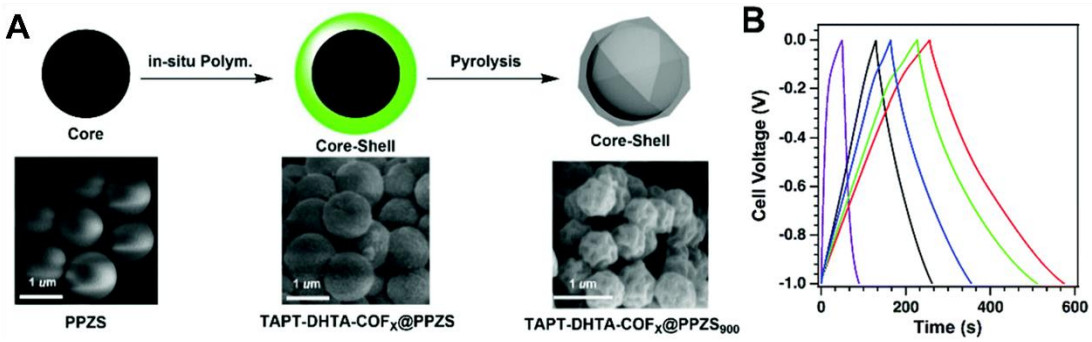

Figure 22. (A) Schematic of the synthesis of TAPT–DHTA–COFX@PPZS and its pyrolysis to process TAPT–DHTA–COFX@PPZS900. (B) Galvanostatic charge/discharge curves at 1 A g^{-1}. $PPZS_{900}$ (black), TAPT–DHTA–COF_{900} (purple), TAPT–DHTA$COF_{0.05}$@$PPZS_{900}$ (blue), TAPT–DHTA–$COF_{0.1}$@$PPZS_{900}$ (red), and TAPT–DHTA–$COF_{0.2}$@$PPZS_{900}$ (green). [107]

3. Significance of the research

With the increasing population and demand of energy, the environmental issues caused by the utilization of fossil fuels have been paid more and more attention. Moreover, the

development and commercial application of new clean energy is still at the primary stage. The demand of high-performance materials with specific properties becomes more and more urgent. Among these, advanced porous materials such as COFs and their derived composites are playing important role. For example, they can be used as absorbent to capture exhaust gases such as CO_2 and SO_2 and effectively storage fuel gases CH_4 and H_2 due to their high surface areas and controllable pores. As electrocatalysts, owing to the low cost, high stability, nontoxicity and excellent electrical conductivity, porous materials particularly carbon-based nanomaterials are also utilized to store and convert chemical and solar energy in the form of electric energy.

4. Research questions and hypotheses

The question is how to design the structure of these porous materials and how to optimize the initial structure and overcome the intrinsic drawback to meet the certain requirement.

As a part of our research, the diversity of COFs in geometry is very intriguing based on 2D and 3D reticular chemistry. But how about 1D COFs? Is it possible to build an 1D COF, which possesses the commonly unique properties of COFs such as high crystallinity and ordered pores but the covalent bonds expand only in one direction? Considered that various other 1D molecularly crystalline structure including 1D polymer, 1D polyhedron, 1D nanoribbon especially 1D MOFs have been reported, fabricating 1D COFs by geometric matching between building blocks is reasonable.

As for 2D COFs, what will happen if two building blocks both are larger conjugated molecules rather than one of them is a small linear molecule? Although keeping the balance between the thermodynamics and the kinetics of the reaction in such cases is difficult, but if achieved, could decrease the number of building blocks consisting of each pore, leading to supermicropores, which are crucial to achieve a high gas uptake density for gas like CO_2. Another point is the relationship between the structure and gas uptake performance of COFs. For example, what's the effect of inert functional groups like methyl groups on the CO_2 capture capacity? Positive or negative? It is controversial. However, in consideration of the electron-donating property of methyl groups, they might enhance the

interaction between the framework and CO_2.

Various doped carbon nanomaterials have been synthesized from graphene derivates, CNT and biomass as electrocatalysts. However, doped or co-doped carbon derived from COFs have rarely been discussed and not truly reported to date. Given stable conjugated structure and rich active heteroatoms such as B, N, O and S within frameworks, COFs should be good platforms to construct heteroatom doped carbons.

References

1. Rouquerol, J.; Avnir, D.; Fairbridge, C. W.; Everett, D. H.; Haynes, J. H.; Pernicone, N.; Ramsay, J. D. F.; Sing, K. S. W.; Unger, K. K. *Pure Appl. Chem.* **1994**, *66*, 1739.
2. Yamauchi, Y.; Kuroda, K. *Chem. Asian J.* **2008**, *3*, 664.
3. Ren, Y.; Ma, Z.; Bruce, P. G. *Chem. Soc. Rev.* **2012**, *41*, 4909.
4. Geraud, E.; Rafqah, S.; Sarakha, M.; Forano, C.; Prevot, V.; Leroux, F. *Chem. Mater.* **2008**, *20*, 1116.
5. Ma, Y.; Tong, W.; Zhou, H.; Suib, S. L. *Microporous Mesoporous Mater.* **2000**, *37*, 243.
6. Lee, J.; Kim, J.; Hyeon, T. *Adv. Mater.* **2006**, *18*, 2073.
7. Cooper, A. I. *Adv. Mater.* **2009**, *21*, 1291.
8. McKeown, N. B.; Budd, P. M. *Chem. Soc. Rev.* **2006**, *35*, 675.
9. Hasell, T.; Cooper, A. I. *Nat. Rev. Mater.* **2016**, *1*, 16053.
10. Zhang, S.; Dokko, K.; Watanabe, M. *Chem. Sci.* **2015**, *6*, 3684.
11. Ding, S. Y.; Wang, W. *Chem. Soc. Rev.* **2013**, *42*, 548.
12. Zhou, H. C.; Long, J. R.; Yaghi, O. M. *Chem. Rev.* **2012**, *112*, 673.
13. James, S. L. *Chem. Soc. Rev.* **2003**, *32*, 276.
14. Bertrand, G. H.; Michaelis, V. K.; Ong, T. C.; Griffin, R. G.; Dincă, M. *Proc. Natl. Acad. Sci.* **2013**, *110*, 4923.
15. Diercks, C. S.; Liu, Y.; Cordova, K. E.; Yaghi, O. M. *Nat. Mater.* **2018**, *17*, 301.
16. Peng, Y.; Li, Y.; Ban, Y.; Jin, H.; Jiao, W.; Liu, X.; Yang, W. *Science*, **2014**, *346*, 1356.
17. Schnepp, Z. *Angew. Chem. Int. Ed.* **2013**, *52*, 1096.
18. Caminade, A. M.; Yan, D.; Smith, D. K. *Chem. Soc. Rev.* **2015**, *44*, 3870.

19. Helms, B.; Mynar, J. L.; Hawker, C. J.; Frechet, J. M. *J. Am. Chem. Soc.* **2004**, *126*, 15020.
20. Flory, P. J.; Rehner Jr, J. *J. Chem. Phys.* **1943**, *11*, 512.
21. Huang, N.; Wang, P.; Jiang, D. *Nat. Rev. Mater.* **2016**, *1*, 16068.
22. Furukawa, H.; Cordova, K. E.; O'Keeffe, M.; Yaghi, O. M. *Science* **2013**, *341*, 1230444.
23. Murray, L. J.; Dincă, M.; Long, J. R. *Chem. Soc. Rev.* **2009**, *38*, 1294.
24. Li, J. R.; Sculley, J.; Zhou, H. C. *Chem. Rev.* **2011**, *112*, 869.
25. Rogge, S. M.; Bavykina, A.; Hajek, J.; Garcia, H.; Olivos-Suarez, A. I.; Sepúlveda-Escribano, A.; Vimont, A.; Clet, G.; Bazin, P.; Kapteijn, F.; Daturi, M.; Ramos-Fernandez, E. V.; Llabrés i Xamena, F. X., Van Speybroeck, V.; Gascon J. *Chem. Soc. Rev.* **2017**, *46*, 3134.
26. Horike, S.; Umeyama, D.; Kitagawa, S. *Acc. Chem. Res.* **2013**, *46*, 2376.
27. Lohse, M. S.; Bein, T. *Adv. Funct. Mater.* **2018**, *28*, 1705553.
28. Waller, P. J.; Gándara, F.; Yaghi, O. M. *Acc. Chem. Res.* **2015**, *48*, 3053.
29. Ding, X.; Guo, J.; Feng, X.; Honsho, Y.; Guo, J.; Seki, S.; Maitarad, P.; Saeki, A.; Nagase, S.; Jiang, D. *Angew. Chem. Int. Ed.* **2010**, *50*, 1289.
30. Dalapati, S.; Jin, S.; Gao, J.; Xu, Y.; Nagai, A.; Jiang, D. *J. Am. Chem. Soc.* **2013**, *135*, 17310.
31. Lyle, S. J.; Waller, P. J.; Yaghi, O. M. *Tre. Chem.* **2019**, *1*, 172.
32. Wei, P. F.; Qi, M. Z.; Wang, Z. P.; Ding, S. Y.; Yu, W.; Liu, Q.; Wang, L.-K.; Wang, H.-Z.; An. W.-K.; Wang, W. *J. Am. Chem. Soc.* **2018**, *140*, 4623.
33. Wu, X.; Han, X.; Liu, Y.; Liu, Y.; Cui, Y. *J. Am. Chem. Soc.* **2018**, *140*, 16124.
34. Kuhn, P.; Antonietti, M.; Thomas, A. *Angew. Chem. Int. Ed.* **2008**, *47*, 3450.
35. Zhang, B.; Wei, M.; Mao, H.; Pei, X.; Alshmimri, S. A.; Reimer, J. A.; Yaghi, O. M. *J. Am. Chem. Soc.* **2018**, *140*, 12715.
36. Jin, Y.; Hu, Y.; Zhang, W. *Nat. Rev. Chem.* **2017**, *1*, 0056.
37. Li, H.; Chavez, A. D.; Li, H.; Li, H.; Dichtel, W. R.; Bredas, J. L. *J. Am. Chem. Soc.* **2017**, *139*, 16310.
38. Lafferentz, L. Eberhardt, V.; Dri, C.; Africh, C.; Comelli, G.; Esch, F.; Hecht, S.; Grill, L. *Nat. Chem.* **2012**, *4*, 215.
39. Liu, X.-H.; Guan, C.-Z.; Wang, D.; Wan, L.-J. *Adv. Mater.* **2014**, *26*, 6912.

40. Liu, Y.; Ma, Y.; Zhao, Y.; Sun, X.; Gándara, F.; Furukawa, H.; Liu, Z.; Zhu, H.; Zhu, C.; Suenaga, K.; Oleynikov, P.; Alshammari, A. S.; X. Zhang, Terasaki, O.; Yaghi, O. M. *Science* **2016**, *351*, 365.
41. Zhao, Y.; Guo, L.; Gándara, F.; Ma, Y.; Liu, Z.; Zhu, C.; Lyu, H.; Trickett, C. A.; Kapustin, E. A.; Terasaki, O.; Yaghi, O. M. *J. Am. Chem. Soc.* **2017**, *139*, 13166.
42. Meric, I.; Han, M. Y.; Young, A. F.; Ozyilmaz, B.; Kim, P.; Shepard, K. L. *Nat. Nanotechnol.* **2008**, *3*, 654.
43. Xu, X.; Liu, C.; Sun, Z.; Cao, T.; Zhang, Z.; Wang, E.; Liu, Z.; Liu, K. *Chem. Soc. Rev.* **2018**, *47*, 3059.
44. Rizzo, D. J., Veber, G., Cao, T., Bronner, C., Chen, T., Zhao, F., Rodriguez, H.; Louie, S. G.; Crommie, M. F.; Fischer, F. R. *Nature* **2018**, *560*, 204.
45. Cote, A. P.; Benin, A. I.; Ockwig, N. W.; O'keeffe, M.; Matzger, A. J.; Yaghi, O. M. *Science* **2005**, *310*, 1166.
46. Fang, Q.; Zhuang, Z.; Gu, S.; Kaspar, R. B.; Zheng, J.; Wang, J.; Qiu, S.; Yan, Y. *Nat. Commun.* **2014**, *5*, 4503.
47. de la Hoz, A.; Diaz-Ortiz, A.; Moreno, A. *Chem. Soc. Rev.* **2005**, *34*, 164.
48. Campbell, N. L.; Clowes, R.; Ritchie, L. K.; Cooper, A. I. *Chem. Mater.* **2009**, *21*, 204.
49. Biswal, B. P.; Chandra, S.; Kandambeth, S.; Lukose, B.; Heine, T.; Banerjee, R. *J. Am. Chem. Soc.* **2013**, *135*, 5328.
50. Blunt, M. O.; Russell, J. C.; Champness, N. R.; Beton, P. H. *Chem. Commun.* **2010**, *46*, 7157.
51. Grill, L.; Dyer, M., Lafferentz, L.; Persson, M.; Peters, M. V.; Hecht, S. *Nat. Nanotechnol.* **2007**, *2*, 687.
52. Zwaneveld, N. A.; Pawlak, R.; Abel, M.; Catalin, D.; Gigmes, D.; Bertin, D.; Porte, L. *J. Am. Chem. Soc.* **2008**, *130*, 6678.
53. Ma, T.; Kapustin, E. A.; Yin, S. X.; Liang, L.; Zhou, Z.; Niu, J.; Li, L.-H.; Wang, Y.; Su, J.; Li, J.; Wang, X.; Wang, W. D.; Wang, W.; Sun, J.; Yaghi, O. M. *Science* **2018**, *361*, 48.
54. Duer, M. J. *Solid state NMR spectroscopy: principles and applications*. John Wiley & Sons. **2008**.
55. Hunger, M.; Wang, W. *Adv. Catal.* **2006**, *50*, 149.

56. Smith, B. J.; Parent, L. R.; Overholts, A. C.; Beaucage, P. A.; Bisbey, R. P.; Chavez, A. D.; Hwang, N.; Park, Ch.; Evans, A. M.; Gianneschi, N. C.; Dichtel, W. R. *ACS Cent. Sci.* **2017**, *3*, 58.
57. Zhang, Y. B.; Su, J.; Furukawa, H.; Yun, Y.; Gándara, F.; Duong, A.; Zou, X.; Yaghi, O. M. *J. Am. Chem. Soc.* **2013**, *135*, 16336.
58. Evans, A. M.; Parent, L. R.; Flanders, N. C.; Bisbey, R. P.; Vitaku, E.; Kirschner, M. S.; Schaller, R. D.; Chen, L. X.; Gianneschi, N. C.; Dichtel, W. R. *Science* **2018**, *361*, 52.
59. Ehrburger-Dolle, F.; Holz, M.; Lahaye, J. *Pure Appl. Chem.* **1993**, *65*, 2223.
60. Jagiello, J.; Thommes, M. *Carbon* **2004**, *42*, 1227.
61. Xu, H.; Gao, J.; Jiang, D. *Nat. Chem.* **2015**, *7*, 905.
62. Tersoff, J.; Hamann, D. R. *Phys. Rev. Lett.* **1983**, *50*, 1998.
63. Gross, L.; Mohn, F.; Moll, N.; Liljeroth, P.; Meyer, G. *Science* **2009**, *325*, 1110.
64. Joshi, T.; Chen, C.; Li, H.; Diercks, C. S.; Wang, G.; Waller, P. J.; Li, H.; Bredas, J.-L.; Yaghi, O. M.; Crommie, M. F. *Adv. Mater.* **2019**, *31*, 1805941.
65. Liu, X. H.; Guan, C. Z.; Ding, S. Y.; Wang, W.; Yan, H. J.; Wang, D.; Wan, L. J. *J. Am. Chem. Soc.* **2013**, *135*, 10470.
66. https://iupac.org/materialschemistryedu/energy/hydrogen-storage/
67. DoE Office of Energy Efficiency and Renewable Energy Hydrogen, Fuel Cells & Infrastructure Technologies Program, 'Grand Challenge' for Basic and Applied Research in Hydrogen Storage Solicitation, available at: http://www.eere.energy.gov/ hydrogenandfuelcells/2003_storage_solicitation.html.
68. Furukawa, H.; Yaghi, O. M. *J. Am. Chem. Soc.* **2009**, *131*, 8875.
69. Y. J. Choi; J. W. Lee; J. H. Choi; J. K. Kang, *Appl. Phys. Lett.* **2008**, *92*, 173102.
70. Jenkinson, D. S.; Adams, D. E.; Wild, A. *Nature* **1991**, *351*, 304.
71. Zeng, Y.; Zou, R.; Zhao, Y. *Adv. Mater.* **2016**, *28*, 2855.
72. Zhao, Y.; Yao, K. X.; Teng, B.; Zhang, T.; Han, Y. *Energy Environ. Sci.* **2013**, *6*, 3684.
73. Alahakoon, S. B.; Thompson, C. M.; Nguyen, A. X.; Occhialini, G.; McCandless, G. T.; Smaldone, R. A. *Chem. Commun.* **2016**, *52*, 2843.
74. Li, Z.; Zhi, Y.; Feng, X.; Ding, X.; Zou, Y.; Liu, X.; Mu, Y. *Chem. Eur. J.* **2015**, *21*, 12079.

75. Huang, N.; Chen, X.; Krishna, R.; Jiang, D. *Angew. Chem. Int. Ed.* **2015**, *54*, 2986.

76. Alvarez, R. A.; Zavala-Araiza, D.; Lyon, D. R.; Allen, D. T.; Barkley, Z. R.; Brandt, A. R.; K. Davis, J.; Herndon, S. C.; Jacob, D. J.; Karion, A.; Kort, E. A.; Lamb, B. K.; Lauvaux, T.; Maasakkers, J. D.; Marchese, A. J.; Omara, M.; Pacala, S. W.; Peischl, J.; Robinson, A. L.; Shepson, P. B.; Sweeney, C.; Townsend-Small, A.; Wofsy, S. C.; Hamburg, S. P. *Science* **2018**, *361*, 186.

77. Chandra, S.; Kundu, T.; Kandambeth, S.; BabaRao, R.; Marathe, Y.; Kunjir, S. M.; Banerjee, R. *J. Am. Chem. Soc.* **2014**, *136*, 6570.

78. Diercks, C. S.; Lin, S.; Kornienko, N.; Kapustin, E. A.; Nichols, E. M.; Zhu, C.; Zhao, Y.; Chang, C. J.; Yaghi, O. M. *J. Am. Chem. Soc.* **2018**, *140*, 1116.

79. Lin, C. Y.; Zhang, D.; Zhao, Z.; Xia, Z. *Adv. Mater.* **2018**, *30*, 1703646.

80. Liao, H.; Ding, H.; Li, B.; Ai, X.; Wang, C. *J. Mater. Chem. A* **2014**, *2*, 8854.

81. Ma, H.; Liu, B.; Li, B.; Zhang, L.; Li, Y. G.; Tan, H. Q.; Zang, H.-Y.; Zhu, G. *J. Am. Chem. Soc.* **2016**, *138*, 5897.

82. Lin, S.; Diercks, C. S.; Zhang, Y. B.; Kornienko, N.; Nichols, E. M.; Zhao, Y.; Paris, A. R.; Kim, D.; Yang, P.; Yaghi. O. M.; Chang, C. J. *Science* **2015**, *349*, 1208.

83. Bhunia, S.; Das, S. K.; Jana, R.; Peter, S. C.; Bhattacharya, S.; Addicoat, M.; Bhaumik, A.; Pradhan, A. *ACS Appl. Mater. Interfaces* **2017**, *9*, 23843.

84. Ghazi, Z. A.; Zhu, L.; Wang, H.; Naeem, A.; Khattak, A. M.; Liang, B.; Khan, N. A.; Wei, Z.; Li, L.; Tang, Z. *Adv. Energy Mater.* **2016**, *6*, 1601250.

85. Guo, J.; Lin, C. Y.; Xia, Z.; Xiang, Z. *Angew. Chem.* **2018**, *130*, 12747.

86. Xu, F.; Jin, S.; Zhong, H.; Wu, D.; Yang, X.; Chen, X.; Wei, H.; Fu, R.; Jiang, D. *Sci. Rep.* **2015**, *5*, 8225.

87. Zheng, Y.; Jiao, Y.; Li, L. H.; Xing, T.; Chen, Y.; Jaroniec, M.; Qiao, S. Z. *ACS Nano* **2014**, *8*, 5290.

88. Hu, C.; Dai, L. *Angew. Chem. Int. Ed.* **2016**, *55*, 11736.

89. Jin, H.; Guo, C.; Liu, X.; Liu, J.; Vasileff, A.; Jiao, Y.; Zheng, Y.; Qiao, S. Z. *Chem. Rev.* **2018**, *118*, 6337.

90. Jiao, Y.; Zheng, Y.; Jaroniec, M.; Qiao, S. Z. *Chem. Soc. Rev.* **2015**, *44*, 2060.

91. Asefa, T. *Acc. Chem. Res.* **2016**, *49*, 1873.

92. Wu, P.; Du, P.; Zhang, H.; Cai, C. *Phys. Chem. Chem. Phys.* **2013**, *15*, 6920.
93. Rani, P.; Jindal, V. K. *RSC Adv.* **2013**, *3*, 802.
94. Kong, X.; Chen, Q.; Sun, Z. *ChemPhysChem* 2013, *14*, 514.
95. Liang, J.; Jiao, Y.; Jaroniec, M.; Qiao, S. Z. *Angew. Chem. Int. Ed.* **2012**, *51*, 11496.
96. Wang, X.; Sun, G.; Routh, P.; Kim, D.-H.; Huang, W.; Chen, P. *Chem. Soc. Rev.* **2014**, *43*, 7067.
97. Jiao, Y.; Zheng, Y.; Davey, K.; Qiao, S. Z. *Nat. Energy* **2016**, *1*, 16130.
98. Lai, L., Potts, J. R., Zhan, D., Wang, L., Poh, C. K., Tang, C., Gong, H.; Shen, Z.; Lin. J.; Ruoff, R. S. *Energy Environ. Sci.* **2012**, *5*, 7936.
99. Gong, K.; Du, F.; Xia, Z.; Durstock, M.; Dai, L. *Science* 2009, *323*, 760.
100. Paraknowitsch, J. P.; Zhang, J.; Su, D.; Thomas, A.; Antonietti, M. *Adv. Mater.* **2010**, *22*, 87.
101. Chen, P., Wang, L.-K., Wang, G., Gao, M.-R., Ge, J., Yuan, W.-J., Shen, Y.-H.; Xie, A.-J; Yu, S.-H. *Energy Environ. Sci.* **2014**, *7*, 4095.
102. Zhang, P.; Sun, F.; Xiang, Z.; Shen, Z.; Yun, J.; Cao, D. *Energy Environ. Sci.* **2014**, *7*, 442.
103. Lv, Q.; Si, W.; He, J.; Sun, L.; Zhang, C.; Wang, N.; Yang, Z.; Li, X.; Wang, X.; Deng, W.; Long, Y.; Huang, C.; Li, Y. *Nat. Commun.* **2018**, *9*, 3376.
104. Dai, L.; Xue, Y.; Qu, L.; Choi, H.-J.; Baek, J.-B. *Chem. Rev.* **2015**, *115*, 4823.
105. Xu, Q.; Tang, Y.; Zhang, X.; Oshima, Y.; Chen, Q.; Jiang, D. *Adv. Mater.* **2018**, *30*, 1706330.
106. Liu, X.; Dai, L. *Nat. Rev. Mater.* **2016**, *1*, 16064.
107. Xu, Q.; Tang, Y.; Zhai, L.; Chen, Q.; Jiang, D. *Chem. Commun.* **2017**, *53*, 11690.

Chapter II: Synthesis of Two-Dimensional and One-Dimensional Covalent Organic Frameworks

Abstract

As mentioned in Chapter I, most of two-dimensional COFs are fabricated via [3 + 2], [3 + 3], [4 + 2] or [6 + 2] pathway, leading to mesopores, which is not suitable for CO_2 capture. Here we report the synthesis and decoration of 2D COFs via [4 + 4] pathway considering the good geometrical matching between building blocks. These 2D [4+4] COFs exhibit high crystallinities and surface areas with pore sizes of less than 1 nm. On the other hand, we developed a designing methodology for one-dimensional imine COFs zigzag packed by linear porous rigid organic chains consisting of V-type linkers and tetrahedral knots. This approach enables us to achieve a very high crystallinity and supermicroporosity for a series of 1D COFs considering the appropriate geometrical combination between linkers and knots. The modification of linkers achieves the introducing of heteroatoms, alkyl chains and aromatic groups into 1D COFs to realize their functionalization. We expect this strategy to open a new door for the synthesis and application of COFs.

1. Introduction

As an emerging class of ordered conjugated organic polymer materials, various COFs have been predicted, synthesized and applicated for gas storage and separation, heterogeneous catalysis, electrochemical catalysts and so on. [1-4] Among these, two-dimensional (2D) COFs are usual in topology because of the beneficial π-π interaction between conjugated layers. [1,5,6] However, these aromatic rings in each layer in turn make the building units too rigid to twist or bend in a large range. Therefore, in most of 2D COFs via [3 + 2], [3 + 3], [4 + 2] or [6 + 2] pathway, the knots often can be monomers with a large size and rigidity, while the linkers are small linear ones in order to keep the balance between the free movement of monomers during the reaction and the interlayered interaction facilitating the formation of COFs in consideration of the thermodynamics and the kinetics. [7,8] Nevertheless, even though 2D single-layered COFs with four-fold symmetry

via on-surface polymerization have been synthesized successfully, [9] forming 2D COFs via [4 + 4] pathway in the solution phase remains a big challenge when both of building units are too relatively rigid to balance the both sides; but if achieved, could show promises for gas capture applications. It is because that via [4 + 4] pathway the number of building blocks consisting of each pore are decreased by at most two-third of those via other pathways, leading to smaller pore sizes, which are crucial to achieve a high gas uptake density for gas like carbon dioxide. [10] In order to further increase the absorption capacity of COFs, many efforts have been made to optimize the pore such as decorated with hydroxyl or carboxyl groups. [11,12] Different from these “active” functional groups, the methyl group not only facilitates to form hydrogen-bond-like interactions with CO_2 to enhance the adsorption capacity but avoid interpenetration and/or severe structure distortion of frameworks. [13]

On the other hand, two-dimensional (2D) sheets and three-dimensional (3D) networks has been successfully explored for 2D and 3D covalent organic frameworks. [14,15] Their good solid-state stability, porosity and crystallinity make them potential for applications in various fields. [16,17] The dimension of COF is determined by the topology diagram where the geometry of the building blocks and their mutual matchings are key to 2D and 3D architectures. [18,19] However, it is undeveloped for 1D COFs, because that, unlike 2D and 3D structures, [20-22] the flexibility of 1D chain systems will cause their solubility in solvents and amorphousness. [23-25] Some extended structures of interwoven and interpenetrating 1D chains has already known for COFs and other material classes. [26-28] Nevertheless, their applications were limited by their lower porosity and largely decreased crystallinity after demetallation, thus designing well-defined 1D COFs remains a challenge.

Herein, we report a series of 2D COFs via [4 + 4] pathways and carry out pore functionalization with methyl groups to achieve an efficient capture and separation of CO_2. These 2D [4 + 4] COFs exhibit high BET surface areas (600~1200 $m^2\ g^{-1}$) and high crystallinities with micropores. Moreover, a series of 1D COFs consist of organic porous chains zigzag interlacing into a crystal structure. These microporous 1D COFs also possess high BET surface areas (300~1250 $m^2\ g^{-1}$) and high crystallinity with a good

designability of functionalizing by heteroatoms, alkyl chains and functional groups. The geometry of linkers and knots are proved important to the formation of 1D COFs.

2. Experimental section

Commercial reagents and solvents were purchased from Sigma-Aldrich, Kanto Chemical or Fujifilm Wako Chemical and used as received.

2.1 Monomers synthesis

4,4',4'',4'''-(pyrene-1,3,6,8-tetrayl)tetraaniline (PyTTA) [29]

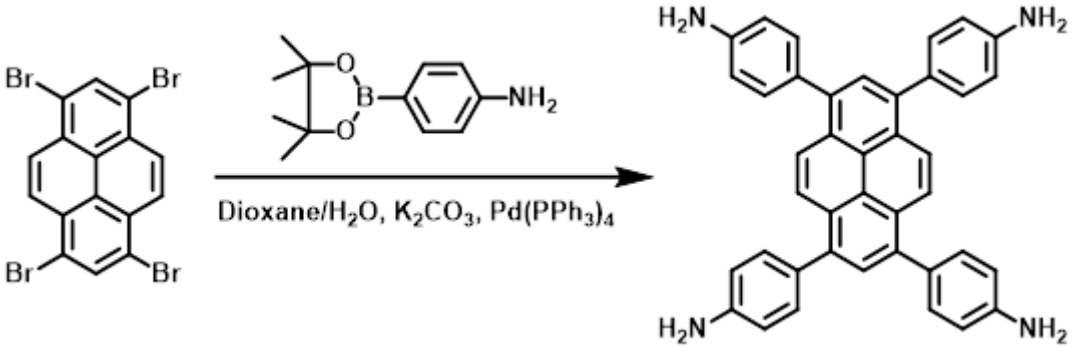

1,3,6,8 tetrabromopyrene (2.0 g, 3.86 mmol), 4-(4,4,5,5-tetramethyl-1,3,2-dioxaborolan-2-yl)aniline (3.8 g, 17.4 mmol), K_2CO_3 (2.9 g, 21.2mmol), and $Pd(PPh_3)_4$ (445 mg, 0.39 mmol) were added into dioxane/H_2O (5:1 v/v, 42 mL) and heated to reflux for 3 days. After cooling to room temperature, H_2O (50 mL) was added. The resulting precipitate was collected via filtration and was washed with H_2O and methanol. Recrystallization from dioxane, followed by drying under high vacuum to give **PyTTA** (1.97 g, 90%) as a yellow solid. ^{1}H NMR (400 MHz, DMSO-d_6) δ: 8.13 (s, 4H), 7.79 (s, 2H), 7.36, 7.34 (d, J=8.3 Hz, 8H), 6.78, 6.76 (d, J=8.3 Hz, 8H), 5.32 (s, 8H).

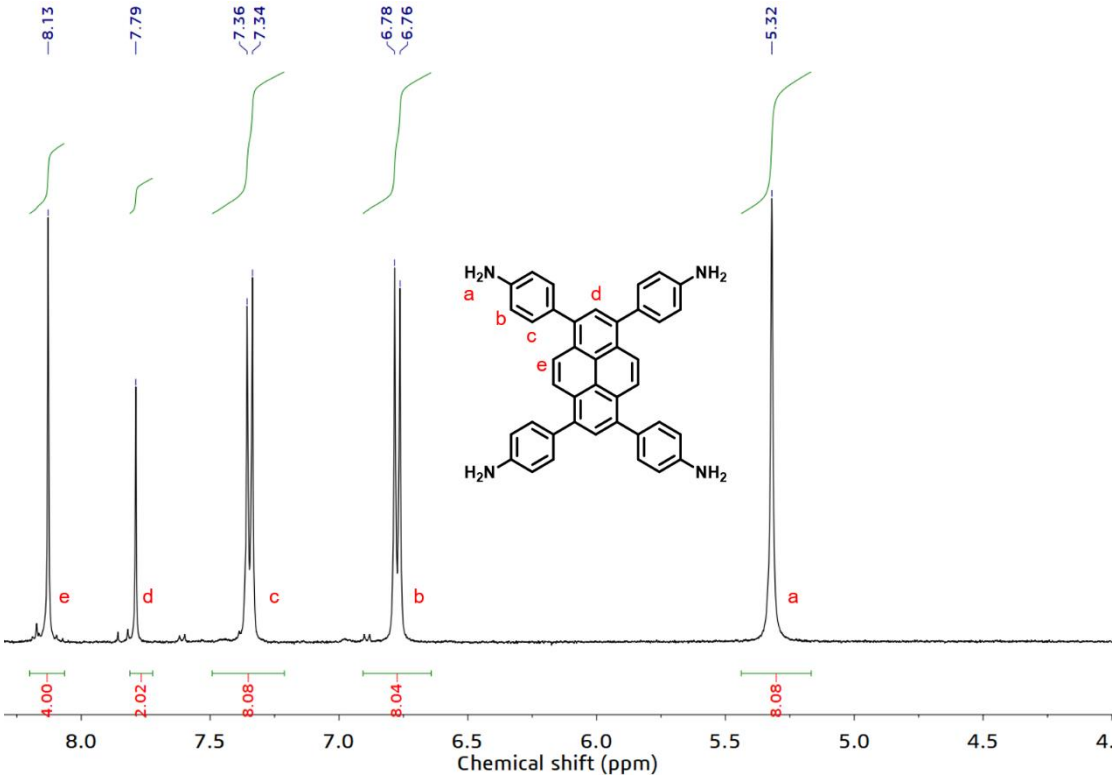

4',5'-bis(4-aminophenyl)-1,1':2',1''-terphenyl-4,4''-diamine (BATPDA) [30]

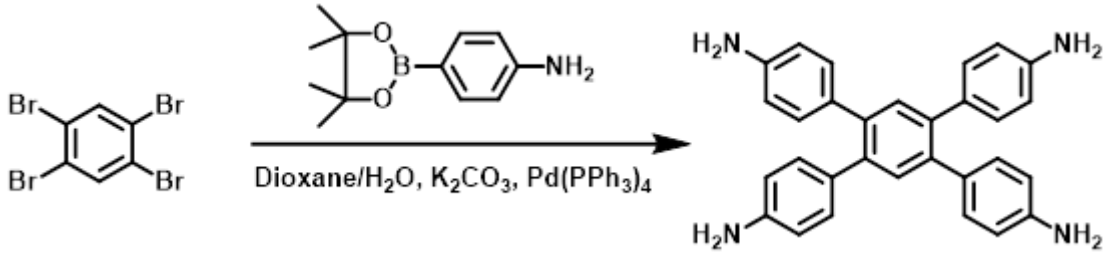

1,2,4,5-tetrabromobenzene (1.5 g, 3.8 mmol), 4-(4,4,5,5-tetramethyl-1,3,2-dioxaborolan-2-yl)aniline (3.7 g, 17.1 mmol), K_2CO_3 (2.1 g, 15.7 mmol), and $Pd(PPh_3)_4$ (439 mg, 0.38 mmol) were added into dioxane/H_2O (5:1, v/v, 36 mL) and heated to reflux for 3 days. After cooling to room temperature, H_2O (50 mL) was added. The resulting precipitate was collected via filtration and was washed with H_2O and methanol. Recrystallization from dioxane, followed by drying under high vacuum to give **BATPDA** (1.8 g, 90%) as a gray solid. ^{1}H NMR (400 MHz, $CDCl_3$) δ: 7.39 (s, 2H), 7.04, 7.02 (d, J=8.5 Hz, 8H), 6.58, 6.56 (d, J=8.1 Hz, 8H).

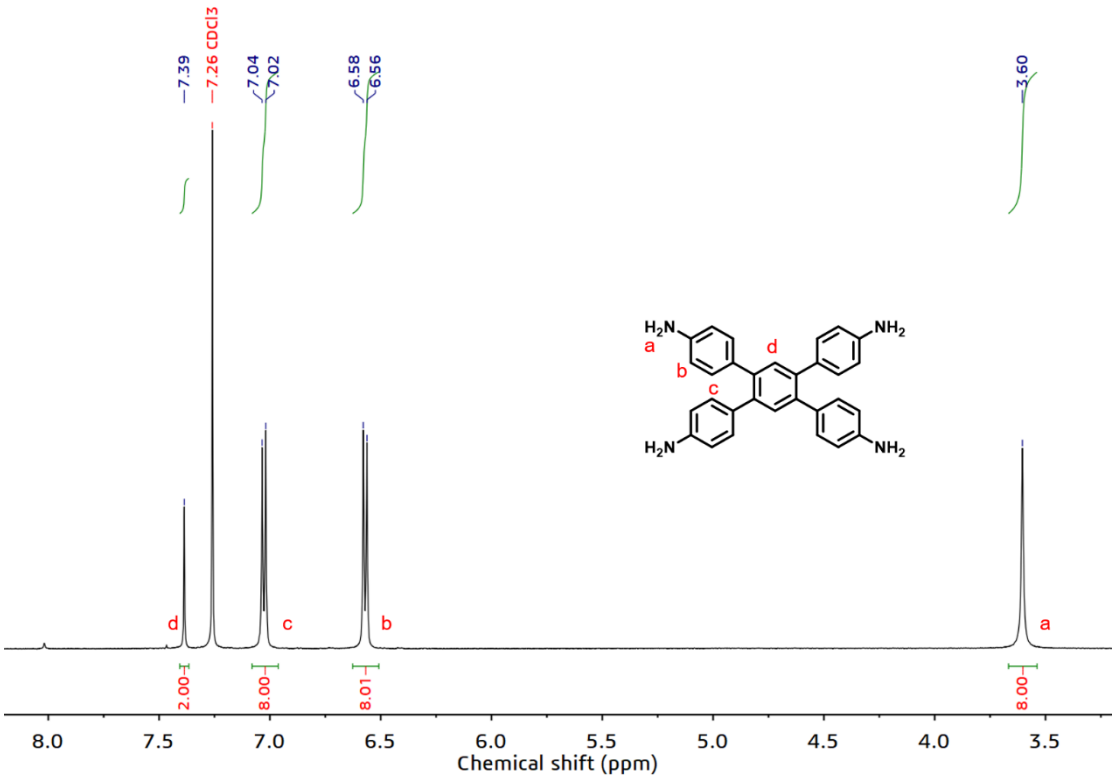

4,4',4'',4'''-(ethene-1,1,2,2-tetrayl)tetraaniline (ETTA) [31]

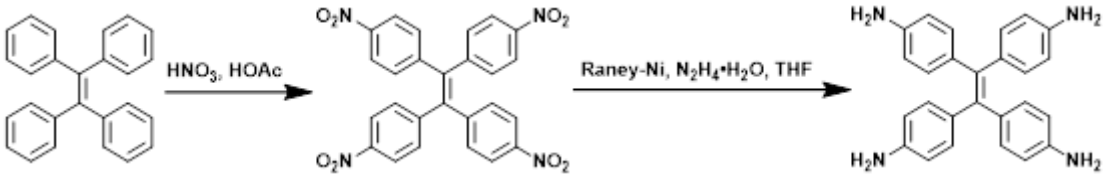

1,1,2,2-tetraphenylethylene (3.0 g, 9.0 mmol) was slowly added to a mixture of 30 mL concentrated nitric acid and 30 mL acetic acid at 0 °C with stirring. After stirring for 4 h at room temperature the solution was diluted with cold water. The resulting precipitate was filtered, dried under reduced pressure and recrystallized in 1,4-dioxane to give **1,1,2,2-tetrakis(4-nitrophenyl)ethene** (2.31g, 50%) as a yellow solid. ^{1}H NMR (400 MHz, $CDCl_3$) *δ*: 8.09-8.07 (d, *J*=8.6 Hz, 8H), 7.20-7.18 (d, *J*=8.6 Hz, 8H).

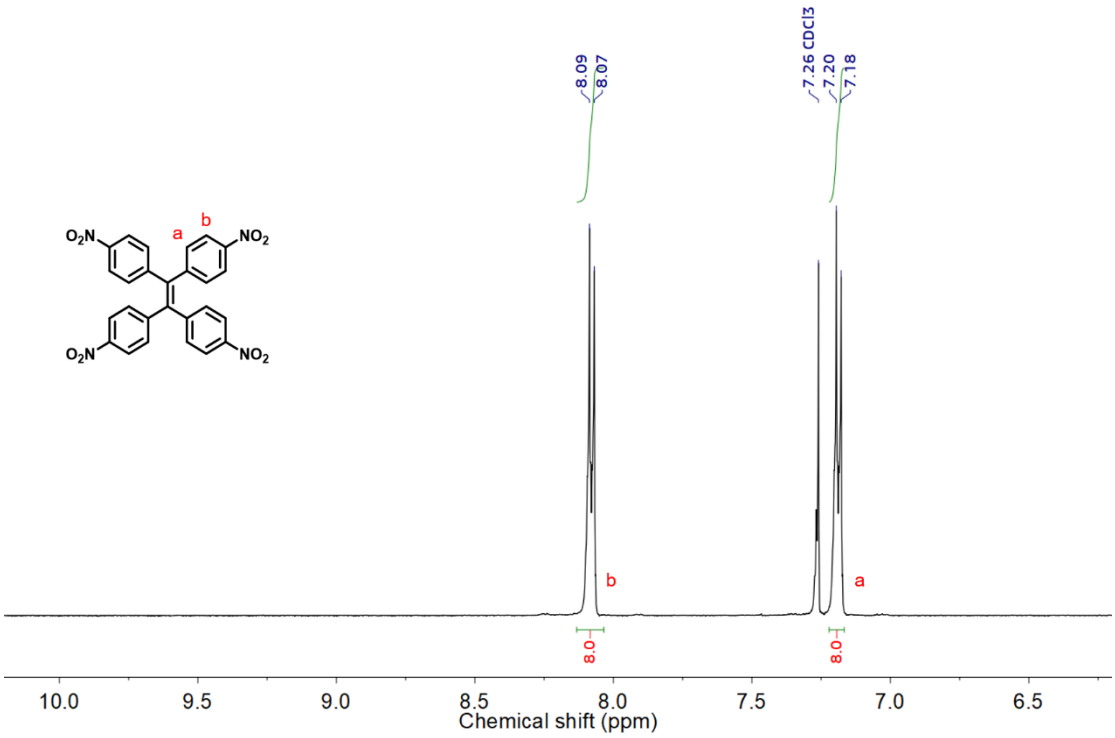

1,1,2,2-tetrakis(4-nitrophenyl)ethene (1.0 g, 1.95 mmol) was dissolved in 20 mL of anhydrous THF under N_2. Skeletal nickel catalyst slurry (4.0 g, 68 mmol) was added to the mixture with stirring. And $N_2H_4 \cdot H_2O$ (1.3 mL, 26 mmol) was then added dropwise to the stirred mixture. The resulting solution was heated to reflux for 3 h. The solution was filtered and dried under reduced pressure to give **ETTA** (688 mg, 90%) as a yellow solid. ^{1}H NMR (400 MHz, DMSO-d_6) δ: 6.56, 6.54 (d, J=8.5 Hz, 8H), 6.25, 6.22 (d, J=8.5 Hz, 8H), 4.81 (s, 8H).

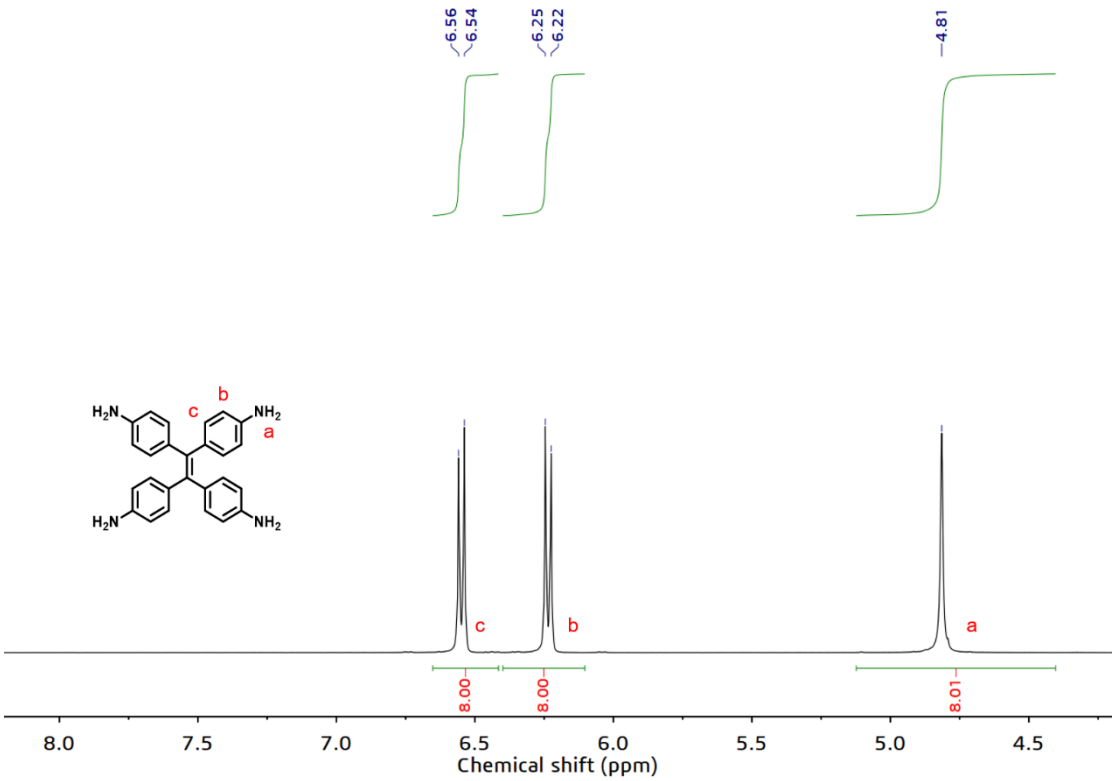

5,10,15,20-tetrakis(4-aminophenyl)porphiny (TAPP) [32]

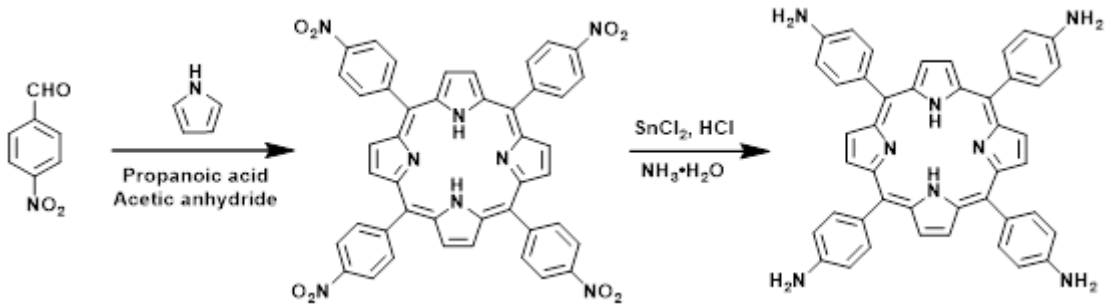

4-nitrobenzaldehyde (21.76 g, 144 mmol) were dissolved in acetic anhydride (24 mL)/ propanoic acid (600 mL). The resulting solution was stirred for 2 h at 140 °C, and pyrrole (10.0 mL, 144 mmol) was added to the resulting mixture dropwisely, which was stirred further for 2 h. The reaction mixture was filtered and washed with methanol until the filtrate appeared colorless. The filtrate was then concentrated under vacuum, and the resulting crude solid was recrystallized in pyridine. The filtrate was washed thoroughly with pyridine (500 mL) to give compound **5,10,15,20-tetrakis(4-nitrophenyl)porphyrin** (5.1 g, 18%) as a purple solid. HRMS-ESI: Calculated for $C_{44}H_{26}N_8O_8$ $[M + H]^+$ m/z = 794.2, found m/z = 794.3.

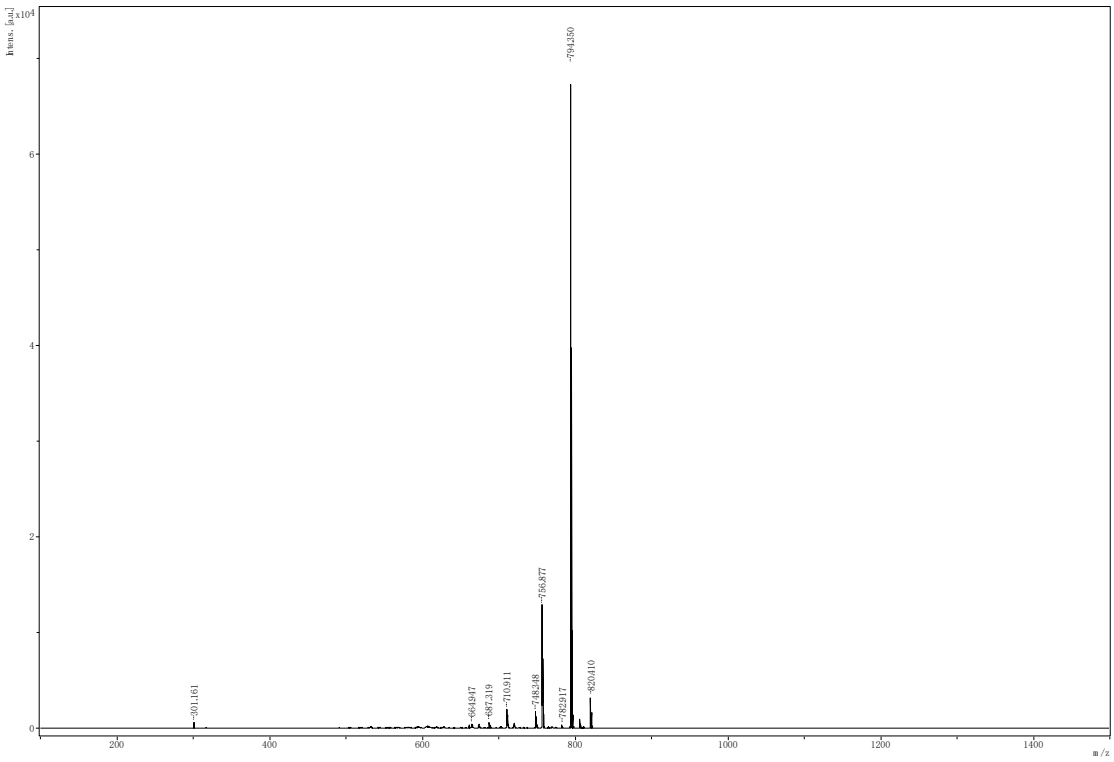

5,10,15,20-tetrakis(4-nitrophenyl)porphyrin (1.16 g, 1.28 mmol) and $SnCl_2$ (2.25 g, 10.0 mmol) were added in concentrated HCl (55 mL). After degassing and backfilling N_2 three times, the resulting solution was stirred for 18 h at 70 °C. The reaction mixture was neutralized by $NH_3 \cdot H_2O$, filtered and washed with acetone until the filtrate appeared colorless. The filtrate was then concentrated under vacuum, and the resulting crude solid was recrystallized in $CHCl_3$ to give compound **TAPP** (300 mg, 35%) as a purple solid. ^1H NMR (400 MHz, DMSO-d_6) δ: 8.88 (s, 8H), 7.86, 7.84 (d, J=8.3 Hz, 8H), 7.10, 7.08 (d, J=8.5 Hz, 8H), 4.05 (s, 8H), -2.68 (s, 2H).

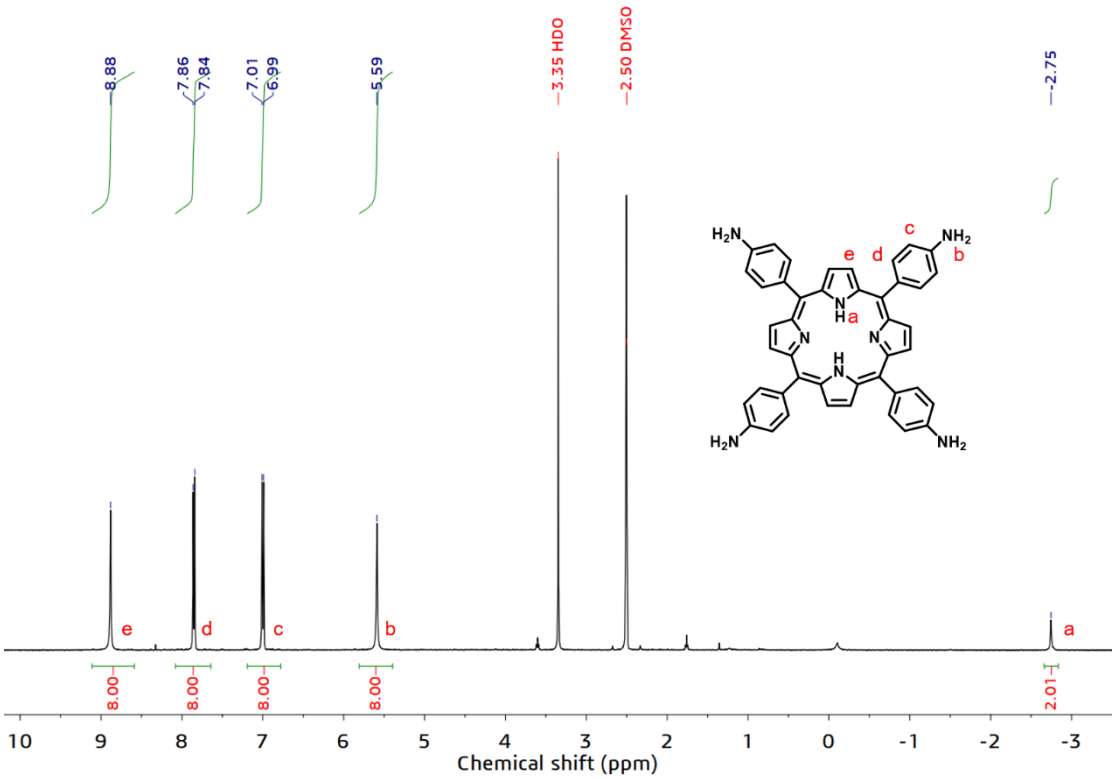

4',5'-bis(4-formylphenyl)-1,1':2',1''-terphenyl-4,4''-dicarbaldehyde (BFTDC) [33]

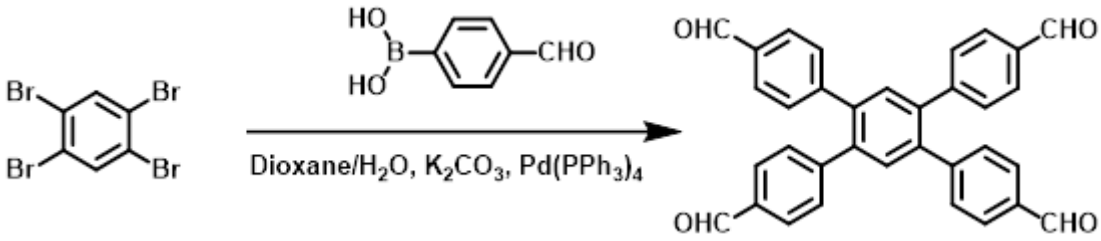

1,2,4,5-tetrabromobenzene (1.91 g, 4.84 mmol), 4-formylphenyl boronic acid (1.60 g, 10.64 mmol), K_2CO_3 (2.68 g, 19.4 mmol) and $Pd(PPh_3)_4$ (578 mg, 0.5 mmol) in dioxane/H_2O (5:1 v/v, 72 mL) were degassed and backfilled N_2 three times. The suspension was stirred under N_2 at 100 °C for 72 h. After cooling to room temperature, the mixture was concentrated and then extracted with EtOAc. The organic phase was dried over anhydrous $MgSO_4$ and then concentrated under reduced pressure to remove the solvent. The crude product was purified by silica gel column chromatography to afford **BFTDC** (1.92 g, 80%). ^{1}H NMR (400 MHz, $CDCl_3$) δ: 10.00 (s, 4H), 7.81, 7.79 (d, J=8.4 Hz, 8H), 7.60 (s, 2H), 7.40, 7.38 (d, J=8.2 Hz, 8H).

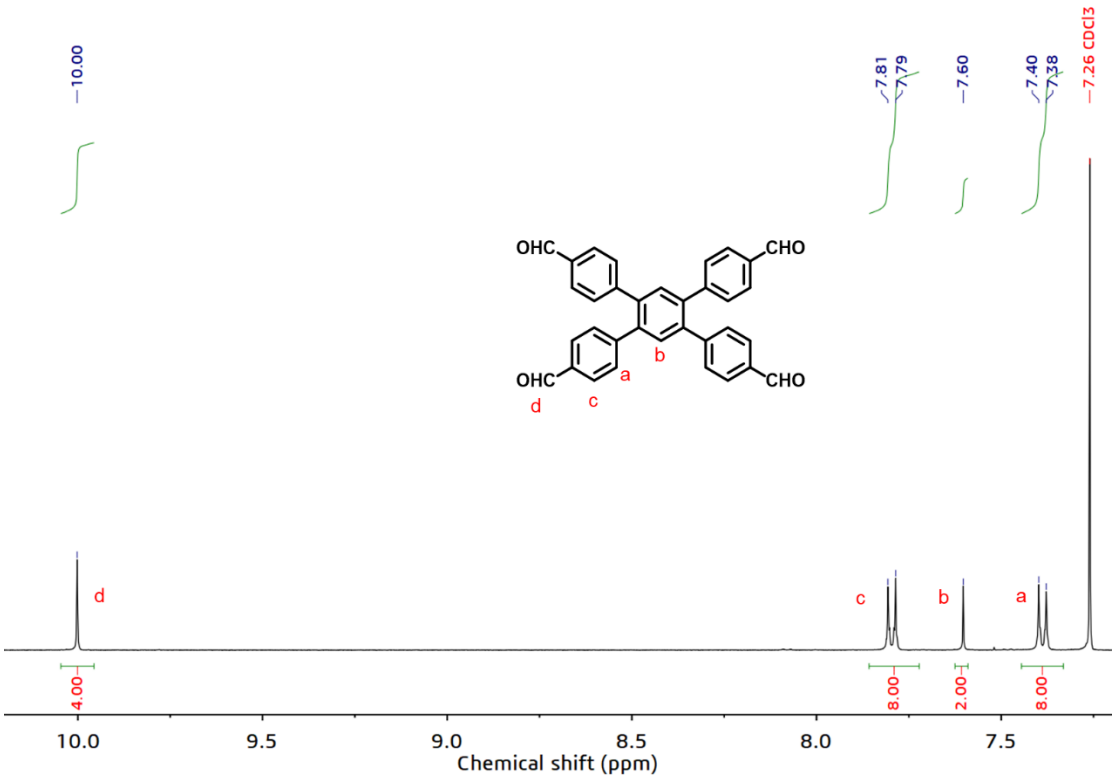

4',5'-bis(4-formylphenyl)-3',6'-dimethyl-[1,1':2',1''-terphenyl]-4,4''-dicarbaldehyde (BFDMTDC) [33]

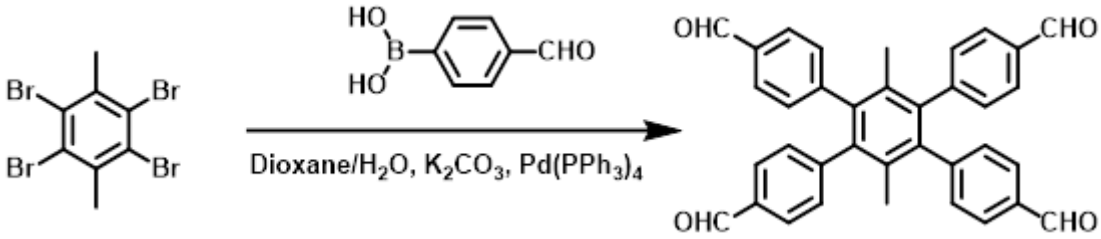

2,3,5,6-Tetrabromo-*p*-xylene (2.0 g, 4.74 mmol), 4-formylphenyl boronic acid (1.56 g, 10.42 mmol), K_2CO_3 (2.62 g, 19.0 mmol) and $Pd(PPh_3)_4$ (578 mg, 0.5 mmol) in dioxane/H_2O (5:1 v/v, 66 mL) were degassed and backfilled N_2 three times. The suspension was stirred under N_2 at 100 °C for 72 h. After cooling to room temperature, the mixture was concentrated and then extracted with EtOAc. The organic phase was dried over anhydrous $MgSO_4$ and then concentrated under reduced pressure to remove the solvent. The crude product was purified by silica gel column chromatography to afford **BFDMTDC** (1.5 g, 60%). ^{1}H NMR (400 MHz, $CDCl_3$) δ: 9.91 (s, 4H), 7.72, 7.70 (d, J=8.3 Hz, 8H), 7.25, 7.23 (d, J=8.1 Hz, 8H), 1.77 (s, 6H).

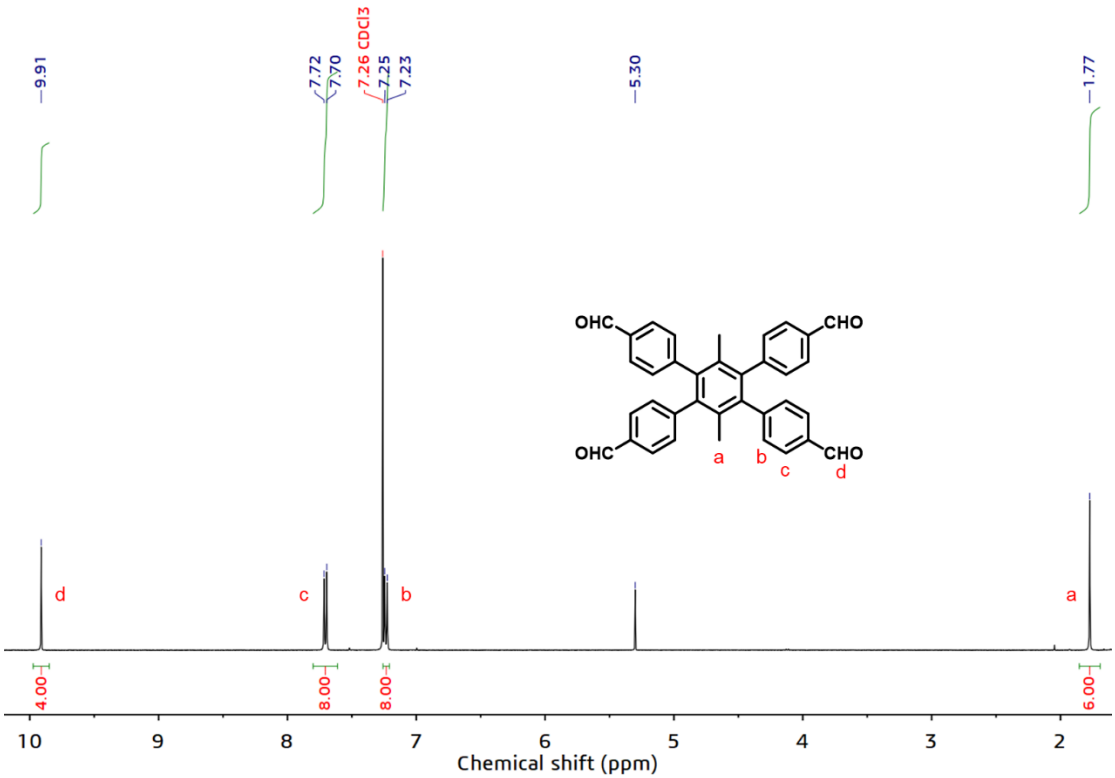

1,1':3',1''-terphenyl-4,4''-dicarbaldehyde (*m*-TPDC) [34]

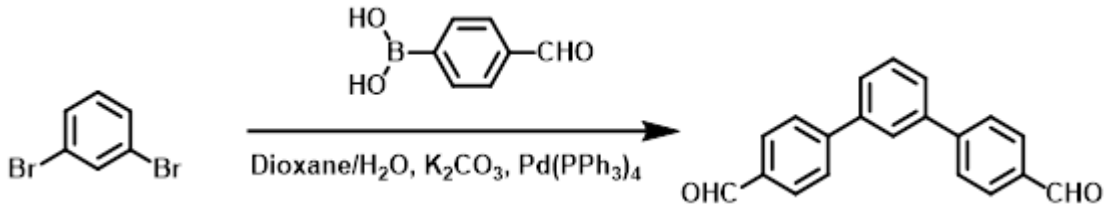

1,3-dibromobenzene (1.0g, 4.24 mmol), 4-formylphenyl boronic acid (2.50g, 17.0 mmol), K_2CO_3 (2.35 g, 17.0 mmol) and $Pd(PPh_3)_4$ (160 mg, 0.14 mmol) in dioxane/H_2O (5:1 v/v, 36 mL) were degassed and backfilled N_2 three times. The suspension was stirred under N_2 at 100 °C for 72 h. After cooling to room temperature, the mixture was concentrated and then extracted with EtOAc. The organic phase was dried over anhydrous $MgSO_4$ and then concentrated under reduced pressure to remove the solvent. The crude product was purified by silica gel column chromatography to afford ***m*-TPDC** (1.10 g, 91%). ^{1}H NMR (400 MHz, $CDCl_3$) *δ*:10.09 (s, 2H), 8.00, 7.99 (d, *J*=8.1 Hz, 4H), 7.88 (s, 1H), 7.83, 7.81 (d, *J*=8.1 Hz, 4H), 7.70, 7.69, 7.68 (t, *J*=7.4 Hz, 9.0 Hz, 2H), 7.62-7.59 (m, *J*=7.9 Hz, 15.4 Hz, 1H).

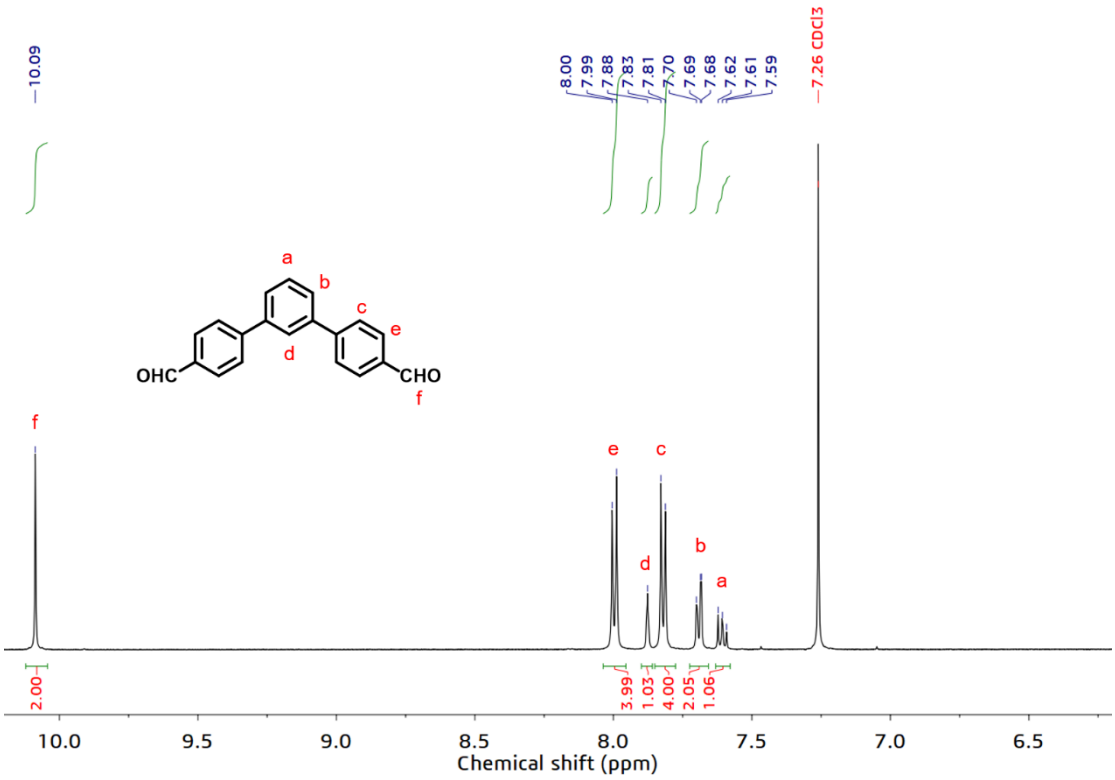

4,4'-(pyridine-2,6-diyl)dibenzaldehyde (PDDC) [35]

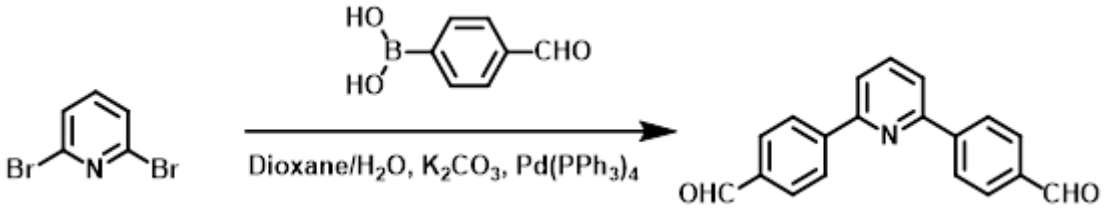

2,6-dibromopyridine (0.94 g, 4.0 mmol), 4-formylphenyl boronic acid (1.26 g, 8.4 mmol), K_2CO_3 (2.21 g, 16.0 mmol) and $Pd(PPh_3)_4$ (160 mg, 0.14 mmol) in dioxane/H_2O (5:1 v/v, 36 mL) were degassed and backfilled N_2 three times. The suspension was stirred under N_2 at 100 °C for 72 h. After cooling to room temperature, the mixture was concentrated and then extracted with EtOAc. The organic phase was dried over anhydrous $MgSO_4$ and then concentrated under reduced pressure to remove the solvent. The crude product was purified by silica gel column chromatography to afford **PDDC** (488 mg, 43%). ^{1}H NMR (400 MHz, $CDCl_3$) δ: 10.11 (s, 2H), 8.34, 8.32 (d, J=8.3 Hz, 4H), 8.05, 8.03 (d, J=8.5 Hz, 4H), 7.92-7.96 (m, 1H), 7.86-7.84 (t, J=7.3 Hz, 8.4 Hz, 2H).

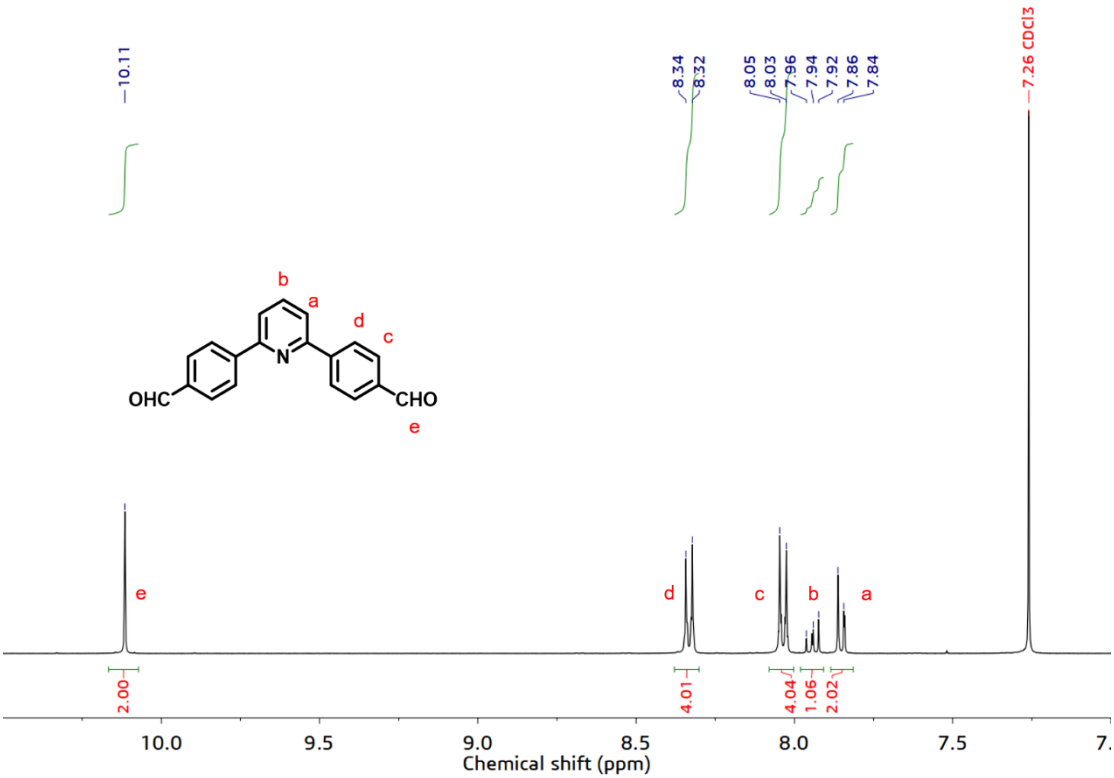

5'-phenyl-1,1':3',1''-terphenyl-4,4''-dicarbaldehyde (PTPDC) [36,37]

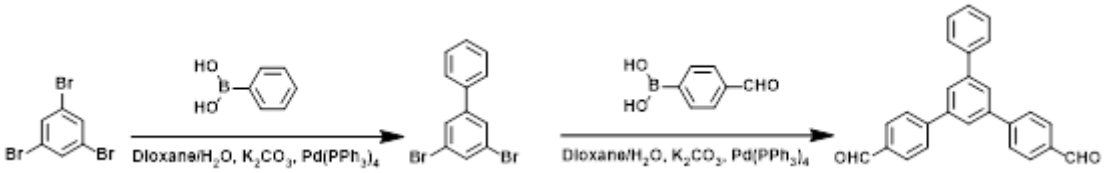

1,3,5-tribromobenzene (5.1 g, 16.2 mmol), phenylboronic acid (1.65 g, 13.6 mmol), K_2CO_3 (7.46 g, 17.0 mmol) and $Pd(PPh_3)_4$ (270 mg, 0.24 mmol) in toluene/ethanol (5:1 v/v, 36 mL) were degassed and backfilled N_2 three times. The suspension was stirred under N_2 at 100 °C for 72 h. After cooling to room temperature, the mixture was concentrated and then extracted with EtOAc. The organic phase was dried over anhydrous $MgSO_4$ and then concentrated under reduced pressure to remove the solvent. The crude product was purified by silica gel column chromatography to afford **3,5-dibromo-1,1'-biphenyl**. Yield: (3.03 g, 60%). ^{1}H NMR (400 MHz, $CDCl_3$) δ: 7.66, 7.65 (d, J=1.7 Hz, 2H,), 7.64 (m, 1H), 7.54-7.52 (m, 2H), 7.47-7.43 (m, 2H), 7.41-7.39 (m, 1H).

3,5-dibromo-1,1'-biphenyl (468 mg, 1.5 mmol), phenylboronic acid (495 mg, 3.3 mmol), K_2CO_3 (0.83 g, 6.0 mmol) and $Pd(PPh_3)_4$ (230 mg, 0.23 mmol) in toluene/ethanol (5:1 v/v, 20 mL) were degassed and backfilled N_2 three times. The suspension was stirred under N_2 at 100 °C for 72 h. After cooling to room temperature, the mixture was concentrated and

then extracted with EtOAc. The organic phase was dried over anhydrous $MgSO_4$ and then concentrated under reduced pressure to remove the solvent. The crude product was purified by silica gel column chromatography to afford **PTPDC**. (391 mg, 72%). ^{1}H NMR (400 MHz, $CDCl_3$) δ: 10.10 (s, 2H), 8.03, 8.01 (d, J=8.4 Hz, 1H), 7.88-7.85 (m, 7H), 7.71-7.69 (m, 2H), 7.53-7.51 (t, J=7.2 Hz, 14.9 Hz, 2H), 7.45-7.42 (t, J=7.4 Hz, 14.7 Hz, 1H).

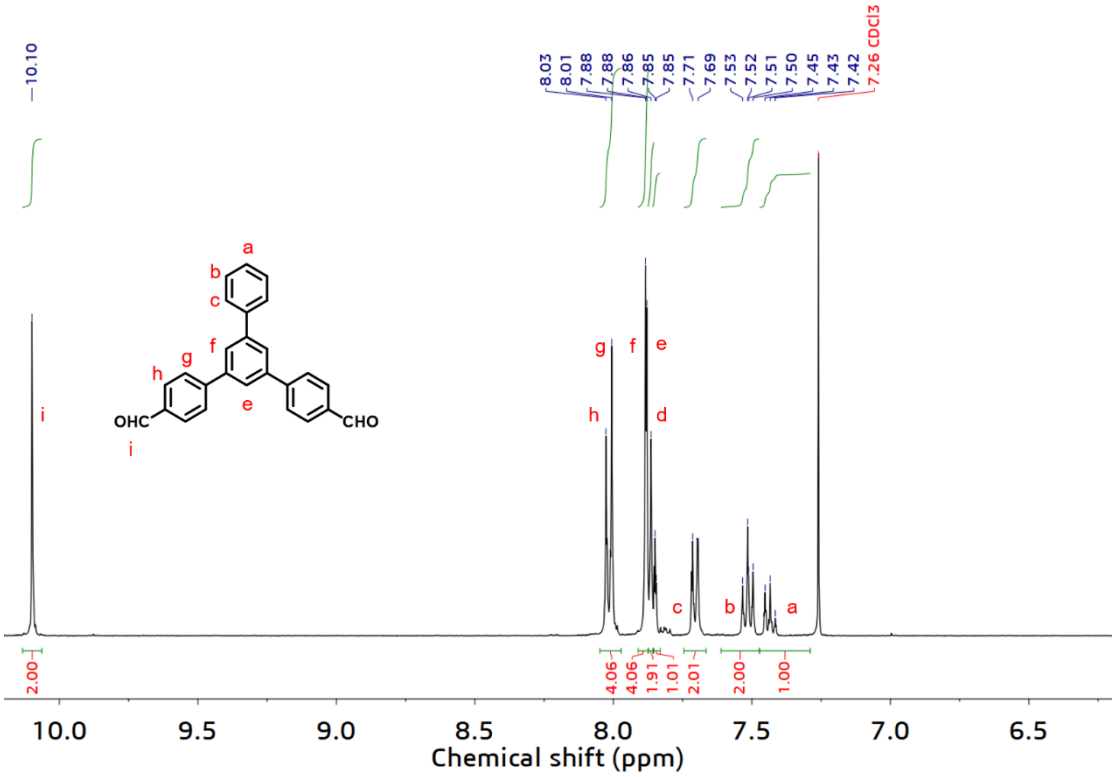

2',4',5',6'-tetrafluoro-[1,1':3',1''-terphenyl]-4,4''-dicarbaldehyde (TF-*m*-TPDC) [34]

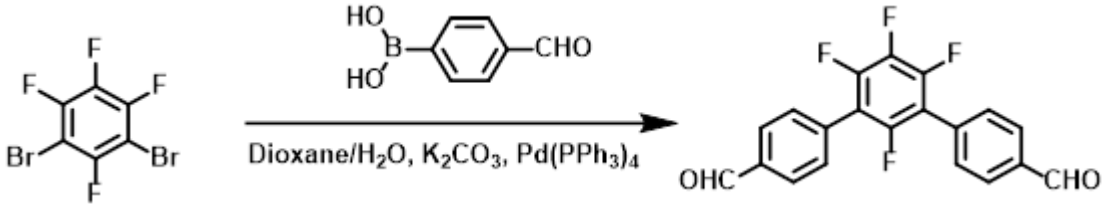

1,3-dibromo-2,4,5,6-tetrafluorobenzene (616 mg, 2.0 mmol), 4-formylphenyl boronic acid (630 mg, 4.2 mmol), K_2CO_3 (1.2 g, 8.7 mmol) and $Pd(PPh_3)_4$ (228 mg, 0.2 mmol) in dioxane/H_2O (5:1 v/v, 18 mL) were degassed and backfilled N_2 three times. The suspension was stirred under N_2 at 100 °C for 72 h. After cooling to room temperature, the mixture was concentrated and then extracted with EtOAc. The organic phase was dried over anhydrous $MgSO_4$ and then concentrated under reduced pressure to remove the solvent. The crude product was purified by silica gel column chromatography to afford **TF-*m*-TPDC** (179 mg,

25%). ^{1}H NMR (400 MHz, $CDCl_3$) δ:10.10 (s, 2H), 8.03, 8.00 (d, J=8.3 Hz, 4H), 7.67, 7.65 (d, J=7.4 Hz, 4H).

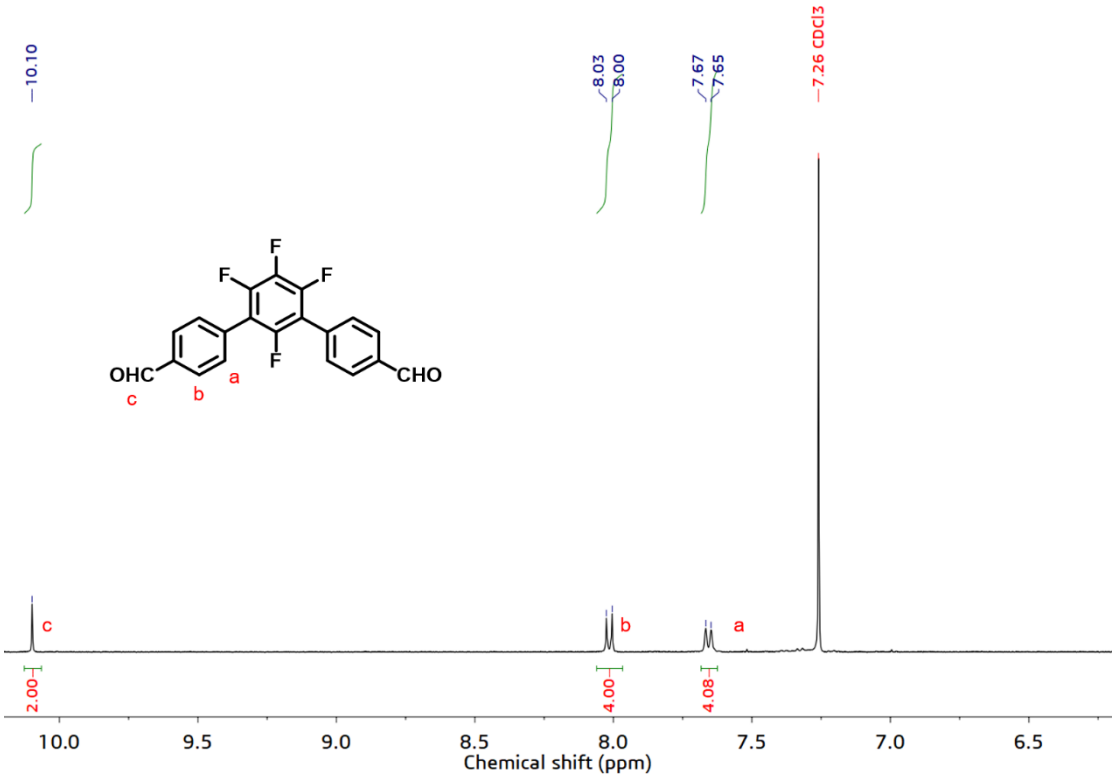

5'-(trimethylsilyl)-1,1':3',1''-terphenyl-4,4''-dicarbaldehyde (TMS-*m*-TPDC) [38]

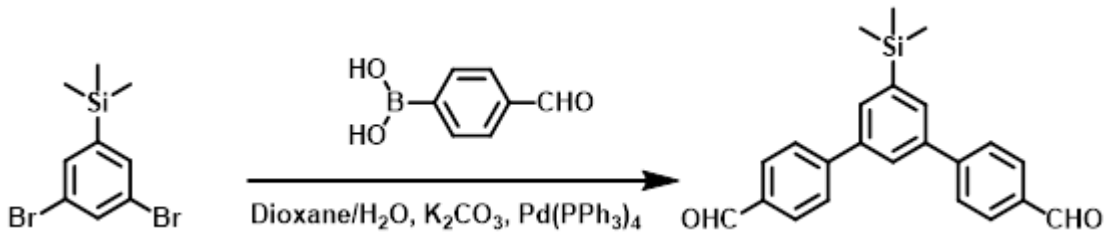

(3,5-dibromophenyl)trimethylsilane (616 mg, 2.0 mmol), 4-formylphenyl boronic acid (630 mg, 4.2 mmol), K_2CO_3 (1.1 g, 8.0 mmol) and $Pd(PPh_3)_4$ (162 mg, 0.14 mmol) in THF/H_2O (5:1 v/v, 18 mL) were degassed and backfilled N_2 three times. The suspension was stirred under N_2 at 90 °C for 72 h. After cooling to room temperature, the mixture was concentrated and then extracted with EtOAc. The organic phase was dried over anhydrous $MgSO_4$ and then concentrated under reduced pressure to remove the solvent. The crude product was purified by silica gel column chromatography to afford **TMS-*m*-TPDC** (346 mg, 48%). ^{1}H NMR (400 MHz, $CDCl_3$) δ: 10.09 (s, 2H), 8.01, 7.99 (d, J=8.3 Hz, 4H), 7.83 (s, 3H), 7.80-7.79 (t, J=4.8 Hz, 6.6 Hz, 4H), 0.38 (s, 9H).

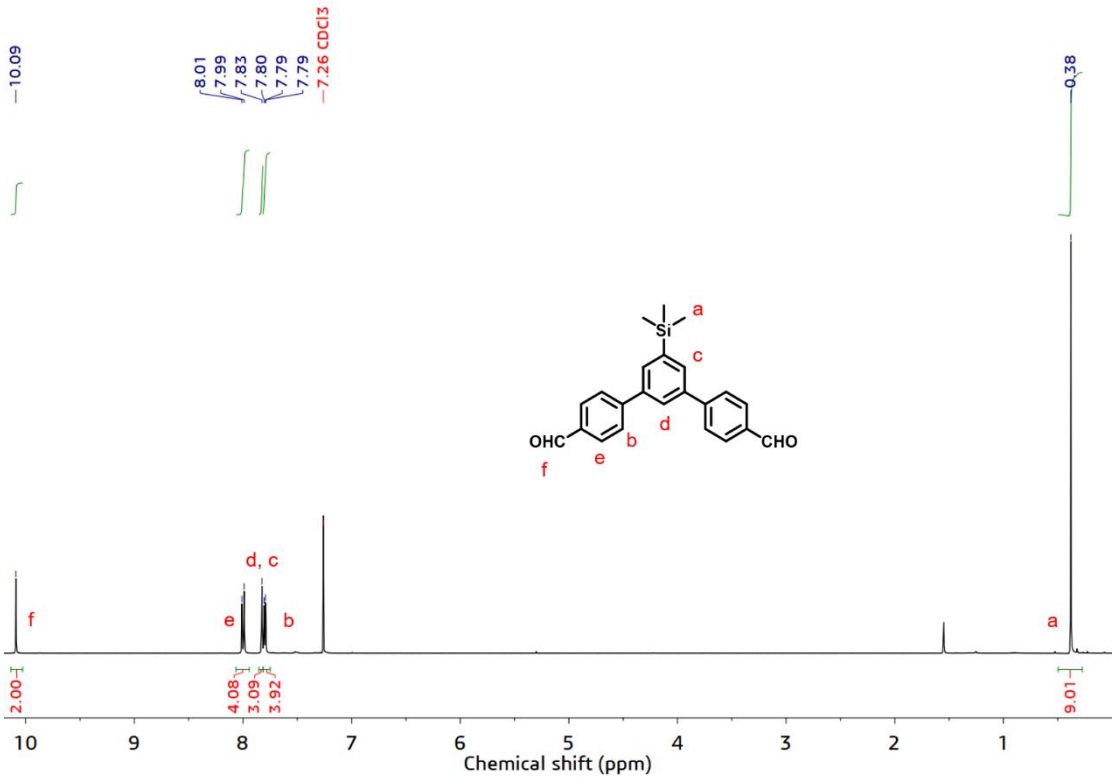

4,4'-(9-ethyl-9H-carbazole-3,6-diyl)dibenzaldehyde (ECDDB) [39]

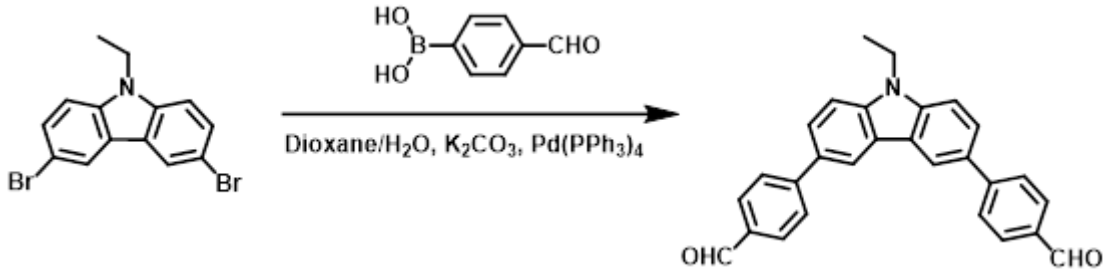

1,3-dibromobenzene (1.5 g, 4.25 mmol), 4-formylphenyl boronic acid (1.35 g, 9.0 mmol), K_2CO_3 (4.5 g, 51.0 mmol) and $Pd(PPh_3)_4$ (400 mg, 0.35 mmol) in THF/H_2O (5:1 v/v, 48 mL) were degassed and backfilled N_2 three times. The suspension was stirred under N_2 at 100 °C for 72 h. After cooling to room temperature, the mixture was concentrated and then extracted with EtOAc. The organic phase was dried over anhydrous $MgSO_4$ and then concentrated under reduced pressure to remove the solvent. The crude product was purified by silica gel column chromatography to afford **ECDDB** (430 mg, 25%). ^{1}H NMR (400 MHz, $CDCl_3$) *δ*:10.08 (s, 2H), 8.46 (s, 2H), 8.01, 7.99 (d, *J*=8.3 Hz, 4H), 7.92, 7.90 (d, *J*=8.3 Hz, 4H), 7.83 (d, *J*=1.9 Hz, 1H), 7.81 (d, *J*=1.8 Hz, 1H), 7.56, 7.54, 7.52 (t, *J*=8.5 Hz, 15.7 Hz, 2H), 4.49-4.44 (m, *J*=7.2 Hz, 14.5 Hz, 21.7 Hz, 2H), 1.52, 1.50 (t, *J*=10.3 Hz, 17.6 Hz, 3H).

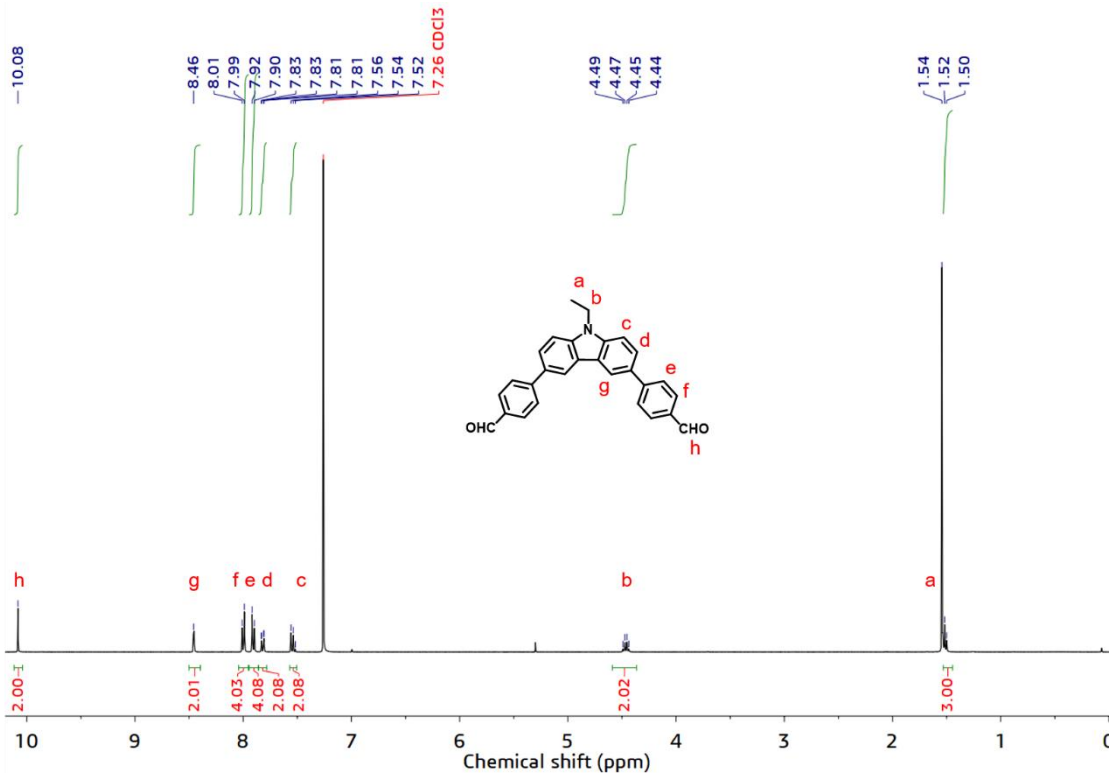

2.2 COFs synthesis

PyTTA-BFTDC COF

A Pyrex tube measuring 10 × 8 mm (o.d × i.d) was charged with PyTTA (11.5 mg, 0.02 mmol), BFTDC (9.9 mg, 0.02 mmol), mesitylene (0.48 mL), dioxane (0.32 mL), and 6 M aqueous acetic acid (0.08 mL). The tube was flash frozen at in liquid N_2 bath for three freeze-pump-thaw cycles and flame sealed. The reaction was heated at 120 ºC for 120 hours yielding a yellow precipitate at the bottom of the tube, which was isolated by filtration with THF. The wet sample was then transferred to a Soxhlet extractor and thoroughly washed with THF for 48 h and dried under vaccum at 100 ºC for 6 h. Calcd. for $C_{74}H_{44}N_4$: C, 89.85%; N, 5.66%; H, 4.39% (C:N=15.87:1:0.78). Found C, 84.89%; N, 3.22% (C:N=26.36:1) by XPS and C, 72.17%; N, 4.59%; H, 4.01% (C:N:H=15.72:1:0.87) by elemental analysis.

PyTTA-BFDMTDC COF

The synthesis was carried out following the same protocol as for PyTTA-BFTDC COF, by replacing BFTDC with BFDMTDC (10.5 mg, 0.02 mmol) and changing the amount of mesitylene and dioxane to 0.60 mL/0.30 mL. Calcd. for $C_{76}H_{48}N_4$: C, 89.74%; N, 5.51%; H,

4.75% (C:N:H=16.29:1:0.86). Found C, 92.01%; N, 4.95% (C:N=18.59:1) by XPS and C, 80.61%; N, 4.87%; H, 4.73% (C:N:H=16.55:1:0.97) by elemental analysis.

BATPDA-BFTDC COF

The synthesis was carried out following the same protocol as for PyTTA-BFTDC COF, by replacing PyTTA with BATPDA (8.8 mg, 0.02 mmol) and changing the amount of mesitylene and dioxane to 0.60 mL/0.30 mL. Calcd. for $C_{64}H_{40}N_4$: C, 88.86%; N, 6.48%; H, 4.66% (C:N:H=13.71:1:0.72). Found C, 88.15%; N, 5.37% (C:N=16.42:1) by XPS and C, 77.41%; N, 5.30%; H, 4.58% (C:N:H=14.61:1:0.86) by elemental analysis.

BATPDA-BFDMTDC COF

The synthesis was carried out following the same protocol as for PyTTA-BFTDC COF, by replacing PyTTA with BATPDA (8.8 mg, 0.02 mmol), *m*-TPDC with BFDMTDC (10.5 mg, 0.02 mmol) and changing the amount of mesitylene and dioxane to 0.4 mL/0.4 mL. Calcd. for $C_{66}H_{44}N_4$: C, 88.76%; N, 6.27%; H, 4.97% (C:N:H=14.16:1:0.79). Found C, 90.36%; N, 5.18% (C:N=17.44:1) by XPS and C, 77.05%; N, 4.86%; H, 4.90% (C:N:H=15.85:1:1.01) by elemental analysis.

PyTTA-*m*-TPDC 1D COF

A Pyrex tube measuring 10 × 8 mm (o.d × i.d) was charged with PyTTA (11.5 mg, 0.02 mmol), *m*-TPDC (11.4 mg, 0.04 mmol), mesitylene (0.6 mL), dioxane (0.2 mL), and 6 M aqueous acetic acid (0.08 mL). The tube was flash frozen at in liquid N_2 bath for three freeze-pump-thaw cycles and flame sealed. The reaction was heated at 120 ºC for 120 hours yielding a yellow precipitate at the bottom of the tube, which was isolated by filtration with THF. The wet sample was then transferred to a Soxhlet extractor and thoroughly washed with THF for 48 h and dried under vaccum at 100 ºC for 6 h. Calcd. for $C_{160}H_{100}N_8$: C, 90.03%; N, 5.25%; H, 4.72% (C:N:H=17.15:1:0.90). Found C, 90.65%; N, 5.49% (16.51:1) by XPS and C, 82.26%; N, 5.06%; H, 4.69% by elemental analysis.

BATPDA-*m*-TPDC 1D COF

The synthesis was carried out following the same protocol as for PyTTA-*m*-TPDC 1D COF, by replacing PyTTA with BATPDA (8.8 mg, 0.02 mmol). Calcd. for $C_{140}H_{92}N_8$: C, 89.14%; N, 5.94%; H, 4.92% (C:N=15.01:1:0.83). Found C, 90.40%; N, 6.30% (C:N=14.35:1) by XPS and C, 84.72%; N, 5.83%; H, 4.83% by elemental analysis..

ETTA-*m*-TPDC 1D COF

The synthesis was carried out following the same protocol as for PyTTA-*m*-TPDC 1D COF, by replacing PyTTA with ETTA (7.9 mg, 0.02 mmol) and changing the amount of mesitylene and dioxane to 0.4 mL/0.4 mL. Calcd. for $C_{132}H_{88}N_8$: C, 88.76%; N, 6.27% (C:N=14.16:1:0.47). Found C, 90.75%; N, 6.28%; H, 2.97% (C:N:H=14.45:1) by XPS and C, 84.37%; N, 5.89%; H, 5.00% by elemental analysis.

PyTTA-PDDC 1D COF

The synthesis was carried out following the same protocol as for PyTTA-*m*-TPDC 1D COF, by replacing *m*-TPDC with PDDC (11.5 mg, 0.04 mmol) and using 1,2-dichlorobenzene (0.8 mL) as the solvent. Calcd. for $C_{156}H_{96}N_{12}$: C, 87.62%; N, 7.86%; H, 4.52% (C:N:H=11.15:1:0.58). Found C, 85.45%; N, 6.83% (C:N=12.51:1) by XPS and C, 77.89%; N, 6.89%; H, 5.06% (C:N:H=11.30:1:0.73) by elemental analysis.

PyTTA-PTPDC 1D COF

The synthesis was carried out following the same protocol as for PyTTA-*m*-TPDC 1D COF, by replacing *m*-TPDC with PTPDC (14.5 mg, 0.04 mmol). Calcd. for $C_{184}H_{116}N_8$: C, 90.61%; N, 4.95%; H, 4.44% (C:N=19.74:1:0.90). Found C, 88.09%; N, 4.50% (C:N=19.58:1) by XPS and C, 82.41%; N, 4.41%; H, 4.49% (C:N:H=18.69:1:1.02) by elemental analysis.

PyTTA-TF-*m*-TPDC 1D COF

The synthesis was carried out following the same protocol as for PyTTA-*m*-TPDC 1D COF, by replacing *m*-TPDC with TF-*m*-TPDC (14.3 mg, 0.04 mmol) and changing the amount of mesitylene and dioxane to 0.4 mL/0.4 mL. Calcd. for $C_{160}H_{84}N_8F_{16}$: C, 79.33%; F, 12.55%;

N, 4.63%; H, 3.49% (C:F:N:H=17.13:2.71:1:0.75). Found C, 77.63%; F, 15.62%; N, 4.59% (C:F:N=16.91:3.40:1) by XPS and C, 82.41%; N, 4.41%; H, 4.49% (C:N:H=18.69:1:1.02) by elemental analysis.

PyTTA-ECDDB 1D COF

The synthesis was carried out following the same protocol as for PyTTA-*m*-TPDC 1D COF, by replacing *m*-TPDC with ECDDB (16.1 mg, 0.04 mmol) and changing the amount of mesitylene and dioxane to 0.4 mL/0.4 mL. Calcd. for $C_{192}H_{128}N_{12}$: C, 88.59%; N, 6.46%; H, 4.95% (C:N:H=13.71:1:0.77). Found C, 85.97%; N, 5.16% (C:N=16.66:1) by XPS and C, 79.32%; N, 5.60%; H, 5.10% (C:N:H=14.16:1:0.91) by elemental analysis.

ETTA-ECDDB 1D COF

The synthesis was carried out following the same protocol as for PyTTA-*m*-TPDC 1D COF, by replacing PyTTA with ETTA (7.9 mg, 0.02 mmol), *m*-TPDC with ECDDB (16.1 mg, 0.04 mmol) and mesitylene/dioxane with 1,2-dichlorobenzene (0.4 mL)/butanol (0.4 mL). Calcd. for $C_{164}H_{116}N_{12}$: C, 85.23%; N, 7.45%; H, 2.32% (C:N=11.44:1:0.31). Found C, 90.31%; N, 7.37% (C:N=12.25:1) by XPS and C, 84.06%; N, 6.72%; H, 5.67% (C:N:H=12.51:1:0.84) by elemental analysis.

TAPP-ECDDB 1D COF

The synthesis was carried out following the same protocol as for PyTTA-*m*-TPDC 1D COF, by replacing PyTTA with TAPP (15.9 mg, 0.02 mmol), *m*-TPDC with ECDDB (16.1 mg, 0.04 mmol). Calcd. for $C_{200}H_{136}N_{20}$: C, 85.20%; N, 9.94%; H, 4.86% (C:N=8.57:1:0.49). Found C, 85.50%; N, 8.17% (C:N=10.47:1) by XPS and C, 79.25%; N, 9.32%; H, 4.73% (C:N:H=8.50:1:0.51) by elemental analysis.

3. Characterization

Matrix-assisted laser desorption ionization time-of-flight mass (MALDI-TOF MS) spectra were recorded on an Bruker Solarix molecular mass spectrometer. Fourier transform

infrared (FT-IR) spectra were recorded on a JASCO FT-IR-6100 infrared spectrometer. Solution phase ^{1}H NMR spectroscopy was carried out using a Bruker AvanceIII400 MHz NMR spectrometer using the residual protonated solvent resonance as an internal standard. Solid-state ^{13}C cross-polarization total suppression of sidebands (^{13}C CP/TOSS) and cross-polarization magic angle spinning nuclear magnetic resonance (^{13}C CP/MAS NMR) spectra were recorded on a Bruker biospin AvanceIII500 (500 MHz) NMR spectrometer using the rotor frequency of 10 kHz. Powder X-ray diffraction (PXRD) data were recorded on a Rigaku SmartLab diffractometer by depositing powder on glass substrate. Thermogrametric analysis (TGA) traces were collected on a TA Instruments TGA/SDTA851e series thermal gravimetric analyzer with the sample held in a Al_2O_3 pan under N_2 atmosphere with the flow rate of 50 ml min^{-1}. Temperature was controlled by the furnace heating from 50°C up to 1000°C with a ramp rate of 5°C min^{-1}. High resolution transmission electron microscope (HR-TEM) images were obtained by Hitachi H-7100, Hitachi H-7650, JEOL JEM-2010 UHR and JEOL JEM-ARM200F TEM. Solid-state UV-Vis spectra were carried out on a JASCO V-780 UV-Visible/NIR spectrophotometer. X-ray photoelectron spectra (XPS) were recorded on an Shimadzu/Kratos X-ray AXIS-ULTRA DLD XPS spectrometer with Al K_α radiation as X-ray source for radiation. The binding energy values of all core-level spectra were referenced to the C 1s neutral-carbon peak at 284.8 eV. The XPS peaks were deconvoluted into different components after subtraction of the background using the Shirley method. Nitrogen sorption isotherms were measured at 77 K with a Bel Japan Inc. BELSORP-mini II and Micromeritics Instrument Corporation 3Flex surface characterization analyzer. Before measurement, the samples were degassed in vacuum at 120 °C for more than 10 h. The Brunauer-Emmett-Teller (BET) and Langmuir method were utilized to calculate the specific surface areas. By using the quenched solid state functional theory (QSDFT) slit/cylindr./sphere pore model, the pore size and volume was derived from the sorption curve. Micropore contribution was conducted from De Boer *t*-plot.

We performed Pawley refinement to optimize the lattice parameters iteratively until the R_{wp} value converges. The pseudo-Voigt profile function was used for whole profile fitting and Berrar–Baldinozzi function was used for asymmetry correction during the refinement

processes. The crystalline structures were determined using the density-functional tight-binding (DFTB+) method including Lennard-Jones (LJ) dispersion implemented in Materials Studio version 8.0 (Accelrys). [40] The Coulombic interaction between partial atomic charges was determined using the self-consistent charge formalism. Lennard-Jones-type dispersion was employed in all calculations to describe van der Waals and π-stacking interactions. The lattice dimensions were optimized simultaneously with the geometry. Standard DFTB parameters for X–Y element pair (X, Y = C, O, H, F and N) interactions were employed from the mio-0-1 set and halorg set.

4. Results and discussions

4.1 2D [4 + 4] COFs

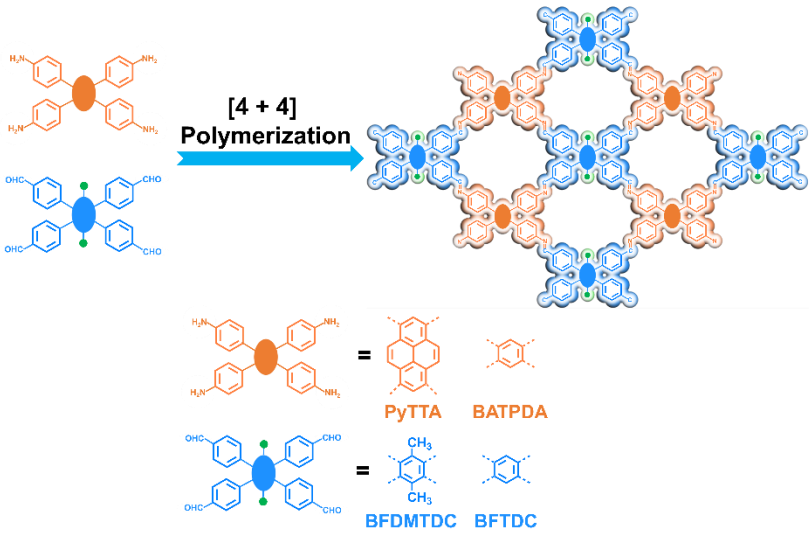

Figure 1. Schematics for the synthesis of 2D [4 + 4] COFs.

First, we synthesized 2D [4 + 4] COFs. **Figure 1** shows the typical synthesis route of 2D [4 + 4] COFs. In these 2D [4 + 4] COFs, knots (PyTTA and BATPDA) and linkers (BFTDC and BFDMTDC) both are tetrafunctional monomers with approximate angels of 60° and 120°. Due to the good geometric matching between knots and linkers, after reacting in the mixed organic solvent and aqueous acetic acid at 120 °C for 5 days, four-connected 2D COFs via [4 + 4] pathway were formed.

The formation of imine bonds in yellow 2D [4 + 4] COFs were confirmed by FT-IR spectroscopy and XPS. The FT-IR spectra showed a band of characteristic C=N stretching

modes at 1622 cm^{-1} (**Figure 2**). [41] The deconvoluted peak at 285.5 eV and 399.0 eV from the high-resolution XPS spectra of C 1s and N 1s are also contributed to imine bonds (**Figure 3**, **4**). [42] Moreover, the atom ratios determined by XPS and element analysis are close to the corresponding theoretical values further verifying the expected structures. And in the ^{13}C CPTOSS solid-state NMR spectra (**Figure 5**), signals at 151-156 ppm were assigned to characteristic C=N double bonds [43], while chemical shifts at 15.1 ppm and 16.0 ppm in PyTTA-BFDMTDC COF and BATPDA-BFDMTDC COF (**Figure 5B**, **D**) were attributed to methyl groups. [44]

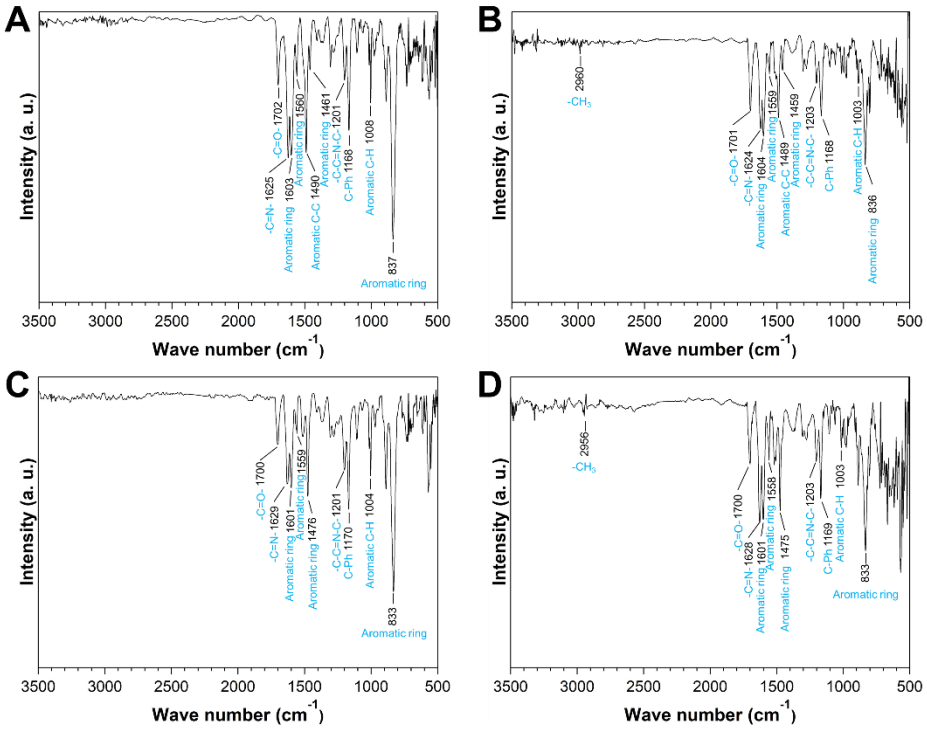

Figure 2. FT-IR spectra of (A) PyTTA-BFTDC COF, (B) PyTTA-BFDMTDC COF, (C) BATPDA-BFTDC COF and (D) BATPDA-BFDMTDC COF, respectively.

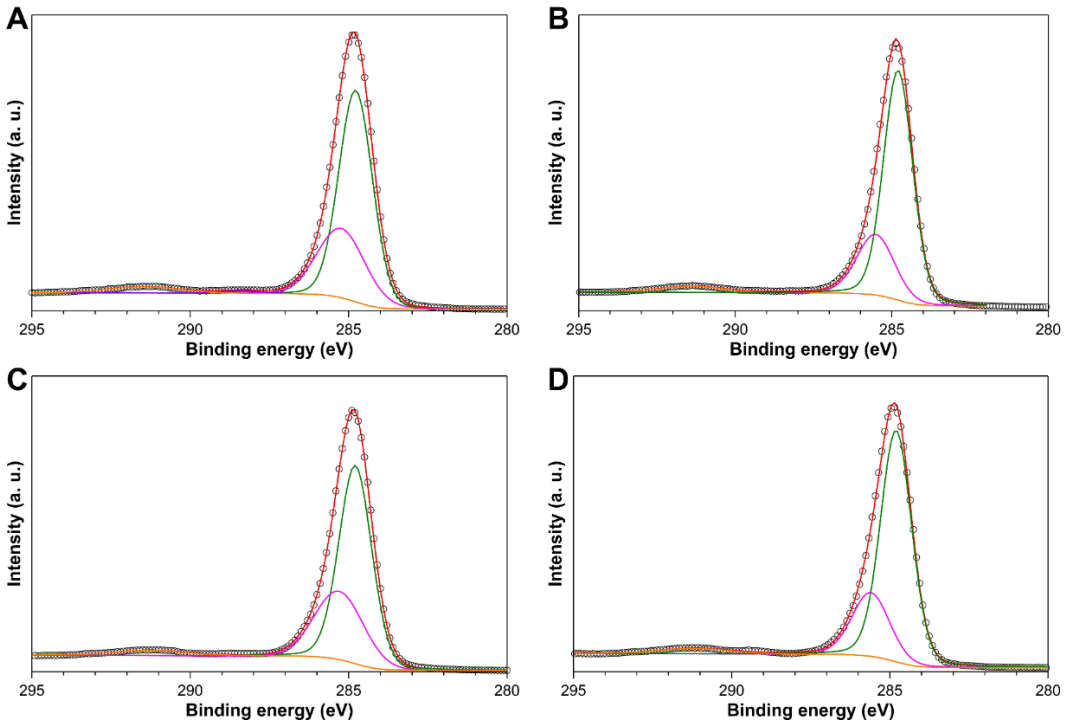

Figure 3. XPS spectra of C 1s for (A) PyTTA-BFTDC COF, (B) PyTTA-BFDMTDC COF, (C) BATPDA-BFTDC COF and (D) BATPDA-BFDMTDC COF, respectively.

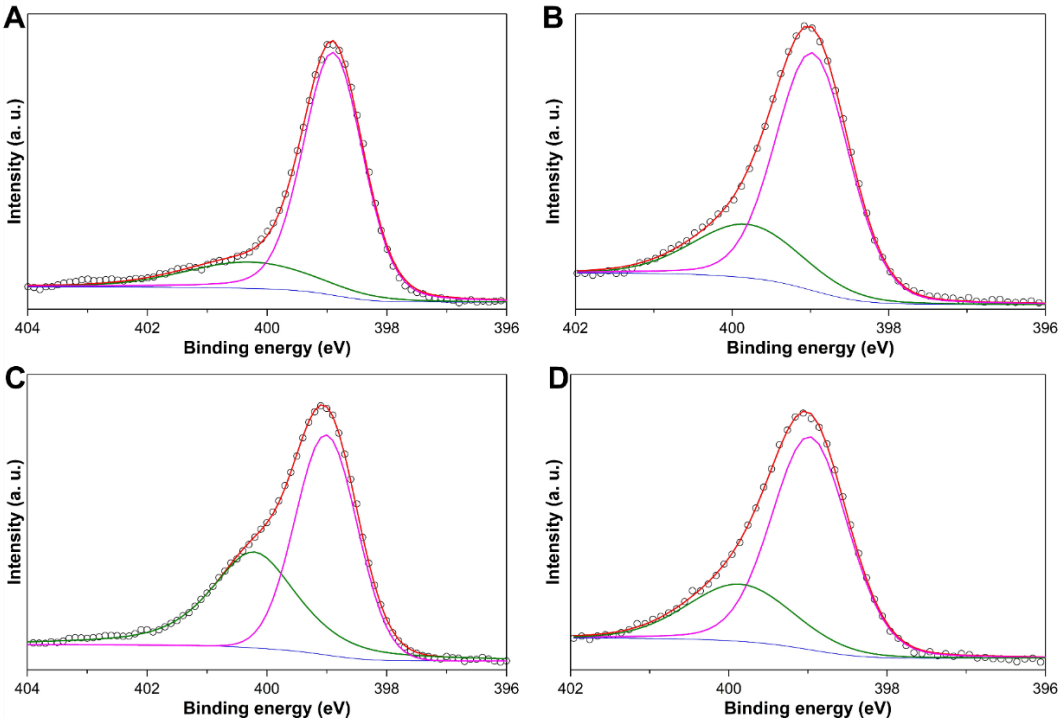

Figure 4. XPS spectra of N 1s for (A) PyTTA-BFTDC COF, (B) PyTTA-BFDMTDC COF, (C) BATPDA-BFTDC COF and (D) BATPDA-BFDMTDC COF, respectively.

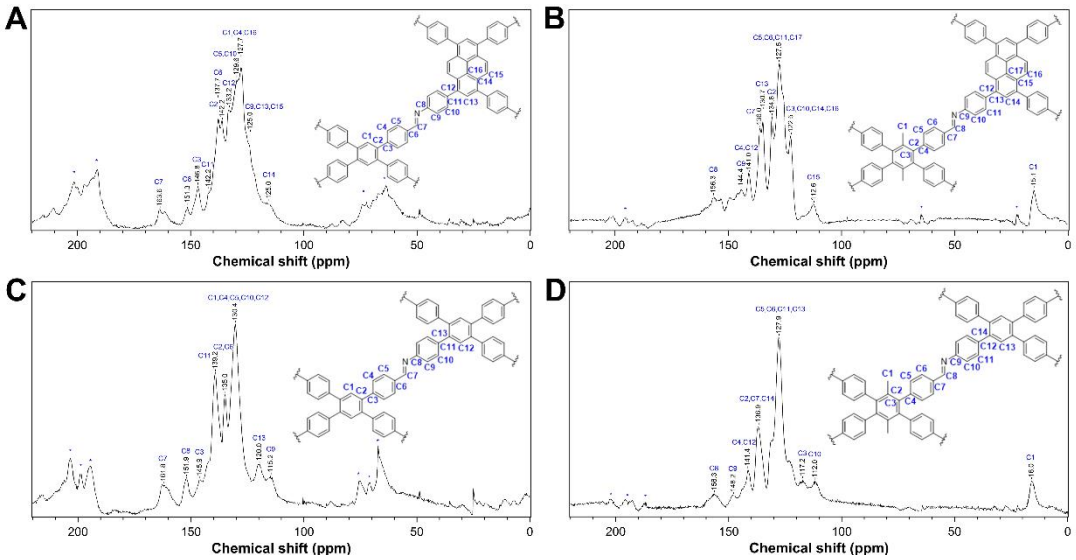

Figure 5. ^{13}C CPTOSS solid-state NMR spectra of (A) PyTTA-BFTDC COF, (B) PyTTA-BFDMTDC COF, (C) BATPDA-BFTDC COF and (D) BATPDA-BFDMTDC COF, respectively.

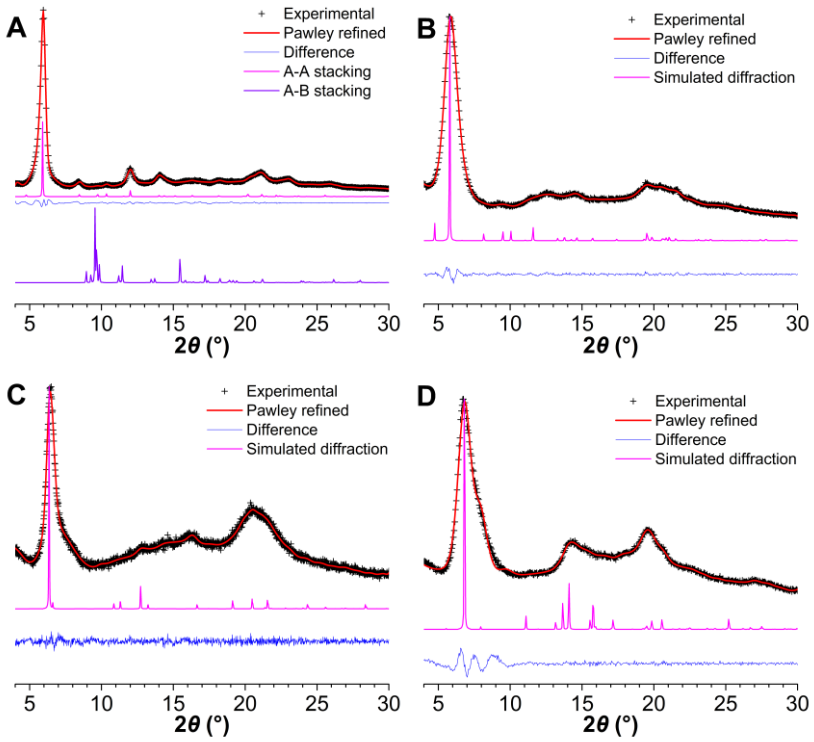

Figure 6. Experimental, Pawley-refined, predicted PXRD patterns of eclipsed and staggered structures, difference, and background plots of (A) PyTTA-BFTDC COF (R_{wp}:3.27%, R_p:2.44%), (B) PyTTA-BFDMTDC COF (R_{wp}:1.90%, R_p:1.55%), (C) BATPDA-BFTDC COF (R_{wp}:3.59%, R_p:2.83%) and (D) BATPDA-BFDMTDC COF (R_{wp}:3.20%, R_p:2.30%), respectively.

The PXRD patterns of 2D [4 + 4] COFs were presented in **Figure 6**. All 2D [4 + 4] COFs exhibited strong diffraction peaks at around 6°, indicating they perhaps have similar

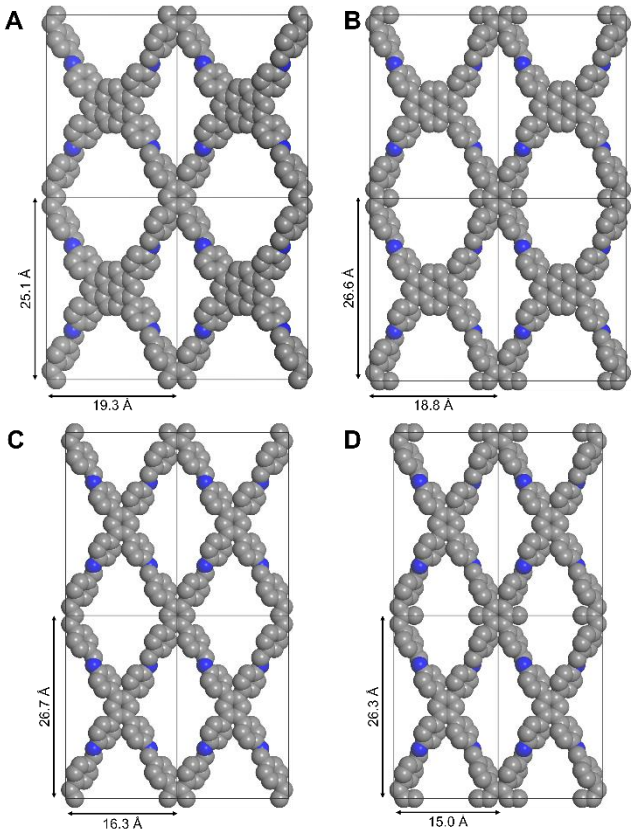

Figure 7. Crystalline lattices (H is omitted for clarity) of (A) PyTTA-BFTDC COF (Symmetry: P2/M, a=19.3 Å, b=25.1 Å, c=4.5 Å, α=γ=90°, β=111.2°), (B) PyTTA-BFDMTDC COF (Symmetry: P2/M, a=18.8 Å, b=26.6 Å, c=4.6 Å, α=γ=90°, β=96.1°), (C) BATPDA-BFTDC COF (Symmetry: P2/M, a=16.3 Å, b=26.7 Å, c=4.3 Å, α=γ=90°, β=89.1°) and (D) BATPDA-BFDMTDC COF (Symmetry: P2/M, a=15.0 Å, b=26.3 Å, c=5.3 Å, α=γ=90°, β=91.5°), respectively.

topologies. Based on space group: P2/M, the A-A stacking structures of 2D [4 + 4] COFs were built and optimized by MS 8.0 (**Figure 7**). In **Figure 6A**, the Pawley refined PXRD pattern of PyTTA-BFTDC COF with very low R_{wp} and R_p values of 3.24% and 2.44% was in good agreement with the experimental result, where PXRD peaks at 5.9°, 8.4°, 12.0° and 14.0° were corresponding to (110), (120), (220) and (040), respectively. The (001) peak of PyTTA-BFTDC COF at 21.1° indicated the π-π stacking distance is 4.2 Å, while the (001) peak of PyTTA-BFDMTDC COF in **Figure 6B** at 19.5° suggested the interlayer space of PyTTA-BFDMTDC COF increased owing to the introducing of methyl groups. By contrast, BATPDA-BFTDC COF demonstrated a smaller lattice size (**Figure 7C**) (a=16.3 Å, b=26.7 Å, c=4.3 Å, α=γ=90°, β=89.1°) than that of PyTTA-BFTDC COF (**Figure 7A**) (a=19.3 Å, b=25.119.3 Å, c=4.5 Å, α=γ=90°, β=111.2°) because of the smaller molecular size of BATPDA than that of PyTTA.

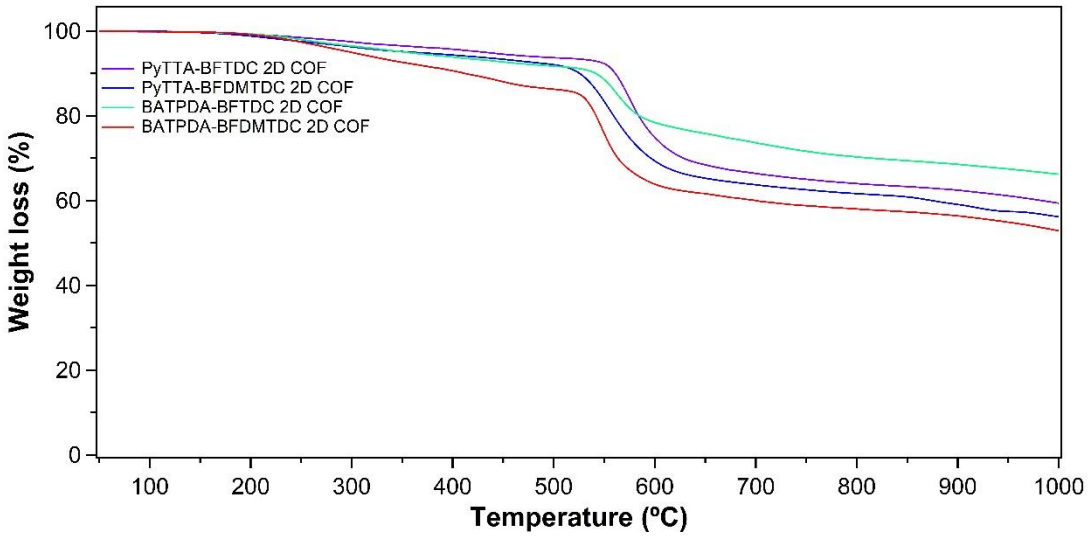

Figure 8. TGA traces for 2D [4 + 4] COFs.

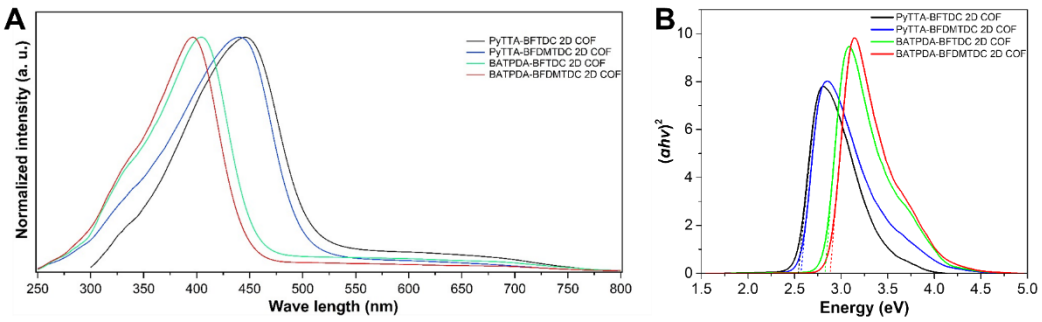

Figure 9. (A) Solid-state UV-vis spectra and (B) Tauc plots for 2D [4 + 4] COFs.

Besides high crystallinities, 2D [4 + 4] COFs possess good thermal stabilities assessed by TGA under N_2. As revealed by the TGA traces (**Figure 8**), 2D [4 + 4] COFs remained stable before around 550 °C. Solid state UV-vis spectra (**Figure 9**) revealed that all [4 + 4] COFs absorb light in the ultraviolet and violet parts, suggesting the optical band gaps of 2.53–2.88 eV as determined by the Kubelka-Munk function and Tauc plots (**Figure 9B**). Compared with PyTTA-BFTDC COF and PyTTA-BFDMTDC, the blue shifted bands of BATPDA-BFTDC COF and BATPDA-BFDMTDC COF by around 50 nm can be ascribed to their lower degree of conjugation. A small blue shift after decorating by methyl groups results from the effect of methyl group on delocalization along as well as across the plane in the extended frameworks.

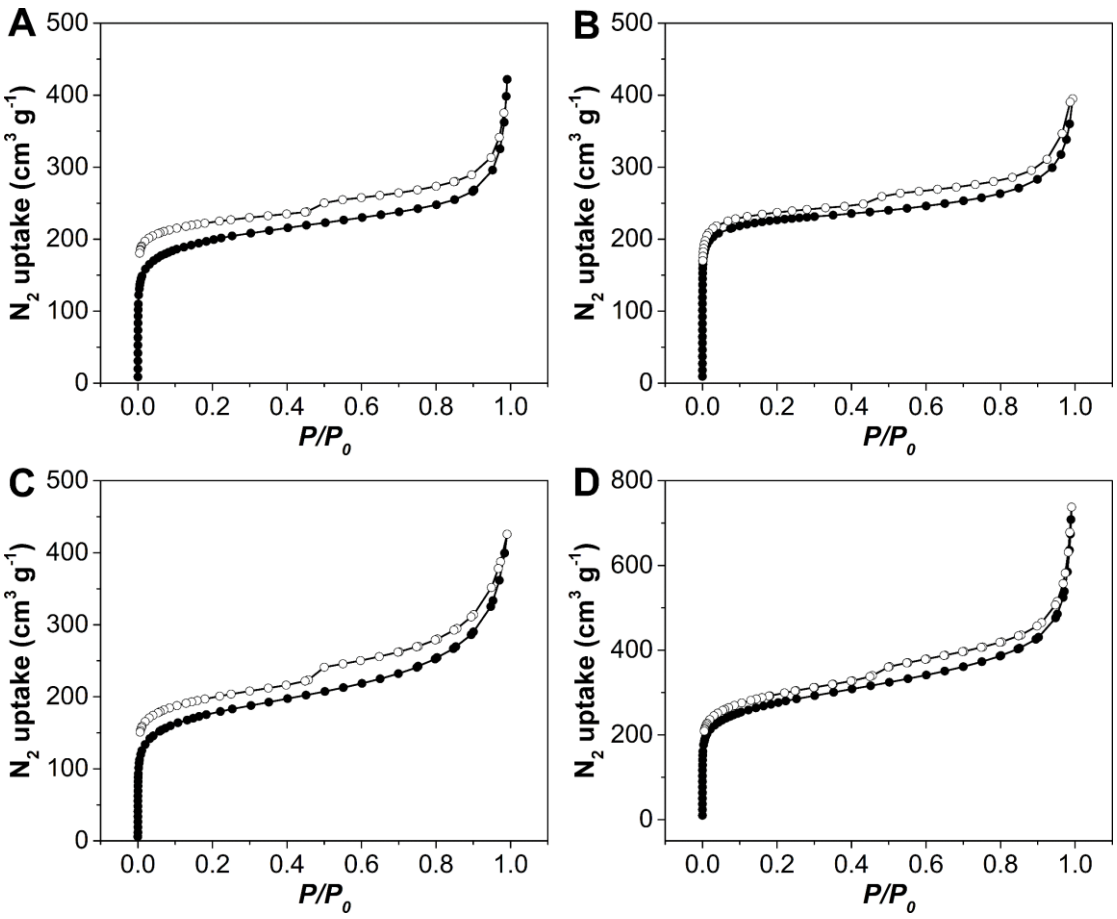

Figure 10. N_2 sorption isotherms measured at 77 K for (A) PyTTA-BFTDC COF, (B) PyTTA-BFDMTDC COF, (C) BATPDA-BFTDC COF and (D) BATPDA-BFDMTDC COF, respectively.

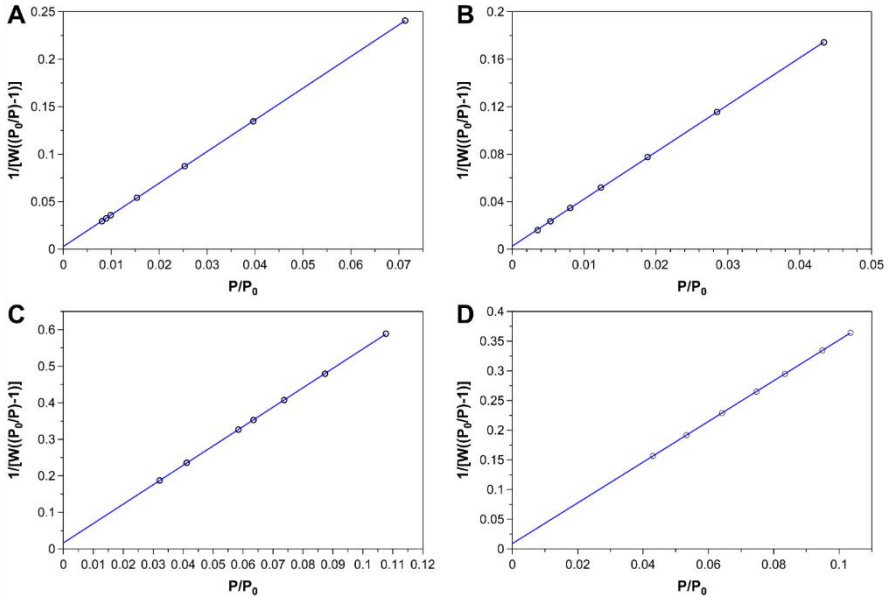

Figure 11. BET plot calculated from N_2 adsorption data for (A) PyTTA-BFTDC COF, (B) PyTTA-BFDMTDC COF, (C) BATPDA-BFTDC COF and (D) BATPDA-BFDMTDC COF, respectively.

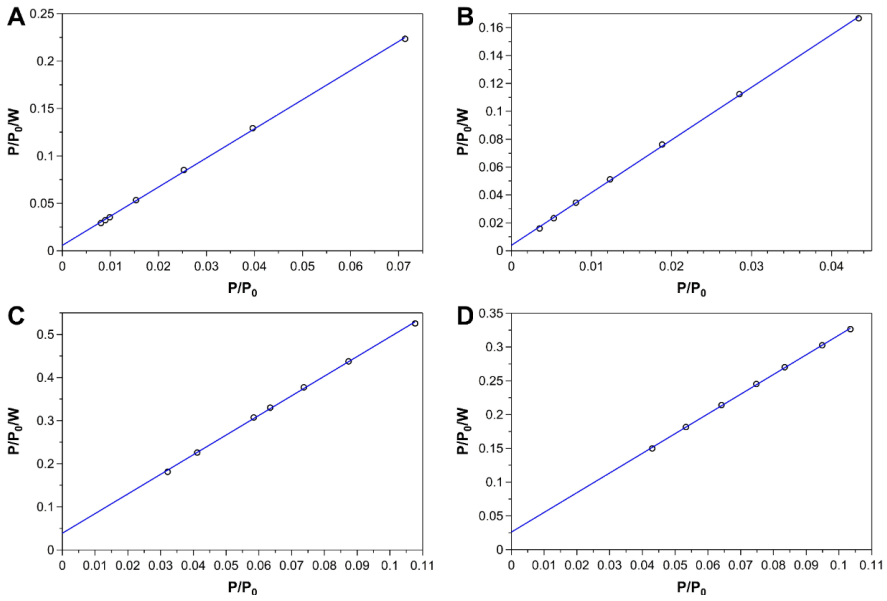

Figure 12. Langmuir plot calculated from N_2 adsorption data for (A) PyTTA-BFTDC COF, (B) PyTTA-BFDMTDC COF, (C) BATPDA-BFTDC COF and (D) BATPDA-BFDMTDC COF, respectively.

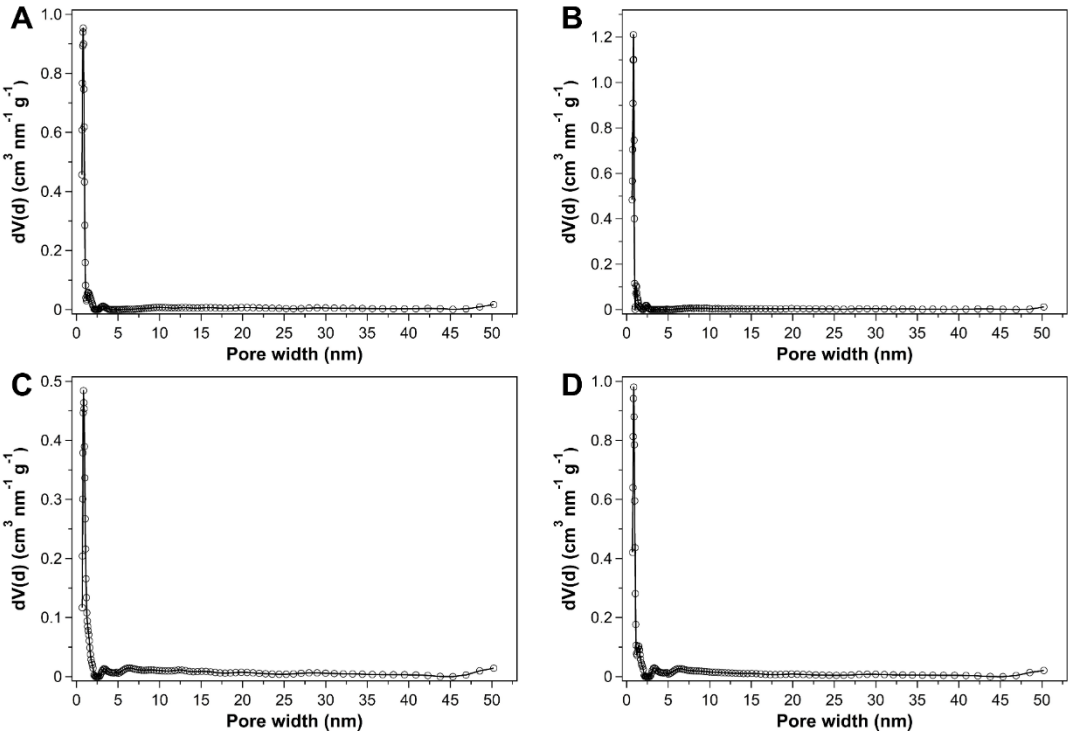

Figure 13. Pore size distributions calculated after fitting QSDFT (slit/cylindr./sphere) models to adsorption data for (A) PyTTA-BFTDC COF, (B) PyTTA-BFDMTDC COF, (C) BATPDA-BFTDC COF and (D) BATPDA-BFDMTDC COF, respectively.

The porosities of 2D [4 + 4] COFs were evaluated by N_2 sorption isotherm (**Figure 10**), which showed very sharp uptakes at low pressure, suggesting they possess rich micropores. [45] The BET and Langmuir surface areas of PyTTA-BFDMTDC COF (878 and

922 $m^2 g^{-1}$, **Figure 11B**, **12B**) and BATPDA-BFDMTDC COF (1013 and 1194 $m^2 g^{-1}$, **Figure 11D**, **12D**) were larger than those of PyTTA-BFTDC COF (741 and 850 $m^2 g^{-1}$, **Figure 11A**, **12A**) and BATPDA-BFTDC COF (654 and 764 $m^2 g^{-1}$, **Figure 11C**, **12C**), respectively. This indicated methyl groups are beneficial to increase the porosity of 2D [4 + 4] COFs. [46] Moreover, all 2D [4 + 4] COFs had narrow pore size distributions at 0.85 nm along with a small fraction of mesopores calculated by using the QSDFT method (**Figure 13**), demonstrating the introducing of methyl groups did not affect the pore size to a great extent. Their high crystallinities and porosities were further confirmed by HR-TEM and fast Fourier transform (FFT) (**Figure 14**). Fringe spacings of ~1.1-1.4 nm (fitting d_{110} for 2D COFs) were measured by FFT (inset).

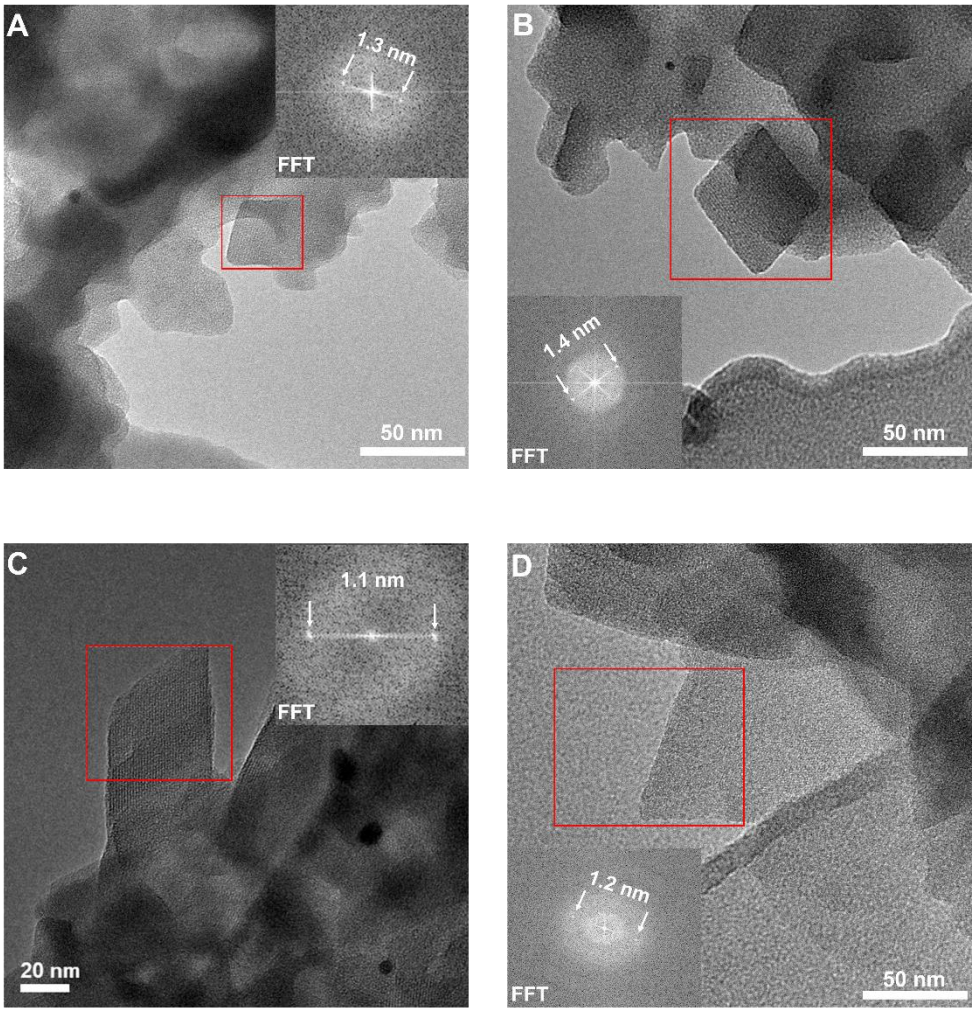

Figure 14. HR-TEM image of (A) PyTTA-BFTDC COF, (B) PyTTA-BFDMTDC COF, (C) BATPDA-BFTDC COF and (D) BATPDA-BFDMTDC COF, respectively. Inset: FFT of the image, cropped at the predominant fringe spacing of d_{110}.

4.2 1D COFs

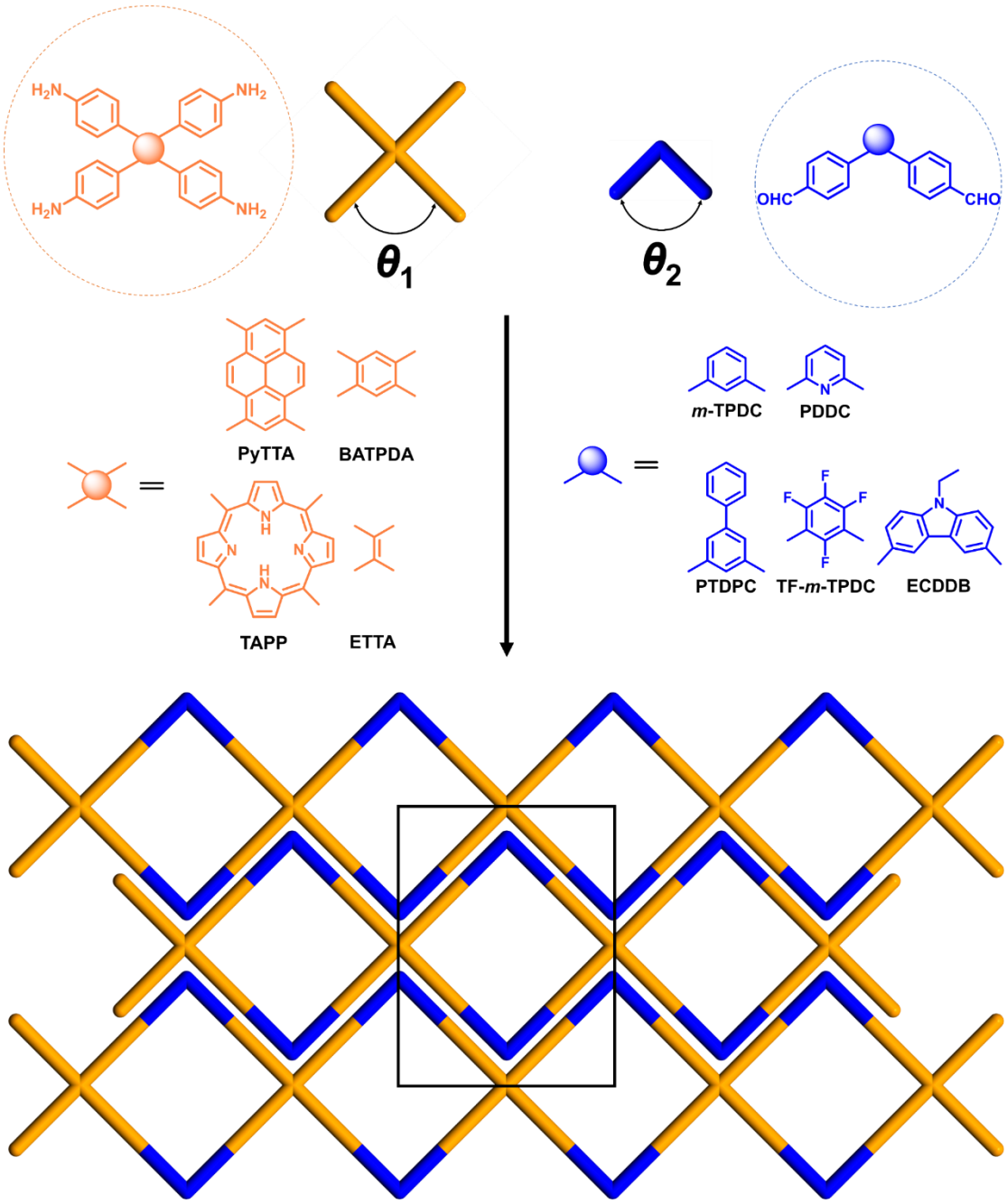

Figure 15. A general designing strategy of 1D COFs. Illustrations of the building of 1D COFs zigzag packed by 1D porous chains where angles of brown shape (tetrahedral knots: PyTTA, BATPDA, TAPP and ETTA) are θ_1 and π-θ_1, while blue shape (V-type linkers: *m*-TPDC, PDDC, PTPDC, TF-*m*-TPDC and ECDDB) have an angle of θ_2.

Next, 1D COFs are designed and synthesized according to the strategy as shown in **Figure 15**. In order to construct the unusual 1D COF, we synthesized a series of aldehyde functionalized monomers (*m*-TPDC, its derivatives, and ECDDB) as linkers with novel geometries. They were designed bearing two phenyl aldehyde groups in the meta positions

of phenyl or phenyl substituents. The position of the aldehyde groups in these linkers approximates a V-type shape (θ_2=90~120°) and can be used to bridge tetrahedral amine knots PyTTA, BATPDA, ETTA or TAPP via imine bonds. The good geometrical matching between these V-type linkers and knots, where the angles (θ_1) are equal approximately to either ~90° or ~60° and ~120°, generates supermicropores on the 1D chain. Interaction such as π-π interaction between these 1D chains likely facilitates close packing of 1D chains into 1D COFs.[47] We believe this new type of 1D COFs will open a new perspective and has great potential to extend the range of structures and properties in the field of COFs.

We synthesized 1D COFs via imine condensation reactions by combining a mixture of tetrahedral knots and V-type linkers in the mixed organic solvent and aqueous acetic acid. The reaction mixture was sealed in a Pyrex tube and heated at 120 °C for 5 days. The resulting precipitate was collected by filtration, washed with THF, and then evacuated at 100 °C for 6 hours to yield a solid, which was insoluble in common polar and nonpolar organic solvents even though refluxed DMSO.

***m*-TPDC and PyTTA**

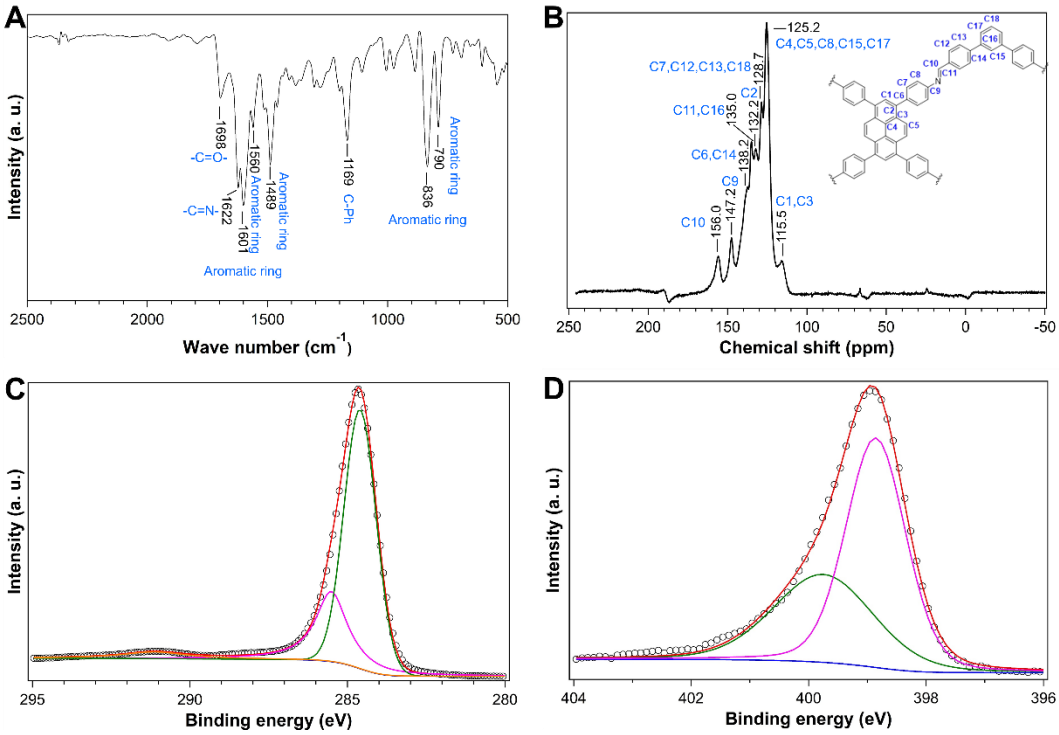

Figure 16. PyTTA-*m*-TPDC COF. (A) FTIR spectrum; (B) Solid-state NMR spectrum; High-resolution XPS spectrum of (C) C 1s and (D) N 1s.

Firstly, taking PyTTA-*m*-TPDC 1D COF as a typical example, imine bonds in 1D COFs were confirmed by FT-IR spectroscopy, solid-state NMR spectroscopy and XPS. The peak at 1622 cm^{-1} in FT-IR spectrum (**Figure 16A)**, chemical shift at 156 ppm in CPTOSS solid-state NMR spectrum (**Figure 16B**) and deconvoluted peaks at 285.5 eV and 399.0 eV in high-resolution XPS spectrum of C 1s and N 1s (**Figure 16C** and **D**) are also contributed to imine bonds. [42,44,48,49] Moreover, the atom ratio determined by XPS and element analysis further verified the theoretical chemical composition.

From a topological point of view, besides 1D structures, there are another two possible crystal lattices for 1D COFs. Taking PyTTA-*m*-TPDC 1D COF as a typical example, **Figure 17A-C** showed three different possible structures. As shown in **Figure 17D**, although the total energy of monoclinic structure is higher than that of orthorhombic structure, the valence energy is lower. This suggests the topological layers in monoclinic structure is the most thermodynamically stable. Moreover, notably the experimental PXRD pattern of the

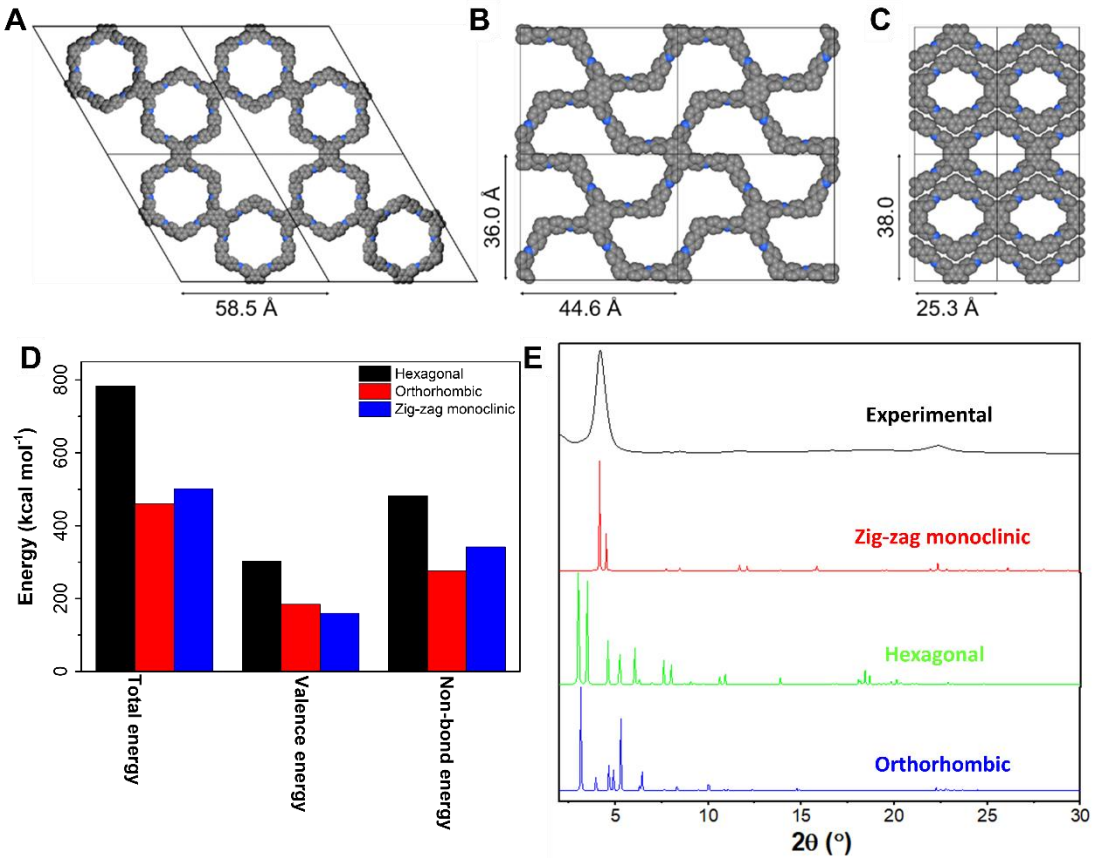

Figure 17. Three different possible structure of PyTTA-*m*-TPDC COF. (A) Experimental and predicted PXRD pattern; (B) Hexagonal eclipsed structure. (C) Orthorhombic eclipsed structure. (D) Monoclinic zig-zag eclipsed structure.

zig-zag structure only exclusively reproduced the simulated PXRD pattern of the eclipsed structure as shown in **Figure 17E**, strongly suggesting that the as-prepared COF holds 1D structure with single aperture.

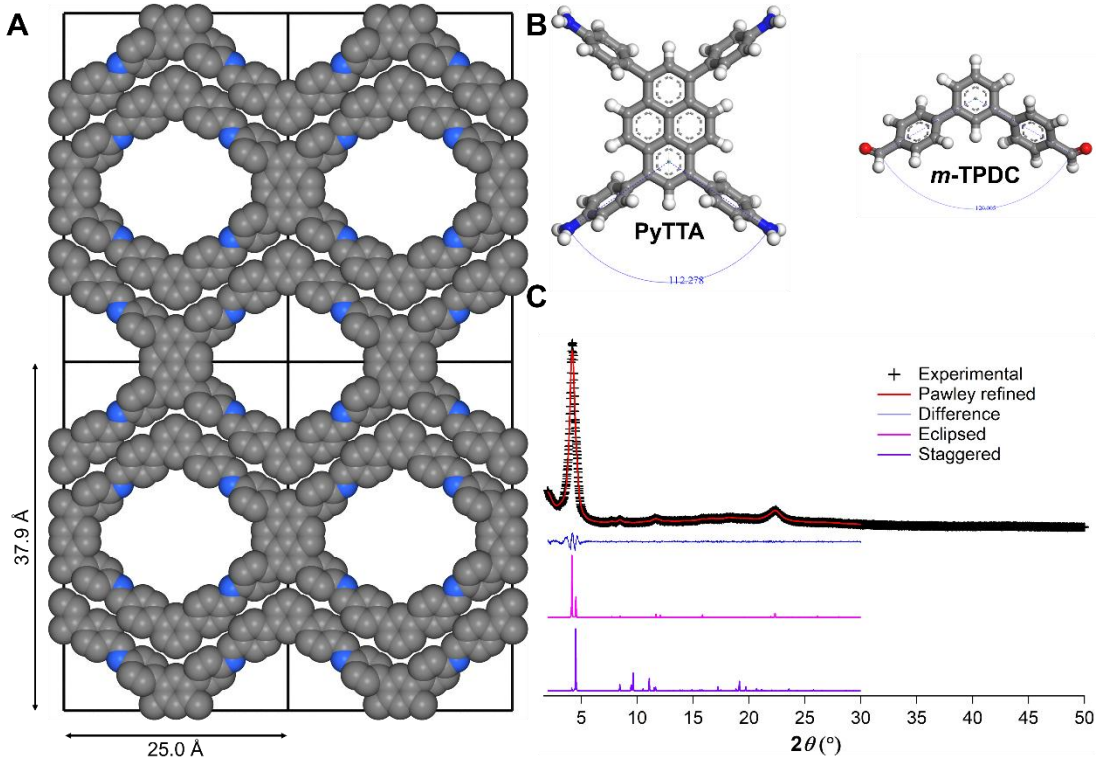

Figure 18. Structure of PyTTA-*m*-TPDC 1D COF. (A) The eclipsed structure (H is omitted for clarity); (B) Structures of the knot (PyTTA) and linker (*m*-TPDC); (C) The Pawley refinement (R_{wp}:3.72%, R_p:2.82%).

In PyTTA-*m*-TPDC 1D COF, the angles of knot and linker both are about 120 °. The eclipsed stacking model (**Figure 18A**) with C2/M symmetry of PyTTA-*m*-TPDC 1D COF was built by MS 8.0 and geometrically optimized by DFTB+ method including L-J dispersion. The Pawley refined PXRD pattern (**Figure 18C**) with very low R_{wp} and R_p values of 3.72% and 2.82% is in good agreement with the experimental result. PyTTA-*m*-TPDC 1D COF with an eclipsed structure (a=25.0Å, b=37.9 Å, c=4.2 Å, α=γ=90º, β=106.4º) exhibited a set of strong PXRD peaks at 4.3º, 7.7º, 8.5º, 11.6º and 15.8º, corresponding to (110), (130), (220), (240) and (350) respectively. The (001) peak at 22.3º indicates the π-π stacking distance is 4.0 Å.

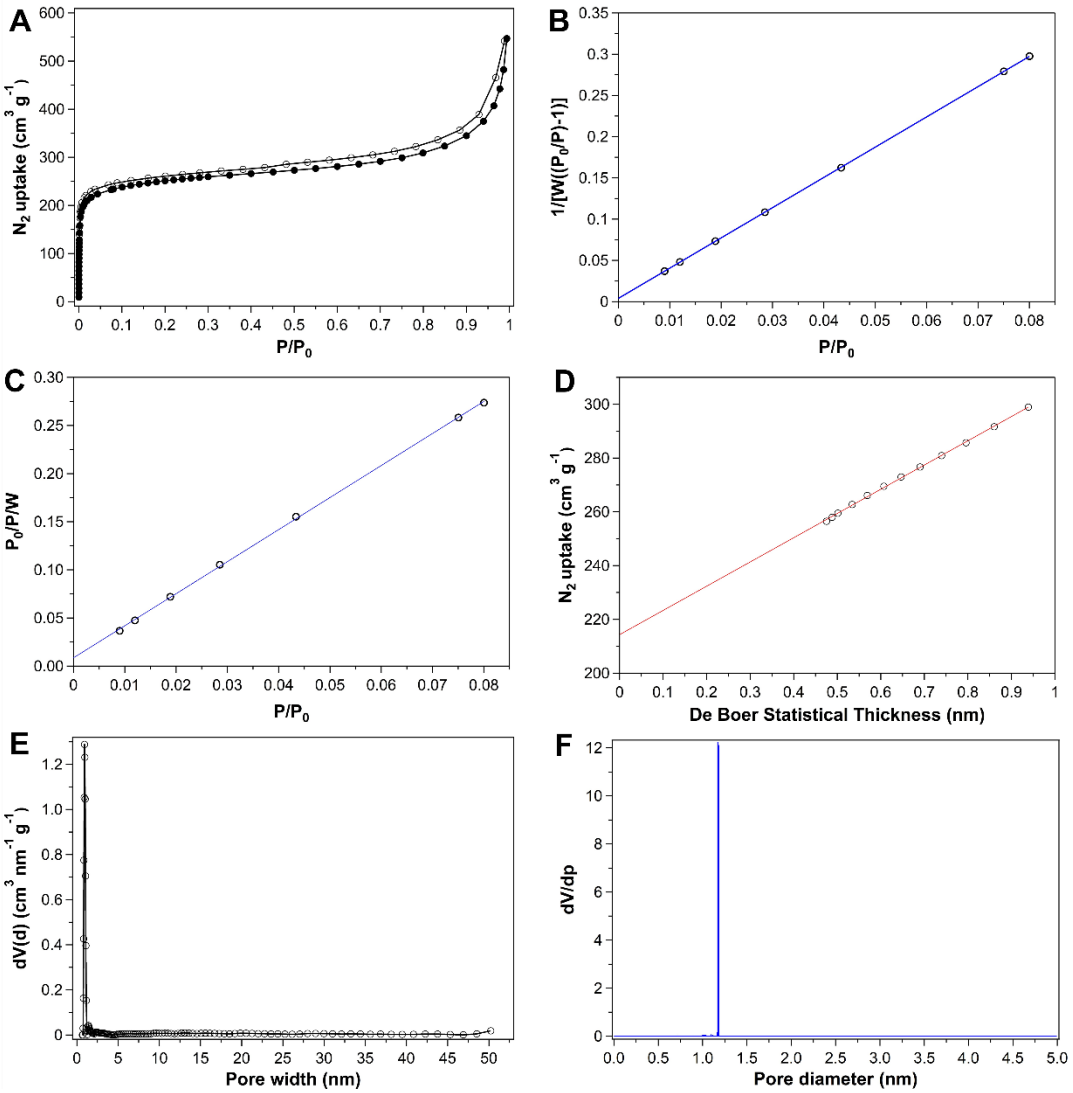

Figure 19. Porosity of PyTTA-*m*-TPDC 1D COF. (A) N_2 isotherm; (B) BET plot; (C) Langmuir plot; (D) De Boer *t*-plot; (E) Pore size distribution calculated after fitting QSDFT (slit/cylindr./sphere) models to adsorption data; (F) The simulated pore size distribution result by Poreblazer.

The porosity of PyTTA-*m*-TPDC 1D COF was evaluated by N_2 adsorption isotherm (**Figure 19A**), which showed a very sharp uptake at P/P_0 from 10^{-5} to 10^{-1}, a signature feature of a microporous material.[45] The BET surface area (**Figure 19B**), Langmuir surface area (**Figure 19C**), and pore volume of PyTTA-*m*-TPDC 1D COF were estimated to be 949 $m^2\ g^{-1}$, 1046 $m^2\ g^{-1}$ and 0.59 $cm^3\ g^{-1}$. Among that, the contribution of micropores was 809 $m^2\ g^{-1}$ (85%) calculated from *t*-plot (**Figure 19D**).[50] More important, the calculated pore size distribution by using the QSDFT method was 0.93 nm (**Figure 19E**), which is much

coincided with the simulated one (1.2 nm) of eclipsed model by Poreblazer (**Figure 19F**), confirming the 1D structure again.

***m*-TPDC and other knots**

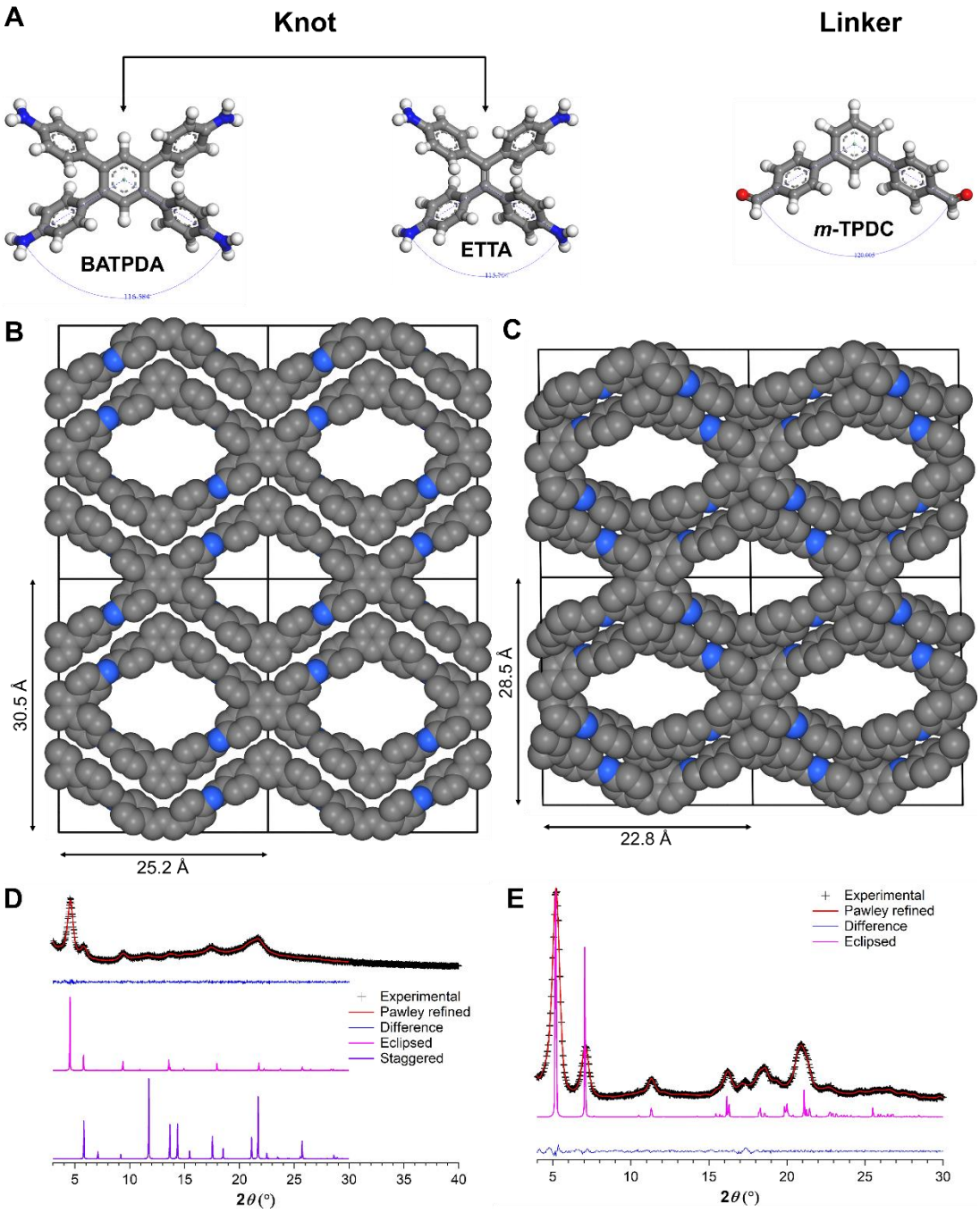

Figure 20. (A) Structures of BATPDA, ETTA and *m*-TPDC; The eclipsed structure (H is omitted for clarity) of (B) BATPDA-*m*-TPDC 1D COF and (C) ETTA-*m*-TPDC 1D COF; The Pawley refinement of (D) BATPDA-*m*-TPDC 1D COF (R_{wp}:3.92%, R_p:3.09%) and (E) ETTA-*m*-TPDC 1D COF (R_{wp}:2.58%, R_p:2.00%).

The angles of other knots ETTA and BATPDA (**Figure 20A**) are same as that of PyTTA, resulting in similar geometry, so they can also produce 1D COFs (ETTA-*m*-TPDC 1D COF and BATPDA-*m*-TPDC 1D COF, **Figure 20B**, **C**) with the linker-*m*-TPDC. Low Pawley refinement errors (**Figure 20D**, **E**) indicate a near equivalence between calculated and refined cell parameters that ensure asserted 1D COF structures through modeling are indeed. Consistent with the pore size of PyTTA-*m*-TPDC 1D COF, ~1 nm aperture (**Figure 21C**, **D**) can be obtained for ETTA-*m*-TPDC 1D COF and BATPDA-*m*-TPDC 1D COF, while lower BET surface area (717 $m^2\ g^{-1}$ and 325 $m^2\ g^{-1}$) calculated from N_2 isotherms (**Figure 21A**, **B**) might be caused by the relatively poor conjugation of ETTA and BATPDA compared with PyTTA. [51]

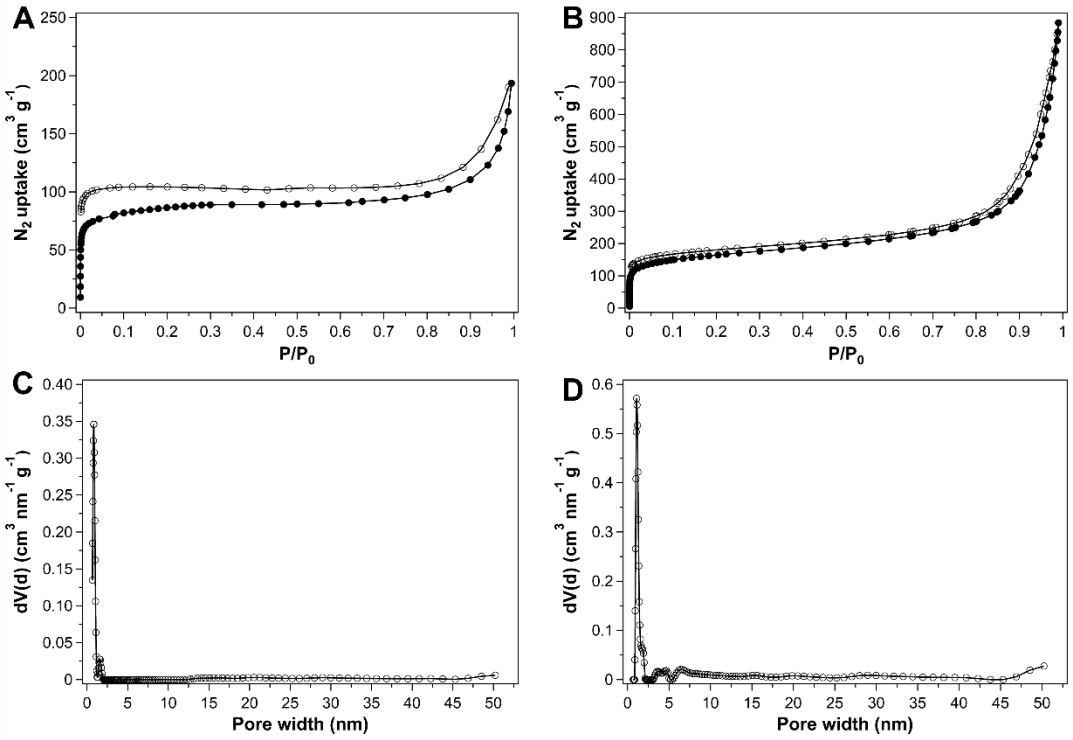

Figure 21. N_2 isotherms of (A) BATPDA-*m*-TPDC 1D COF and (B) ETTA-*m*-TPDC 1D COF; Pore size distribution calculated after fitting QSDFT (slit/cylindr./sphere) models to adsorption data for (C) BATPDA-*m*-TPDC 1D COF and (D) ETTA-*m*-TPDC 1D COF.

Functionalization

Functionalization with desirable atoms and groups is a powerful strategy for pore engineering of COFs. [52] Same as other COFs, introducing heteroatoms or aromatic groups into either pore surface or skeleton is also applicable to modify 1D COFs. Linkers—*m*-TPDC derivatives (**Figure 22A**) (PDDC (N replacing C), TF-*m*-TPDC (F replacing H), and

PTPDC (phenyl replacing H)), whose angle all are 120°, can give modified 1D COFs (PyTTA-PDDC 1D COF, PyTTA-TF-*m*-TPDC 1D COF, and PyTTA-PTPDC 1D COF) (**Figure 22B-D**) possessing high BET surface areas (729 m^2 g^{-1}, 1225 m^2 g^{-1}, and 859 m^2 g^{-1}) calculated from N_2 isotherms (**Figure 23A**, **23B** and **24A**). Among these, PyTTA-TF-*m*-TPDC 1D COF has a highest Langmuir surface area (**Figure 24B**) of 1346 m^2 g^{-1} calculated from N_2 isotherms (**Figure 24A**), which corresponds to a microspore (**Figure 24C**, 1115 m^2 g^{-1}, 91% contribution) volume of 0.64 cm^3 g^{-1}. Meanwhile, the calculated pore size distribution of these three 1D COFs was about 1 nm (**Figure 23C**, **23D** and **Table 1**). The obviously sharp PXRD peaks indicate the good crystallinity of these 1D COFs (**Figure 22E-G**).

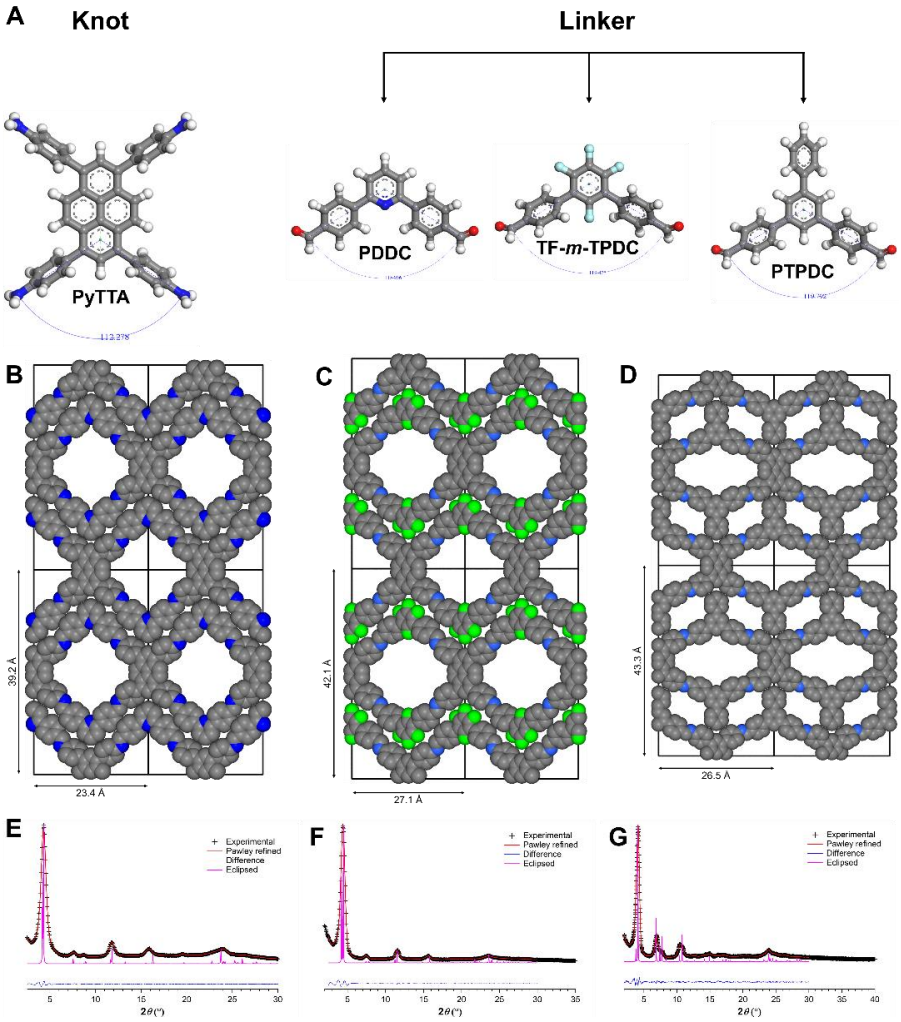

Figure 22. (A) Structures of PyTTA, PDDC, TF-*m*-TPDC and PTPDC; The eclipsed structure (H is omitted for clarity) of (B) PyTTA-PDDC 1D COF, (C) PyTTA-TF-*m*-TPDC 1D COF, and (D) PyTTA-PTPDC 1D COF; The Pawley refinement of (E) PyTTA-PDDC

1D COF (R_{wp}:2.15%, R_p:1.73%), (F) PyTTA-TF-*m*-TPDC 1D COF (R_{wp}:3.56%, R_p:2.69%), and (G) PyTTA-PTPDC 1D COF (R_{wp}:5.54%, R_p:3.41%).

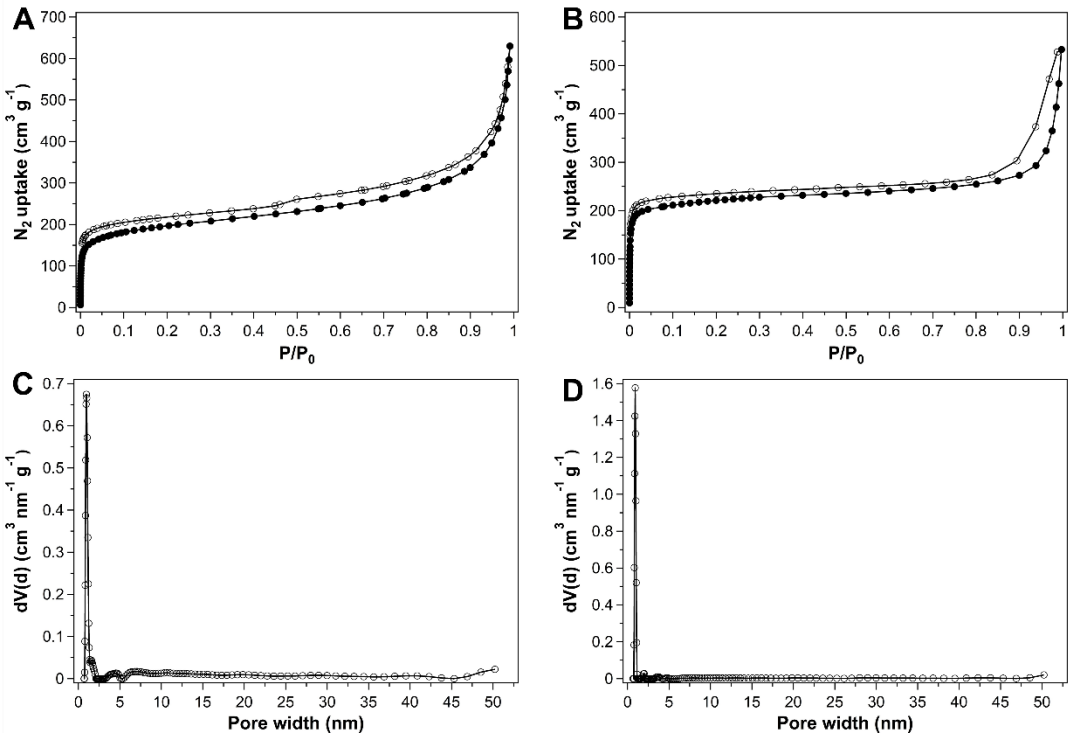

Figure 23. N_2 isotherms of (A) PyTTA-PDDC 1D COF and (B) PyTTA-PTPDC 1D COF; Pore size distribution calculated after fitting QSDFT (slit/cylindr./sphere) models to adsorption data for (C) PyTTA-PDDC 1D COF and (D) PyTTA-PTPDC 1D COF.

The optical band gap of the PyTTA-TF-*m*-TPDC 1D COF determined by solid-state UV-vis spectrum was 2.24 eV (**Figure 24D**), further proving the high crystallinity and low defect within the linear COFs. The architectural stability of the PyTTA-TF-*m*-TPDC 1D COF was evaluated by TGA, which showed a main weight loss at 550 °C where the frameworks start to decompose (**Figure 24E**). Even it remained its crystallinity under harsh conditions such as strong base (pH=13) and acid (pH=1) after one day (**Figure 24F**).

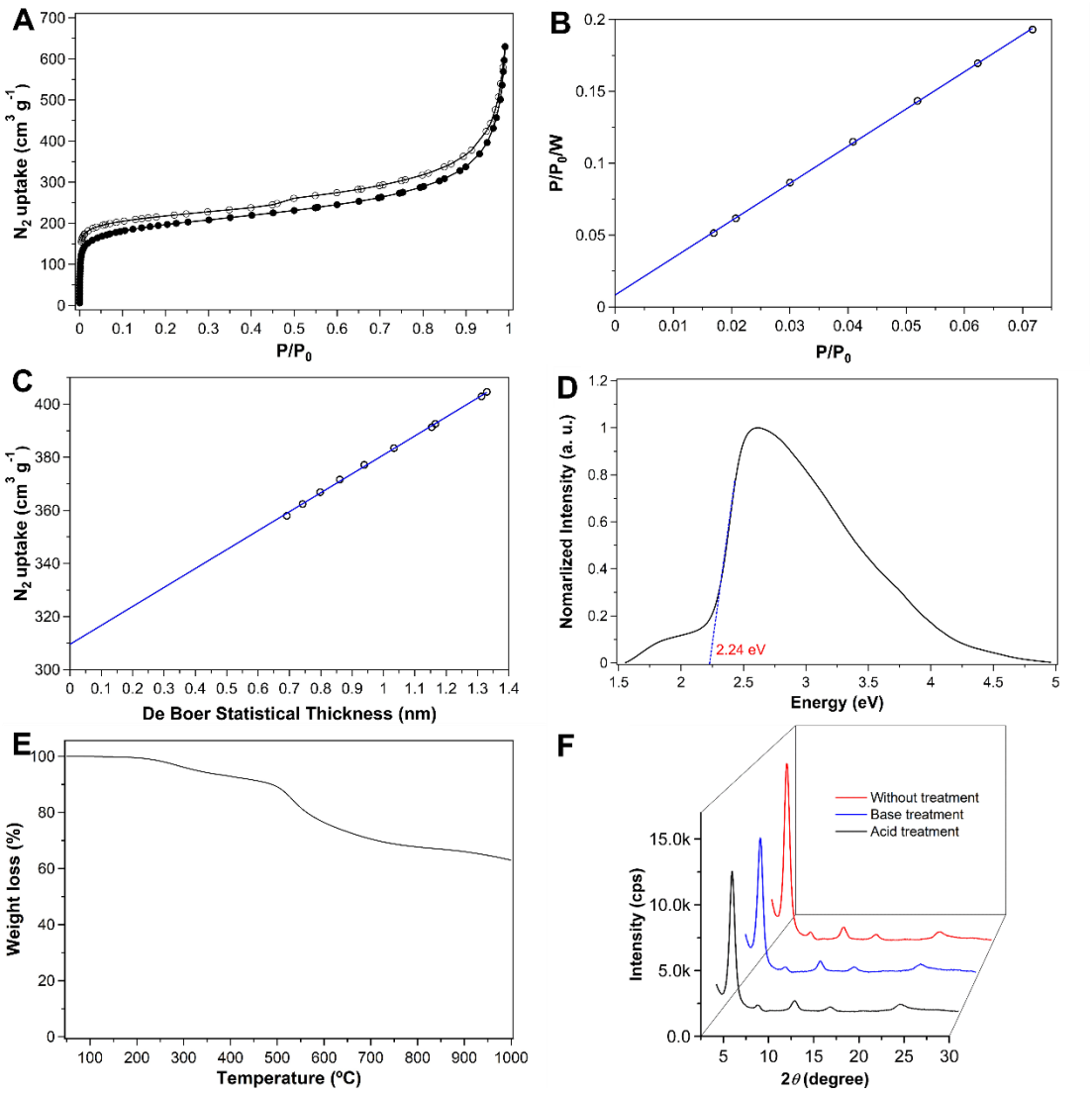

Figure 24. PyTTA-TF-*m*-TPDC 1D COF. (A) N_2 isotherms; (B) Langmuir plot; (C) *t*-plot; (D) UV-vis spectrum; (E) TGA trace; (F) The PXRD patterns comparison after treatment of strong acid (pH=1) and base (pH=13) for 24 h.

Mechanism

In general, *m*-TPDC and its derivatives all have an angle of ~120º so that it is favorable for them to match geometrically with PyTTA having a same angle of ~120º, without large torsional twists between the planes of the rings. However, as shown in **Figure 25**, TMS-*m*-TPDC (TMS replacing H) has too large steric hindrances to result in frameworks due to the reduced conjugation of likers and interlayered interaction. That suggests the conjugation of replaced groups plays an important role on the formation of these *m*-TPDC based 1D COFs. On the other hand, even though isophthalaldehyde also has an angle of ~120º (two

aldehyde groups are in the meta positions of phenyl), it is hardly to synthesize 1D COF likely due to more defects attributed to the shorter distance between two aldehyde groups.

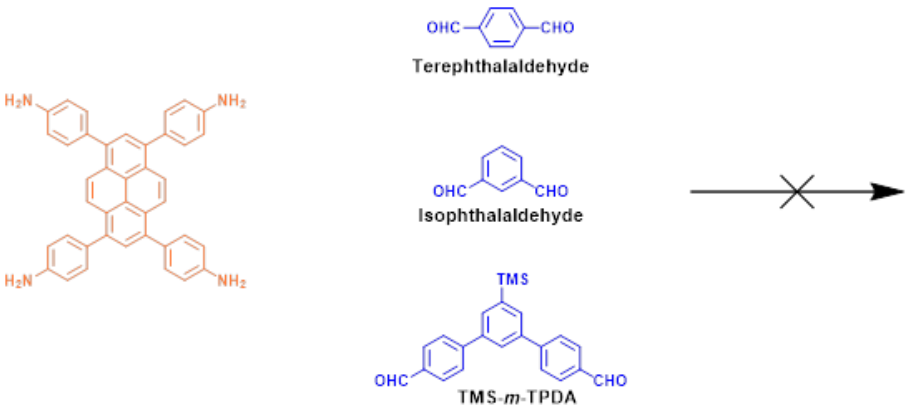

Figure 25. The failed reactions for formation of COFs.

Knots and linkers with angles of ~90°

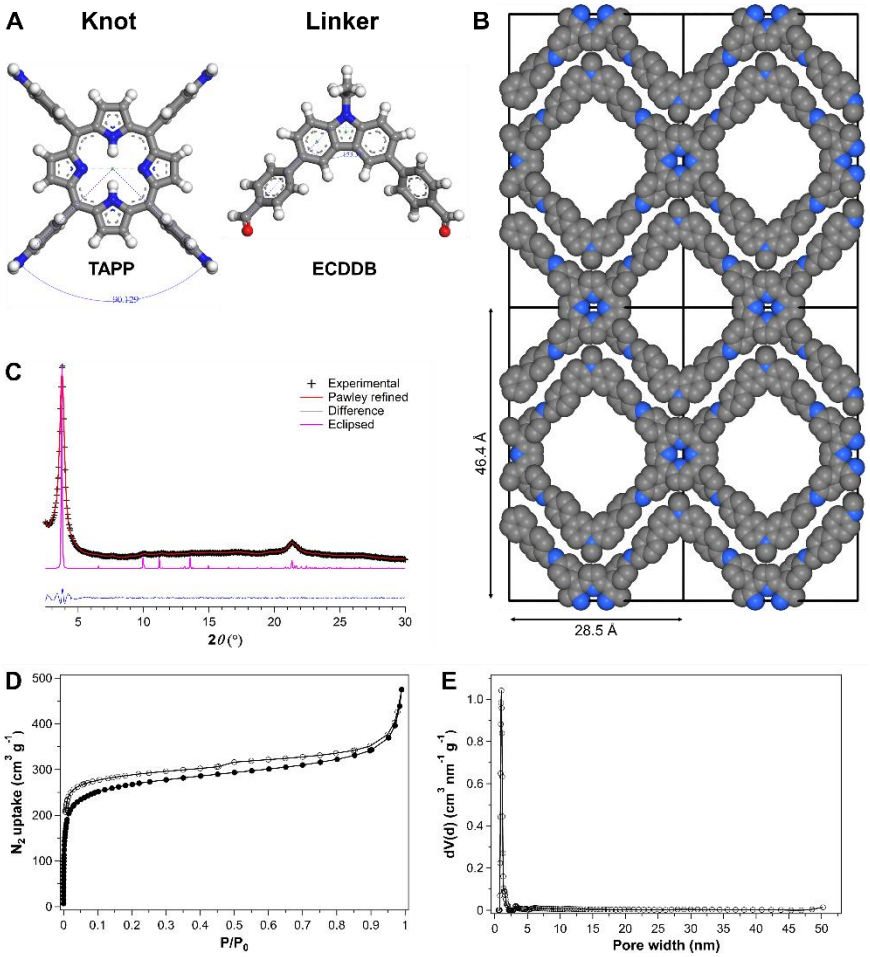

Figure 26. (A) Structures of TAPP and ECDDB; (B) The eclipsed structure (H is omitted for clarity) of TAPP-ECDDB 1D COF; (C) The Pawley refinement (R_{wp}:2.85%, R_p:2.23%); (D) N_2 isotherms; (E) Pore size distribution calculated after fitting QSDFT (slit/cylindr./sphere) models to adsorption data.

The crystallinity and porosity of 1D COFs are significantly affected by the geometric structure of linkers. Good geometrical matching leads to the easy combination between V-type linkers and tetrahedral knots. Therefore, TAPP having ~90º angles can pair with the orthogonal linker ECDDB (**Figure 26A**) very well producing TAPP-ECDDB 1D COF (**Figure 26B**) with a good crystallinity (**Figure 26C**) as well as high surface areas (**Figure 26D**) (BET and Langmuir surface areas are 1010 $m^2 g^{-1}$ and 1155 $m^2 g^{-1}$) with a pore size of 1.0 nm (**Figure 26E**), which are comparable with those of 2D and 3D COFs based on porphyrin found relatively difficult to build a COF. [53,54]

Knots and linkers with different angles

Although PyTTA and ETTA possess an angle larger than 90º compared with that (~90°) of ECDDB (**Figure 27A**), PyTTA and ETTA can form PyTTA-ECDDB 1D COF and ETTA-ECDDB 1D COF (**Figure 27B-E**). This is ascribed to the larger torsion for the conjugation plane of ECDDB and PyTTA/ETTA. This seems to allow for a short alkyl chain of ECDDB folding between layers and counteract the geometrical tension easily because imine bonds are more flexible than other bonds such as boronate and triazine bonds. Similar with other 1D COFs, these three ECDDB based 1D COFs all have ~0.9 nm aperture (**Table 1**), sufficing to prove the 1D construction. Meanwhile, this provides an alternative strategy to introduce unconjugated group into the skeleton of 1D COFs. However, we assume 1D COFs based on other rigid linkages like boronate and triazine bonds would keep more strict geometrical consistency between knots and linkers.

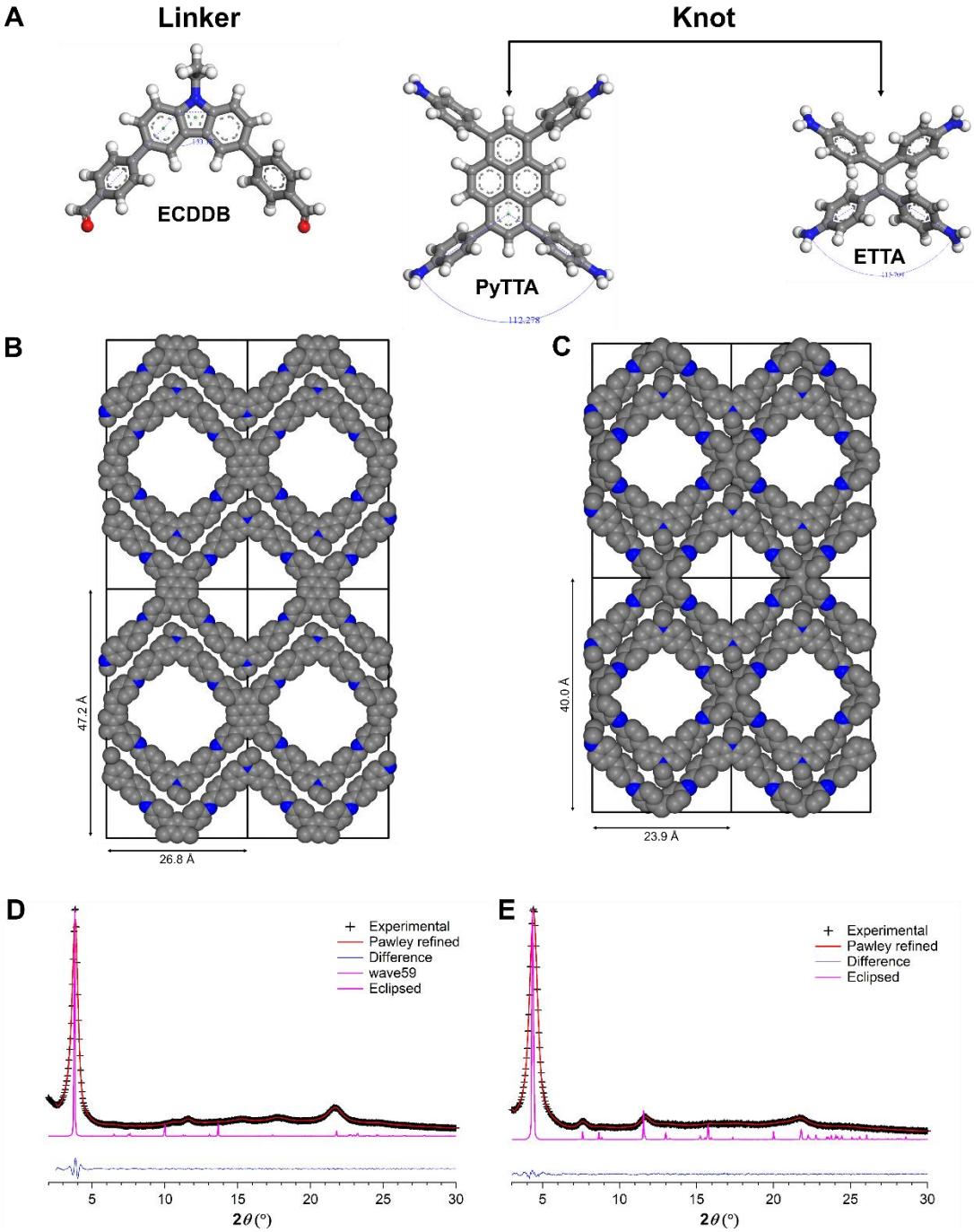

Figure 27. (A) Structures of ECDDB, PyTTA and ETTA; (B) The eclipsed structure (H is omitted for clarity) of (B) PyTTA-ECDDB 1D COF and (C) ETTA-ECDDB 1D COF; The Pawley refinement of (D) PyTTA-ECDDB 1D COF (R_{wp}:3.05%, R_p:2.22%) and (E) ETTA-ECDDB 1D COF (R_{wp}:2.40%, R_p:1.87%).

Morphology

We investigated the morphology of 1D COFs by FE-SEM. For example, PyTTA-TF-*m*-TPDC 1D COF is composed of random loose networks as shown in **Figure 28A**. We also investigated 1D COFs by TEM in order to gain insight into direct space information.

However, they are so sensitive to the high intensity of the electron beam that they will rapidly become amorphous even be damaged structurally and only an approximate pore structure could be observed with this technique. [55] Even so, the TEM image of 1D COFs for example PyTTA-TF-*m*-TPDC 1D COF (**Figure 28B**) especially TAPP-ECDDB 1D COF (**Figure 28C**) still reveals a high degree of crystallinity and order, as demonstrated by the honeycomb-type facets with a distance of about ~1.3 nm determined by the corresponding FFT image (**Figure 28D**).

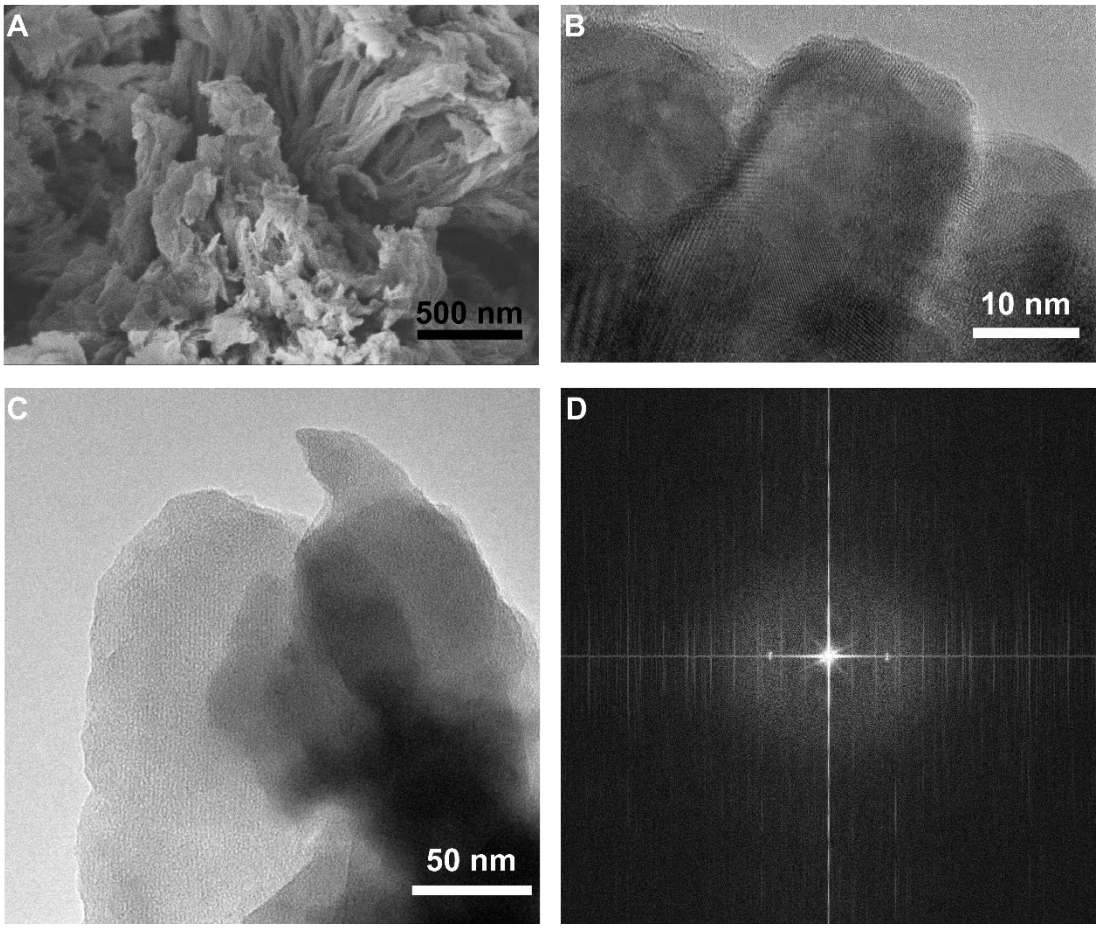

Figure 28. Morphology. (A) FE-SEM image of PyTTA-TF-*m*-TPDC 1D COF; HR-TEM images of (B) PyTTA-TF-*m*-TPDC 1D COF and (C) TAPP-ECDDB 1D COF; (D) corresponding FFT image of TAPP-ECDDB 1D COF.

Table 1. The summary of BET surface areas, Langmuir surface areas, micropores contribution and mean crystalline size.

COFs	BET surface area ($m^2 g^{-1}$)	Langmuir surface area ($m^2 g^{-1}$)	Micropores contribution ($m^2 g^{-1}$)	Pore size (nm)
BATPDA-TPDC 1D COF	325	357	314 (96.6%)	0.85
ETTA-*m*-TPDC 1D COF	717	911	539 (75.2%)	1.1
PyTTA-*m*-TPDC 1D COF	949	1046	809 (85.2%)	0.93
PyTTA-PDDC 1D COF	729	837	495 (67.9%)	0.97
PyTTA-PTPDC 1D COF	859	901	782 (91.0%)	0.93
PyTTA-TF-*m*-TPDC 1D COF	1225	1346	1115 (91.0%)	0.93
PyTTA-ECDDB 1D COF	1063	1171	987 (92.9%)	1.0
ETTA-ECDDB 1D COF	919	1053	748 (81.4%)	0.93
TAPP-ECDDB 1D COF	1010	1155	878 (86.9%)	1.0
PyTTA-BFTDC 2D COF	1044	1133	877 (84.0%)	0.82
PyTTA-BFDMTDC 2D COF	878	922	785 (89.4%)	0.82
BATPDA-BFTDC 2D COF	654	764	467 (71.4%)	0.85
BATPDA-BFDMTDC 2D COF	1013	1194	774 (76.4%)	0.85

Various 2D and 3D COFs have been synthesized through a variety of methods. However, due to the limited applicable reactions and building blocks, it is difficult to design and synthesize a new COF to meet the requirement of various application and demand of exploring the relevant mechanism. Recently, interwoven COFs consisting of 1D organic thread have been reported. However, the surface area is very low and the crystallinity decreases after removing the metal. It remains a challenge to achieve a truly crystalline and stable 1D COFs without metal-coordination interaction. In this chapter, we have successfully synthesized new 2D COFs via [4 + 4] pathway and built a systematic methodology of constructing 1D COFs.

Most of 2D COFs are synthesized via [3 + 2], [3 + 3], [4 + 2] or [6 + 2] pathway because one of building blocks is a small and linear monomer so that it can easily keep the balance between the free movement of monomers during the reaction and the interlayered

interaction facilitating the formation of COFs. By contrast, it seems hardly to form a COF using two tetragonal building blocks due to the rigid conjugation and larger size. However, it is possible to construct 2D [4 + 4] COFs in theory if the geometric matching between two tetragonal building blocks is good enough to offset the difficulty of movement by scanning the reaction condition and via on-surface synthesis. On the other hand, COFs are believed to often exist in the form of 2D and 3D since 1D structures are too flexible to form an order crystalline solid. Therefore, most researchers focus on designing an ideal 2D or 3D topology before synthesis. However, this prejudice hinders the development of 1D COFs.

In this chapter, we synthesized 2D [4 + 4] COFs and 1D COFs and confirmed their structures by various methods. First, FTIR, solid-state NMR and XPS spectrum verified the formation of imine bond in 2D [4 + 4] COFs and 1D COFs. Their microporosities (pore size: ~1 nm) and large surface area were determined by N_2 isotherm. Their exact crystal structures by comparing their experimental PXRD patterns with the theoretically simulated ones. The crystal structures of 2D [4 + 4] COFs can be confirmed more easily owing to the only one possible topology. By contrast, it is a little complicated to determine the crystal structures of 1D COFs due to the possibility of other 2D structures. After comparing the experimental pore size and PXRD patterns with the theoretically simulated ones, 1D structure can be considered as the most possible. A lot of successful 2D and 1D COFs examples suggest the geometry of knots and linkers and their matching play an important role on the formation of COFs. When the angle of knots and linkers are close, it is easy to fabricate COFs. For instance, TAPP having ~90º angles can pair with the orthogonal linker ECDDB with an angle of ~90º very well producing TAPP-ECDDB 1D COF. Moreover, various heteroatoms and functional groups such as methyl groups and phenyl groups can be introduced into the framework without changing the crystal structure, indicating the high designability of 2D and 1D COFs. However, some functional groups like TMS may cause monomers too flexible to form a crystalline solid. On the other hand, even though the geometric matching between knots and linkers is not so good, it is possible to form a 1D COF when the difference is not so large. For example, PyTTA-ECDDB 1D COF can be formed by PyTTA possessing an angle of ~120º and ECDDB with an angle of ~90º.

Moreover, the size of building blocks also affects the formation of COFs. For example, isophthalaldehyde with an angle of ~120º is hardly to combine with PyTTA to forming 1D COF likely due to more defects.

5. Brief summary

In conclusion, a new strategy for construction of 2D [4 + 4] COFs and 1D COFs with various topological structures has been developed. This strategy leads to the successful construction of COFs bearing micropores, high surface area and high crystallinity. Furthermore, the functionalization has been realized due to the high designability of COFs. This work not only indicates that 2D COFs can be facilely constructed from simple tetragonal building blocks via [4 + 4] pathway but also suggests a promising way to fabricate 1D COFs by considering the geometry, size and other possible property of linkers. This sheds new light on the development of new strategies for the construction of COFs and the control the dimension of COFs at molecular level. We believe these COFs will be potential in various fields such as gas capture and separation. Moreover, if the 2D [4 + 4] COF monolayers and 1D COF single chains via on-surface synthesis can be obtained, not only their more detailed precise crystal structure will be determined, but also it is useful to explore the topological behavior of COFs. The single-crystal 2D [4 + 4] COFs and 1D COFs will be the focus of future plan to estimate the relationship between structure and performance.

References

1. Feng, X.; Ding, X.; Jiang, D. *Chem. Soc. Rev.* **2012**, *41*, 6010.
2. Furukawa, H.; Yaghi, O. M. *J. Am. Chem. Soc.* **2009**, *131*, 8875.
3. Xu, H.; Gao, J.; Jiang, D. *Nat. Chem.* **2015**, *7*, 905.
4. Lin, S.; Diercks, C. S.; Zhang, Y.-B.; Kornienko, N.; Nichols, E. M.; Zhao, Y.; Paris, A. R.; Kim, D.; Yang, P.; Yaghi, O. M.; Chang, C. J. *Science* **2015**, *349*, 1208.
5. Liu, X.-H.; Guan, C.-Z.; Ding, S.-Y.; Wang, W.; Yan, H.-J.; Wang, D.; Wan, L.-J. *J. Am. Chem. Soc.* **2013**, *135*, 10470.

6. Feng, X.; Liu, L.; Honsho, Y.; Saeki, A.; Seki, S.; Irle, S.; Dong, Y.; Nagai, A.; Jiang, D. *Angew. Chem. Int. Ed.* **2012**, *51*, 2618.
7. Diercks, C. S.; Yaghi, O. M. *Science* **2017**, *355*, eaal1585.
8. Côté, A. P.; Hani, M. E.-K; Furukawa, H.; Hunt, J. R.; Yaghi, O. M. *J. Am. Chem. Soc.* **2007**, *129*, 12914.
9. Liu, X.-H.; Guan, C.-Z.; Wang, D.; Wan, L.-J. *Adv. Mater.* **2014**, *26*, 6912.
10. Hao, G. P.; Li, W. C.; Qian, D.; Lu, A. H. *Adv. Mater.* **2010**, *22*, 853.
11. Zeng, Y.; Zou, R.; Zhao, Y. *Adv. Mater.* **2016**, *28*, 2855.
12. Huang, N.; Chen, X.; Krishna, R.; Jiang, D. *Angew. Chem. Int. Ed.* **2015**, *54*, 2986.
13. Liu, H.; Zhao, Y.; Zhang, Z.; Nijem, N.; Chabal, Y. J.; Zeng, H.; Li, J. *Adv. Funct. Mater.* **2011**, *21*, 4754.
14. Lohse, M. S.; Bein, T. *Adv. Funct. Mater.* **2018**, *28*, 1705553.
15. Diercks, C. S.; Yaghi, O. M. *Science* **2017**, *355*, eaal1585.
16. Lin, S.; Diercks, C. S.; Zhang, Y.-B.; Kornienko, N.; Nichols, E. M.; Zhao, Y.; Paris, A. R.; Kim, D.; Yang, P.; Yaghi, O. M.; Chang, C. J. *Science* **2015**, *349*, 1208.
17. Medina, D. D.; Sick, T.; Bein, T. *Adv. Energy Mater.* **2017**, *7*, 1700387.
18. Ding, S.; Wang, W. *Chem. Soc. Rev.* **2013**, *42*, 548.
19. Huang, N.; Wang, P.; Jiang, D. *Nat. Rev. Mater.* **2016**, *1*, 16068.
20. Gao, Q.; Li, X.; Ning, G.-H.; Leng, K.; Tian, B.; Liu, C.; Tang, W.; Xu, H.-S.; Loh, K. P. *Chem. Commun.* **2018**, *54*, 2349.
21. Tian, Y.; Xu, S.-Q.; Qian, C.; Pang, Z.-F.; Jiang, G.-F.; Zhao, X. *Chem. Commun.* **2016**, *52*, 11704.
22. El-Kaderi, H. M.; Hunt, J. R.; Mendoza-Cortés, J. L.; Côté, A. P.; Taylor, R. E.; O'Keeffe, M.; Yaghi, O. M. *Science* **2007**, *316*, 268.
23. Morgan, P. W.; Kwolek, S. L.; Pletcher, T. C. *Macromolecules* **1987**, *20*, 729.
24. Cooper, A. I. *Adv. Mater.* **2009**, *21*, 1291.
25. McCrum, N. G.; Buckley, C. P.; Bucknall, C. B. *Principles of polymer engineering*, Oxford University Press, USA, **1997**.

26. Liu, Y.; Ma, Y.; Zhao, Y. Sun, X.; Gándara, F.; Furukawa, H.; Liu, Z.; Zhu, H.; Zhu, C.; Suenaga, K.; Oleynikov, P.; Alshammari, A. S.; Zhang, X.; Terasaki, O.; Yaghi, O. M. *Science* **2016**, *351*, 365.
27. Carlucci, L.; Ciani, G.; Proserpio, D. M. *Coord. Chem. Rev.* **2003**, *246*, 247.
28. Zhao, Y.; Guo, L.; Gándara, F.; Ma, Y.; Liu, Z.; Zhu, C.; Lyu, H.; Trickett, C. A.; Kapustin, E. A.; Terasaki, O.; Yaghi, O. M. *J. Am. Chem. Soc.* **2017**, *139*, 13166.
29. Bessinger, D.; Ascherl, L.; Auras, F.; Bein, T. *J. Am. Chem. Soc.* **2017**, *139*, 12035.
30. Schwab, M. G.; Hamburger, M.; Feng, X.; Shu, J.; Spiess, H. W.; Wang, X.; Antonietti, M.; Müllen, K. *Chem. Commun.* **2010**, *46*, 8932.
31. Lin, Y.; Jiang, X.; Kim, S. T.; Alahakoon, S. B.; Hou, X.; Zhang, Z.; Thompson, C. M.; Smaldone, R. A.; Ke, C. *J. Am. Chem. Soc.* **2017**, *139*, 7172.
32. Chen, X.; Addicoat, M.; Jin, E.; Zhai, L.; Xu, H.; Huang, N.; Guo, Z.; Liu, L.; Irle, S.; Jiang, D. *J. Am. Chem. Soc.* **2015**, *137*, 3241.
33. Altarawneh, S.; Behera, S.; Jena, P.; El-Kaderi, H. M. *Chem. Commun.* **2014**, *50*, 3571.
34. Giacalone, F.; Campisciano, V.; Calabrese, C.; Parola, V. L.; Syrgiannis, Z.; Prato, M.; Gruttadauria, M. *ACS Nano* **2016**, *10*, 4627.
35. Kuhnert, N.; Patel, C.; Jami, F. *Tetrahedron Lett.* **2015**, *46*, 7575.
36. Selivanova, A. V.; Tyurin, V. S.; Beletskaya, I. P. *ChemPlusChem* **2014**, *79*, 1278.
37. Bunck, D. N.; Dichtel, W. R. *J. Am. Chem. Soc.* **2013**, *135*, 14952.
38. Pang, Z.-F.; Xu, S.-Q.; Zhou, T.-Y.; Liang, R.-R.; Zhan, T.-G.; Zhao, X. *J. Am. Chem. Soc.* **2016**, *138*, 4710.
39. Hu, Y.; Zhang, J.; Li, Z.; Wang, X.; Yin, J.; Liu, S. H. *Dyes Pigments* **2018**, *151*, 165.
40. Materials Studio 2018. Dassault Systèmes BIOVIA, San Diego. Available from http://www.3dsbiovia.com/products/collaborative-science/biovia-materials-studio/.
41. Xu, Q.; Tang, Y.; Zhang, X.; Oshima, Y.; Chen, Q.; Jiang D. *Adv. Mater.* **2018**, *30*, 1706330.
42. Tan, J.; Namuangruk, S.; Kong, W.; Kungwan, N.; Guo, J.; Wang, C. *Angew. Chem. Int. Ed.* **2016**, *55*, 13979.
43. Troschke, E.; Grätz, S.; Lübken, T.; Borchardt, L. *Angew. Chem.* **2017**, *129*, 6963.
44. Qian, C.; Qi, Q.-Y.; Jiang, G.-F.; Cui, F.-Z.; Tian, Y.; Zhao, X. *J. Am. Chem. Soc.* **2017**, *139*, 6736.

45. Côté, A. P.; Benin, A. I.; Ockwig, N. W.; O'Keeffe, M.; Matzger, A. J.; Yaghi, O. M. *Science* **2005**, *310*, 1166.
46. Dawson, R.; Adams, D. J.; Cooper, A. I. *Chem. Sci.* **2011**, *2*, 1173.
47. Briseno, A. L.; Mannsfeld, S. C. B.; Shamberger, P. J.; Ohuchi, F. S.; Bao, Z.; Jenekhe, S. A.; Xia, Y. *Chem*. *Mater*. **2008**, *20*, 4712.
48. Liu, X.-H.; Guan, C.-Z.; Ding, S.-Y.; Wang, W.; Yan, H.-J.; Wang, D.; Wan, L.-J. *J. Am*. *Chem*. *Soc*. **2013**, *135*, 10470.
49. Troschke, E.; Grätz, S.; Lübken, T.; Borchardt, L. *Angew*. *Chem*. **2017**, *129*, 6963.
50. Lowell, S.; Shields, J. E.; Thomas, M. A.; Thomas, M. *Characterization of porous solids and powders: surface area, pore size and density* (*16*, Springer Science & Business Media, New York, **2012**).
51. Auras, F.; Ascherl, L.; Hakimioun, A. H.; Margraf, J. T.; Hanusch, F. C.; Reuter, S.; Bessinger, D.; Döblinger, M.; Hettstedt, C.; Karaghiosoff, K.; Herbert, S.; Knochel, P.; Clark, T.; Bein, T. *J. Am*. *Chem*. *Soc*. **2016**, *138*, 16703.
52. Nagai, A.; Guo, Z.; Feng, X.; Jin, S.; Chen, X.; Ding, X.; Jiang, D. *Nat*. *Commun*. **2011**, *2*, 536.
53. Diercks, C. S.; Lin, S.; Kornienko, N.; Kapustin, E. A.; Nichols, E. M.; Zhu, C.; Zhao, Y.; Chang, C. J.; Yaghi, O. M. *J. Am*. *Chem*. *Soc*. **2018**, *140*, 1116.
54. Lin, G.; Ding, H.; Chen, R.; Peng, Z.; Wang, B.; Wang, C. *J. Am. Chem*. *Soc*. **2017**, *139*, 8705.
55. Roeser, J.; Prill, D.; Bojdys, M. J.; Fayon, P.; Trewin, A.; Fitch, A. N.; Schmidt, M. U.; Thomas, A. *Nat*. *Chem*. **2017**, *9*, 977.

Chapter III: Covalent Organic Frameworks for Carbon Dioxide Capture and Separation

Abstract

In the chapter II, we synthesized microporous 2D [4 + 4] COFs and 1D COFs. In this chapter, we utilized these COFs to investigate CO_2 capture. Owing to the micropores (~1 nm), large BET surface (300-1250 $m^2 g^{-1}$) and large pore volume (0.6-1.2 $cm^{-3} g^{-1}$) render these COFs show high capacities for CO_2 capture. The introducing of methyl groups has a complicated effect on surface are area, pore volume and crystal size. Moreover, methyl group decorated COFs exhibit much enhanced capacities for CO_2 capture due to the interaction between CO_2 and methyl group, suggesting that methyl group functionalized COFs could outperform those "active" group-based sorbents in CO_2 capture and separation application. 1D COFs also demonstrate a good separation of CO_2 over N_2 and CH_4.

1. Introduction

As one of greenhouse gases, CO_2 is continuously released in an increasing pace along with the increased consumption of fossil fuels and the destruction of vegetation. [1] In order to fight against global warming and climate change, it is urgent to remove CO_2 from air and flue gas. [2] Compared with aqueous solution of amine derivatives, using porous materials to capture CO_2 is an energy-saving manner. [3] As a class of lightweight materials, COFs have been paid much attention due to their designable porous structure especially controllable pore interface by pore surface engineering. This structural designability is important for adsorption of CO_2. Moreover, compare with other porous materials like MOFs, COFs are immune to water due to the lack of strong interaction between metal sites and these polar gases. [4] Pore volume and pore size are important parameters that determine the gas storage capability. In general, smaller pore size and larger pore volume often means higher CO_2 capability. In addition, introducing functional groups to the pore walls is an alternative way to improve the CO_2 capability. "Active" functional groups such as

hydroxyl or carboxyl groups are often used to decorate the pore surface of COFs, however, inevitable decrease in the BET surface area, pore volume, and interpenetration and/or severe structure distortion of frameworks appear. [5] By contrast, methyl groups not only avoid these problems but facilitate to form hydrogen-bond-like interactions with CO_2 to enhance the adsorption capacity. [6] In this chapter, 2D [4 + 4] COFs and 1D COFs will be utilized to capture and separate CO_2 based on their unique porosities and surface properties.

2. Experimental section

Commercial reagents and solvents were purchased from Sigma-Aldrich, Kanto Chemical or Fujifilm Wako Chemical and used as received.

2.1 Monomers synthesis

4,4',4'',4'''-(pyrene-1,3,6,8-tetrayl)tetraaniline (PyTTA) [7]

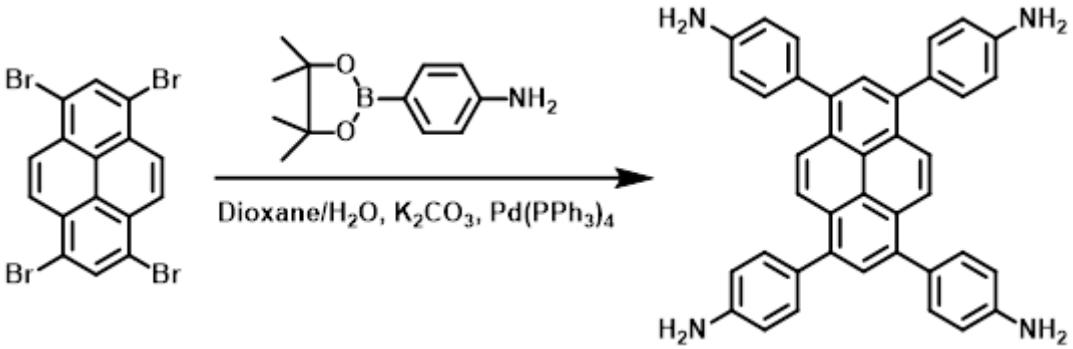

1,3,6,8 tetrabromopyrene (2.0 g, 3.86 mmol), 4-(4,4,5,5-tetramethyl-1,3,2-dioxaborolan-2-yl)aniline (3.8 g, 17.4 mmol), K_2CO_3 (2.9 g, 21.2mmol), and $Pd(PPh_3)_4$ (445 mg, 0.39 mmol) were added into dioxane/H_2O (5:1 v/v, 42 mL) and heated to reflux for 3 days. After cooling to room temperature, H_2O (50 mL) was added. The resulting precipitate was collected via filtration and was washed with H_2O and methanol. Recrystallization from dioxane, followed by drying under high vacuum to give **PyTTA** (1.97 g, 90%) as a yellow solid. ^{1}H NMR (400 MHz, DMSO-d_6) δ: 8.13 (s, 4H), 7.79 (s, 2H), 7.36, 7.34 (d, J=8.3 Hz, 8H), 6.78, 6.76 (d, J=8.3 Hz, 8H), 5.32 (s, 8H).

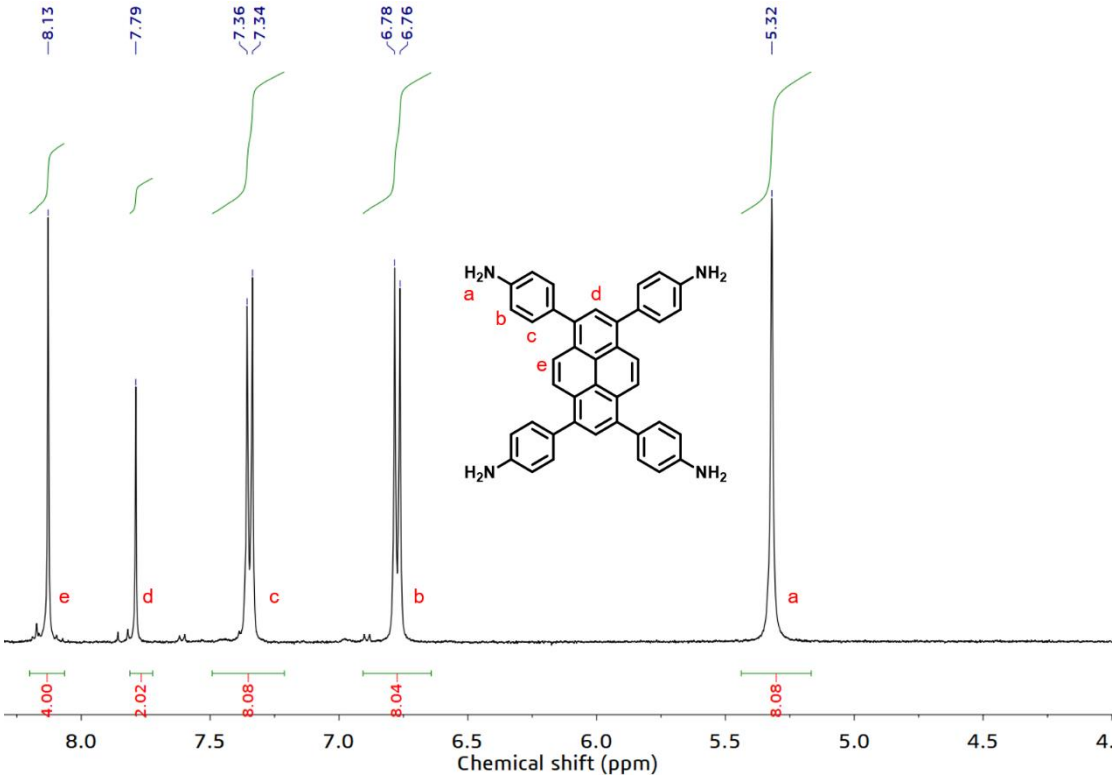

4',5'-bis(4-aminophenyl)-1,1':2',1''-terphenyl-4,4''-diamine (BATPDA) [8]

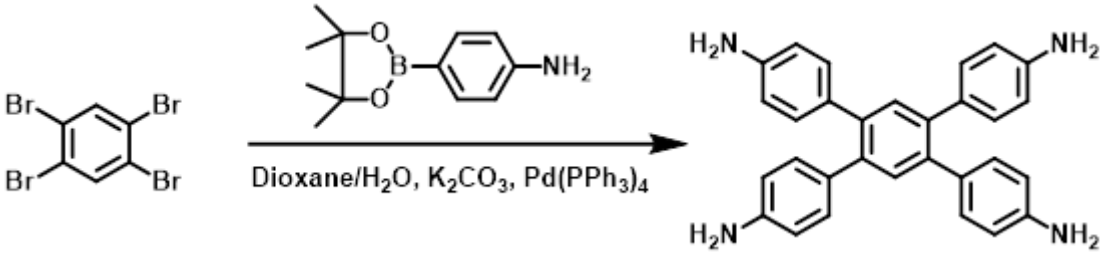

1,2,4,5-tetrabromobenzene (1.5 g, 3.8 mmol), 4-(4,4,5,5-tetramethyl-1,3,2-dioxaborolan-2-yl)aniline (3.7 g, 17.1 mmol), K_2CO_3 (2.1 g, 15.7 mmol), and $Pd(PPh_3)_4$ (439 mg, 0.38 mmol) were added into dioxane/H_2O (5:1, v/v, 36 mL) and heated to reflux for 3 days. After cooling to room temperature, H_2O (50 mL) was added. The resulting precipitate was collected via filtration and was washed with H_2O and methanol. Recrystallization from dioxane, followed by drying under high vacuum to give **BATPDA** (1.8 g, 90%) as a gray solid. ^{1}H NMR (400 MHz, $CDCl_3$) δ: 7.39 (s, 2H), 7.04, 7.02 (d, J=8.5 Hz, 8H), 6.58, 6.56 (d, J=8.1 Hz, 8H).

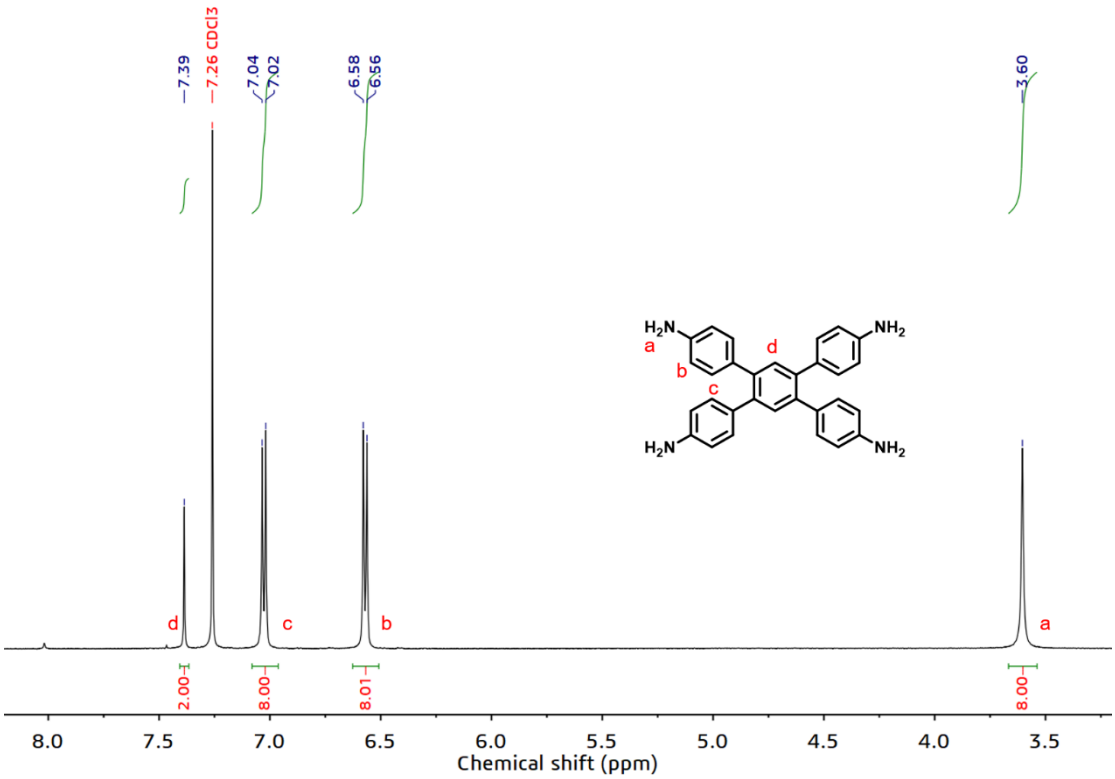

4',5'-bis(4-formylphenyl)-1,1':2',1''-terphenyl-4,4''-dicarbaldehyde (BFTDC) [9]

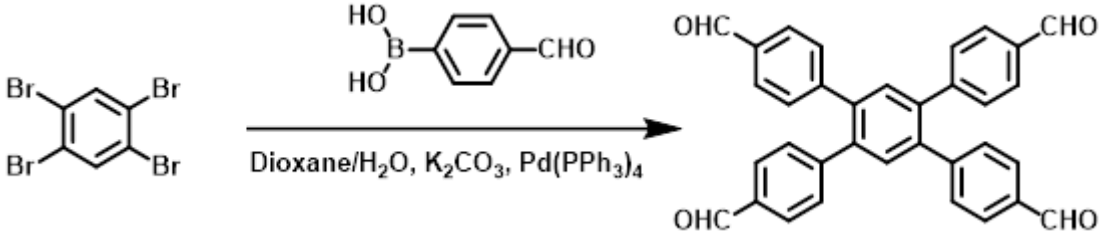

1,2,4,5-tetrabromobenzene (1.91 g, 4.84 mmol), 4-formylphenyl boronic acid (1.60 g, 10.64 mmol), K_2CO_3 (2.68 g, 19.4 mmol) and $Pd(PPh_3)_4$ (578 mg, 0.5 mmol) in dioxane/H_2O (5:1 v/v, 72 mL) were degassed and backfilled N_2 three times. The suspension was stirred under N_2 at 100 °C for 72 h. After cooling to room temperature, the mixture was concentrated and then extracted with EtOAc. The organic phase was dried over anhydrous $MgSO_4$ and then concentrated under reduced pressure to remove the solvent. The crude product was purified by silica gel column chromatography to afford **BFTDC** (1.92 g, 80%). ^{1}H NMR (400 MHz, $CDCl_3$) δ: 10.00 (s, 4H), 7.81, 7.79 (d, J=8.4 Hz, 8H), 7.60 (s, 2H), 7.40, 7.38 (d, J=8.2 Hz, 8H).

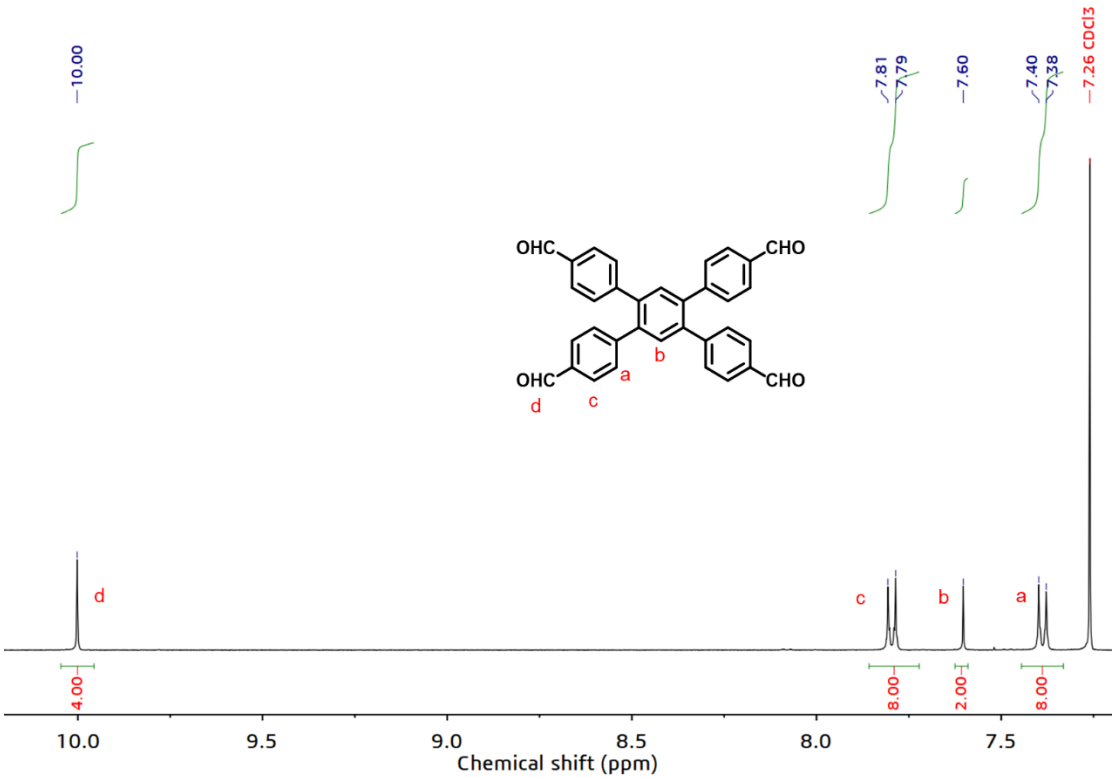

4',5'-bis(4-formylphenyl)-3',6'-dimethyl-[1,1':2',1''-terphenyl]-4,4''-dicarbaldehyde (BFDMTDC) [9]

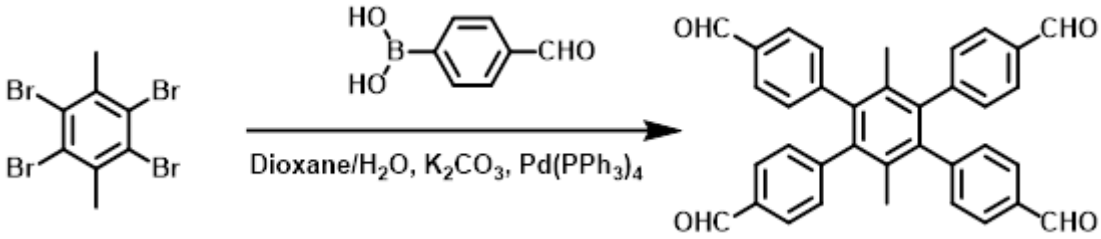

2,3,5,6-Tetrabromo-*p*-xylene (2.0 g, 4.74 mmol), 4-formylphenyl boronic acid (1.56 g, 10.42 mmol), K_2CO_3 (2.62 g, 19.0 mmol) and $Pd(PPh_3)_4$ (578 mg, 0.5 mmol) in dioxane/H_2O (5:1 v/v, 66 mL) were degassed and backfilled N_2 three times. The suspension was stirred under N_2 at 100 °C for 72 h. After cooling to room temperature, the mixture was concentrated and then extracted with EtOAc. The organic phase was dried over anhydrous $MgSO_4$ and then concentrated under reduced pressure to remove the solvent. The crude product was purified by silica gel column chromatography to afford **BFDMTDC** (1.5 g, 60%). ^{1}H NMR (400 MHz, $CDCl_3$) δ: 9.91 (s, 4H), 7.72, 7.70 (d, J=8.3 Hz, 8H), 7.25, 7.23 (d, J=8.1 Hz, 8H), 1.77 (s, 6H).

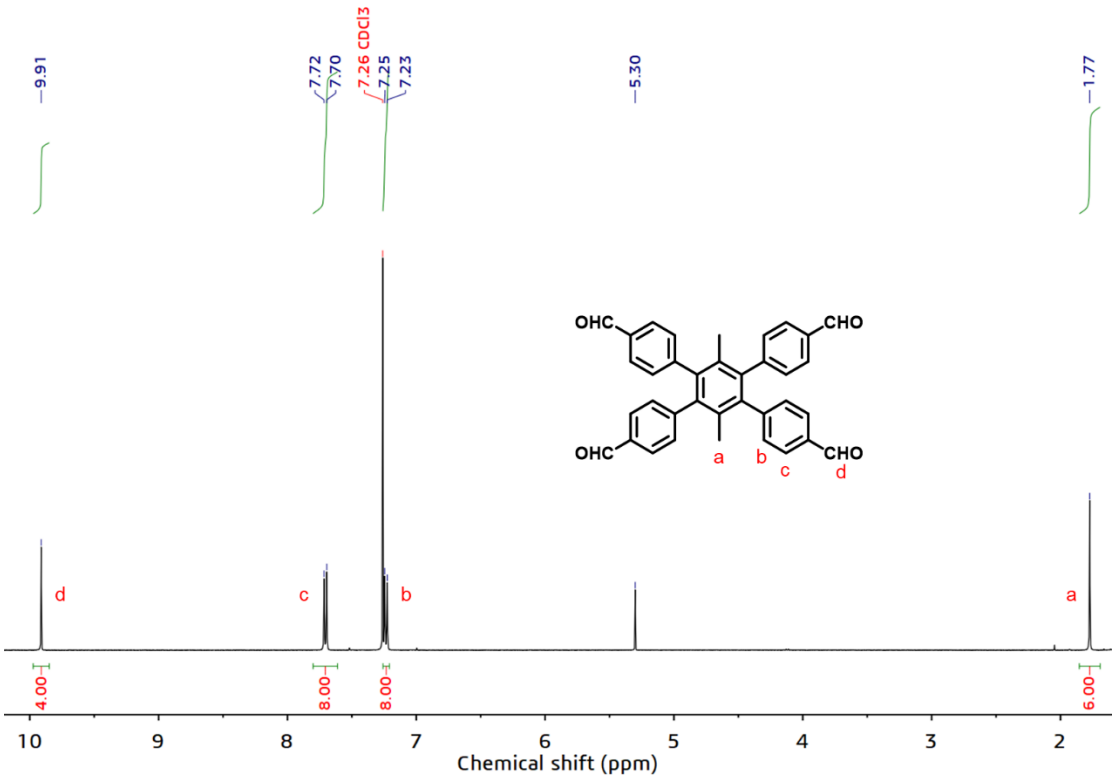

1,1':3',1''-terphenyl-4,4''-dicarbaldehyde (*m*-TPDC) [10]

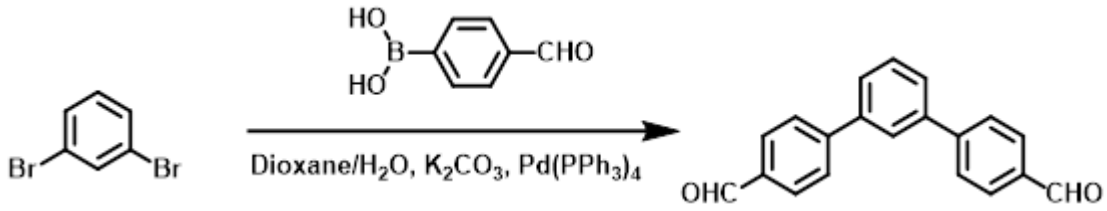

1,3-dibromobenzene (1.0g, 4.24 mmol), 4-formylphenyl boronic acid (2.50g, 17.0 mmol), K_2CO_3 (2.35 g, 17.0 mmol) and $Pd(PPh_3)_4$ (160 mg, 0.14 mmol) in dioxane/H_2O (5:1 v/v, 36 mL) were degassed and backfilled N_2 three times. The suspension was stirred under N_2 at 100 °C for 72 h. After cooling to room temperature, the mixture was concentrated and then extracted with EtOAc. The organic phase was dried over anhydrous $MgSO_4$ and then concentrated under reduced pressure to remove the solvent. The crude product was purified by silica gel column chromatography to afford ***m*-TPDC** (1.10 g, 91%). ^{1}H NMR (400 MHz, $CDCl_3$) *δ*:10.09 (s, 2H), 8.00, 7.99 (d, *J*=8.1 Hz, 4H), 7.88 (s, 1H), 7.83, 7.81 (d, *J*=8.1 Hz, 4H), 7.70, 7.69, 7.68 (t, *J*=7.4 Hz, 9.0 Hz, 2H), 7.62-7.59 (m, *J*=7.9 Hz, 15.4 Hz, 1H).

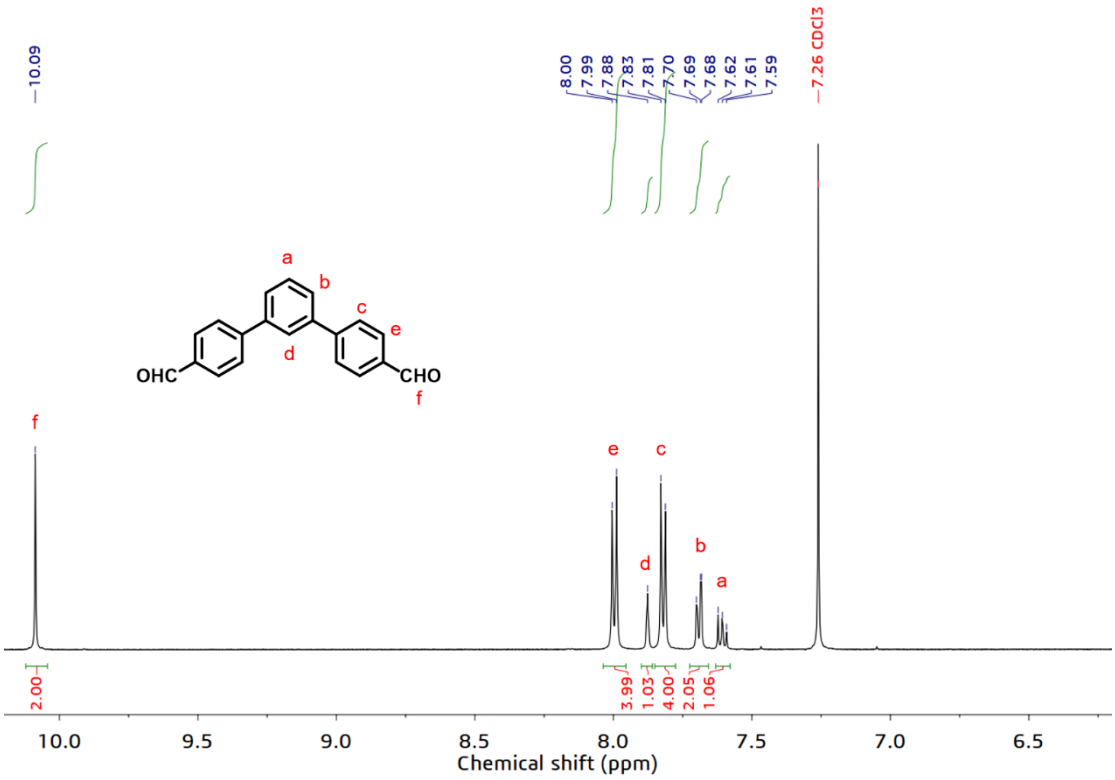

2.2 COFs synthesis

PyTTA-BFTDC COF

A Pyrex tube measuring 10 × 8 mm (o.d × i.d) was charged with PyTTA (11.5 mg, 0.02 mmol), BFTDC (9.9 mg, 0.02 mmol), mesitylene (0.48 mL), dioxane (0.32 mL), and 6 M aqueous acetic acid (0.08 mL). The tube was flash frozen at in liquid N_2 bath for three freeze-pump-thaw cycles and flame sealed. The reaction was heated at 120 ºC for 120 hours yielding a yellow precipitate at the bottom of the tube, which was isolated by filtration with THF. The wet sample was then transferred to a Soxhlet extractor and thoroughly washed with THF for 48 h and dried under vaccum at 100 ºC for 6 h. Calcd. for $C_{74}H_{44}N_4$: C, 89.85%; N, 5.66%; H, 4.39% (C:N=15.87:1:0.78). Found C, 84.89%; N, 3.22% (C:N=26.36:1) by XPS and C, 72.17%; N, 4.59%; H, 4.01% (C:N:H=15.72:1:0.87) by elemental analysis.

PyTTA-BFDMTDC COF

The synthesis was carried out following the same protocol as for PyTTA-BFTDC COF, by replacing BFTDC with BFDMTDC (10.5 mg, 0.02 mmol) and changing the amount of

mesitylene and dioxane to 0.60 mL/0.30 mL. Calcd. for $C_{76}H_{48}N_4$: C, 89.74%; N, 5.51%; H, 4.75% (C:N:H=16.29:1:0.86). Found C, 92.01%; N, 4.95% (C:N=18.59:1) by XPS and C, 80.61%; N, 4.87%; H, 4.73% (C:N:H=16.55:1:0.97) by elemental analysis.

BATPDA-BFTDC COF

The synthesis was carried out following the same protocol as for PyTTA-BFTDC COF, by replacing PyTTA with BATPDA (8.8 mg, 0.02 mmol) and changing the amount of mesitylene and dioxane to 0.60 mL/0.30 mL. Calcd. for $C_{64}H_{40}N_4$: C, 88.86%; N, 6.48%; H, 4.66% (C:N:H=13.71:1:0.72). Found C, 88.15%; N, 5.37% (C:N=16.42:1) by XPS and C, 77.41%; N, 5.30%; H, 4.58% (C:N:H=14.61:1:0.86) by elemental analysis.

BATPDA-BFDMTDC COF

The synthesis was carried out following the same protocol as for PyTTA-BFTDC COF, by replacing PyTTA with BATPDA (8.8 mg, 0.02 mmol), *m*-TPDC with BFDMTDC (10.5 mg, 0.02 mmol) and changing the amount of mesitylene and dioxane to 0.4 mL/0.4 mL. Calcd. for $C_{66}H_{44}N_4$: C, 88.76%; N, 6.27%; H, 4.97% (C:N:H=14.16:1:0.79). Found C, 90.36%; N, 5.18% (C:N=17.44:1) by XPS and C, 77.05%; N, 4.86%; H, 4.90% (C:N:H=15.85:1:1.01) by elemental analysis.

PyTTA-*m*-TPDC 1D COF

A Pyrex tube measuring 10 × 8 mm (o.d × i.d) was charged with PyTTA (11.5 mg, 0.02 mmol), *m*-TPDC (11.4 mg, 0.04 mmol), mesitylene (0.6 mL), dioxane (0.2 mL), and 6 M aqueous acetic acid (0.08 mL). The tube was flash frozen at in liquid N_2 bath for three freeze-pump-thaw cycles and flame sealed. The reaction was heated at 120 ºC for 120 hours yielding a yellow precipitate at the bottom of the tube, which was isolated by filtration with THF. The wet sample was then transferred to a Soxhlet extractor and thoroughly washed with THF for 48 h and dried under vaccum at 100 ºC for 6 h. Calcd. for $C_{160}H_{100}N_8$: C, 90.03%; N, 5.25%; H, 4.72% (C:N:H=17.15:1:0.90). Found C, 90.65%; N, 5.49% (16.51:1) by XPS and C, 82.26%; N, 5.06%; H, 4.69% by elemental analysis.

3. Characterization

Solution phase ^{1}H NMR spectroscopy was carried out using a Bruker AvanceIII400 MHz NMR spectrometer using the residual protonated solvent resonance as an internal standard. X-ray photoelectron spectra (XPS) were recorded on an Shimadzu/Kratos X-ray AXIS-ULTRA DLD XPS spectrometer with Al K_{α} radiation as X-ray source for radiation. The binding energy values of all core-level spectra were referenced to the C 1s neutral-carbon peak at 284.8 eV. The XPS peaks were deconvoluted into different components after subtraction of the background using the Shirley method. Powder X-ray diffraction (PXRD) data were recorded on a Rigaku SmartLab diffractometer by depositing powder on glass substrate. The size of crystals particles was determined by Scherrer equation.The Carbon dioxide and nitrogen uptake curves were measured at 273 K with a Bel Japan Inc. BELSORP-mini II. By using nonlocal density functional theory (NLDFT) model, the pore size was derived from the sorption curve. Breakthrough curves were obtained at 298 K by a hand-made apparatus equiped with a stainless-steel column and gas chromatograph. [11,12]

4. Results and discussions

The porosities of 2D [4 + 4] COFs have been evaluated in Chapter II. Considering the micropore (< 1 nm) and high BET surface area (650-1100 $m^2 g^{-1}$), these COFs might have a good potential for CO_2 capture. The CO_2 uptake curves were measured at 273 K as shown in **Figure 1**. At 1 atm, the CO_2 uptake capacity for PyTTA-BFTDC COF was 79.9 mg g^{-1}, while PyTTA-BFDMTDC COF revealed a higher capacity of 100.2 mg g^{-1}, which is among the top ranks of COFs materials for CO_2 adsorption as shown in **Table 1**. Similarly, compared with BATPDA-BFTDC COF (69.2 mg g^{-1}), BATPDA-BFDMTDC COF also showed an increased CO_2 uptake capacity of 82.6 mg g^{-1}. This indicates the CO_2 uptake capacity of methyl group decorated COFs is higher than that of undecorated ones.

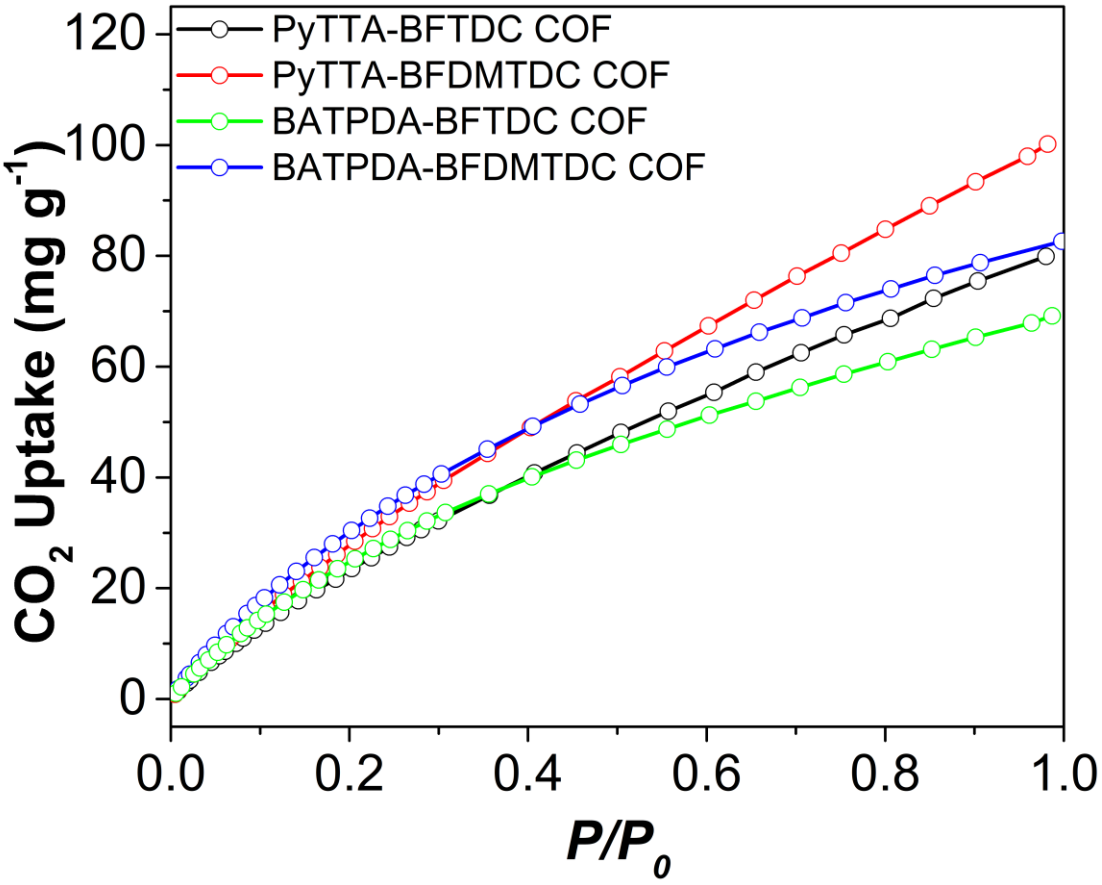

Figure 1. (A) CO_2 uptake curves at 273 K for PyTTA-BFTDC COF, PyTTA-BFDMTDC COF, BATPDA-BFTDC COF and BATPDA-BFDMTDC COF.

The pore volume and surface area are believed to be the positive factor to affect the CO_2 uptake capacity of porous materials. The BET surface area of PyTTA-BFDMTDC COF (878 $m^2 g^{-1}$) and BATPDA-BFDMTDC COF (1013 $m^2 g^{-1}$) is larger than that PyTTA-BFTDC COF (741 $m^2 g^{-1}$) and BATPDA-BFTDC COF (654 $m^2 g^{-1}$). This indicates the BET surface area of 2D [4 + 4] COFs can be increased after introducing methyl groups without changing the pore size. However, the CO_2 uptake capacity is not in direct proportion to the BET surface. For example, the CO_2 uptake capacity of BATPDA-BFDMTDC COF (82.6 mg g^{-1}) is not twice as large as that of BATPDA-BFTDC COF (69.2 mg g^{-1}) even though the BET surface is increased almost to twice. In addition, from the *t*-plots (**Figure 2**), PyTTA-BFDMTDC COF and BATPDA-BFDMTDC COF demonstrated higher contributions of micropores (89.4% and 76.7%) than those of PyTTA-BFTDC COF and BATPDA-BFTDC COF and (84.5% and 71.4%), respectively, indicating more micropores can be generated by decorating with methyl groups. The more detailed pore size distribution can be

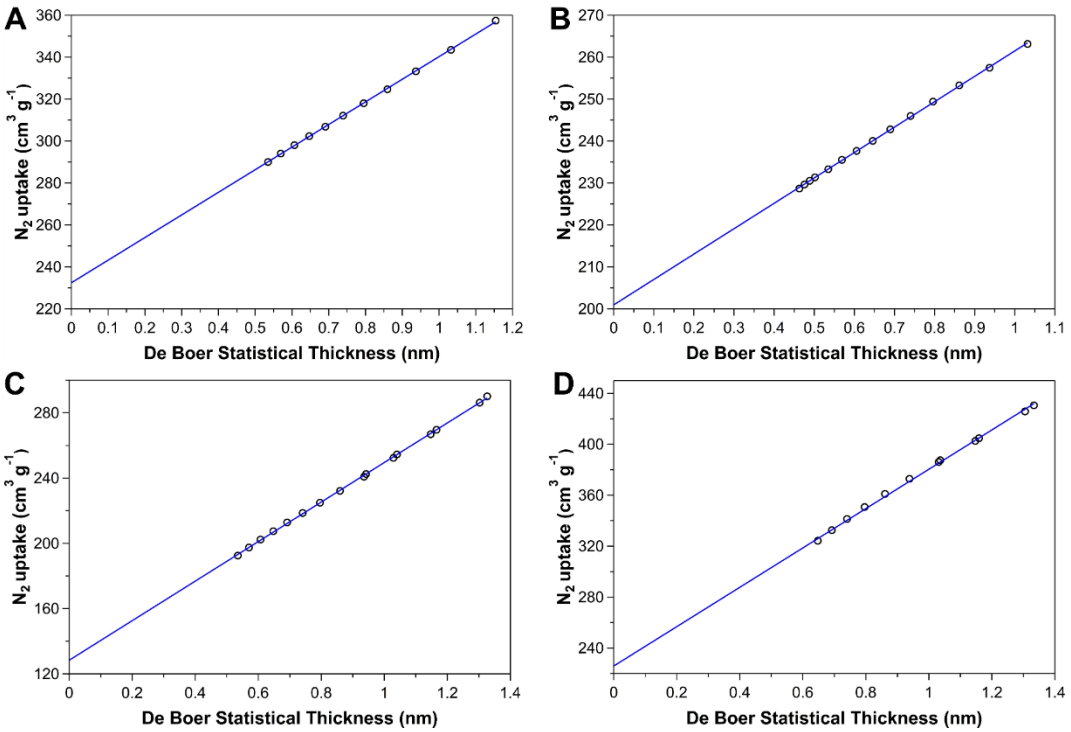

Figure 2. De Boer *t*-plot for (A) PyTTA-BFTDC COF, (B) PyTTA-BFDMTDC COF, (C) BATPDA-BFTDC COF and (D) BATPDA-BFDMTDC COF, respectively.

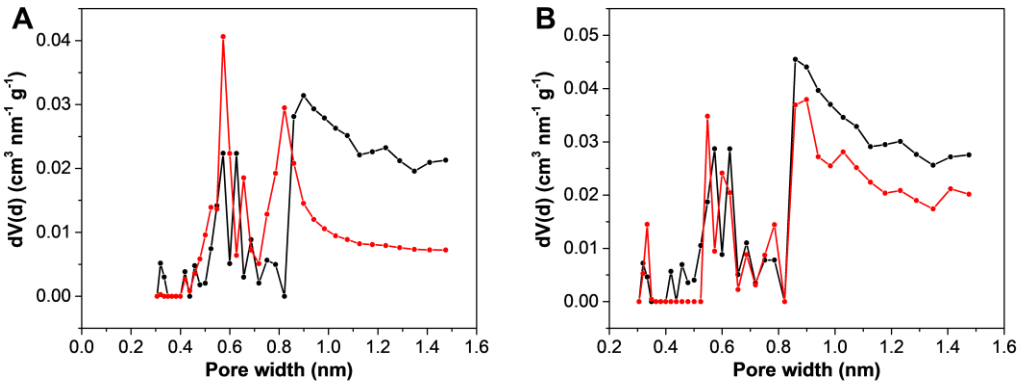

Figure 3. Pore size distributions for (A) PyTTA-BFTDC COF (black), PyTTA-BFDMTDC COF (red) and (B) BATPDA-BFTDC COF (black), BATPDA-BFDMTDC COF (red), respectively, calculated after fitting NLDFT models to adsorption data.

investigated by using CO_2 as an alternative probe due to the well-known diffusion limitations of N_2 in carbons with narrow micropores. The fitted results by the non-local density functional theory (NLDFT) model indicated plenty of pores larger than 0.8 nm besides rich micropores smaller than 0.7 nm exist in all 2D [4 + 4] COFs (**Figure 3**). This nonuniform distribution might be attributed to the amorphous phase and defects. On the other hand, the pore volume of PyTTA-BFTDC COF (0.65 $cm^3\ g^{-1}$) and PyTTA-BFDMTDC COF (0.61 $cm^3\ g^{-1}$) is almost same, while the pore volume of BATPDA-BFDMTDC COF

(1.14 $cm^3 g^{-1}$) is much larger than that of BATPDA-BFTDC COF (0.66 $cm^3 g^{-1}$), suggesting the pore volume can be retained or changed after modifying with methyl groups. This also indicating the CO_2 uptake capacity is not in direct proportion to the pore volume.

In addition, the phenomenon that the capacity of PyTTA-BFDMTDC 2D COF is higher than that of BATPDA-BFDMTDC 2D COF despite the BET surface area of PyTTA-BFDMTDC 2D COF is lower than that of BATPDA-BFDMTDC 2D COF, suggests that type of building blocks also affects the CO_2 capture. The larger better conjugation of pyrene core likely strongly affiliates CO_2.

Table 1. Porosity and CO_2 capture performance of 2D [4 + 4] COFs

COFs	BET surface area ($m^2 g^{-1}$)	Micropores contribution ($m^2 g^{-1}$)	Pore size (nm)	Pore volume ($cm^3 g^{-1}$)	CO_2 uptake (mg g^{-1})	CO_2/N_2 selectivity (w/w)
PyTTA-BFTDC	741	654 (84.5%)	0.82	0.65	79.9	14/1
PyTTA-BFDMTDC	878	785 (89.4%)	0.82	0.61	100.2	24/1
BATPDA-BFTDC	654	467 (71.4%)	0.85	0.66	69.2	20/1
BATPDA-BFDMTDC	1013	777 (76.7%)	0.85	1.14	82.6	26/1

Table 2. FWHM and mean sizes calculated from PXRD patterns of 2D [4 + 4] COFs.

COFs	FWHM	Mean size (nm)
PyTTA-BFTDC 2D COF	0.47	16.8
PyTTA-BFDMTDC 2D COF	0.90	8.8
BATPDA-BFTDC 2D COF	0.61	13.1
BATPDA-BFDMTDC 2D COF	1.29	6.2

The behavior that the CO_2 uptake capacity of porous materials is relative with the crystal size has been investigated. However, due to the difficulty of controlling the nucleation and crystallization processes, synthesis of single-crystal COFs with well-defined sizes remains a big challenge. We estimated the mean size of crystal phases in 2D [4 + 4] COFs from the PXRD patterns according to the Scherrer equation: $\tau = \frac{K\lambda}{\beta \cos\theta}$ (K=0.9, λ=1.54 Å). [13]

The mean sizes of crystals in PyTTA-BFTDC COF, PyTTA-BFDMTDC COF and BATPDA-BFTDC COF and BATPDA-BFDMTDC COF were determined as 16.8, 8.8, 13.1 and 6.2 nm, respectively (**Table 2**). Obviously, the mean size decreased after decorating

with methyl groups, suggesting the decrease of the channel length in each grain of the adsorbent, which results in high accessibility for CO_2 adsorption under the same condition. This might be ascribed to the decreased conjugation resulting in weakening the π-π interaction for crystallization after decorating with methyl groups. Moreover, due to the lower conjugation of BATPDA than PyTTA, the size of BATPDA-based COFs is a little smaller than corresponding PyTTA-based COFs. However, the size calculated by the Scherrer equation is the mean value, the distribution of crystal size as well as the contribution of amorphous phase and various crystal shape is hard to be estimated as a reference. In addition, some argue that the result will derivate the Scherrer equation for crystallite sizes up to 200 nm and less than 100 nm. [14]

Furthermore, the CO_2 uptake capacity is significantly enhanced through the interaction between functional groups like methyl groups and CO_2. [15] For example, the binding energy of benzene ring and CO_2 increases with the increasing density of methyl groups. [16] Moreover, different from those negatively charged atoms and functional groups, methyl groups serve to increase van der Waals interactions without compromising the Coulombic interactions between aromatic frameworks and CO_2. Therefore, after decorating methyl groups, CO_2 cannot freely orient itself to obtain the most favorable energetic conformation in this environment, resulting in a highly CO_2 selectivity as well. [17]

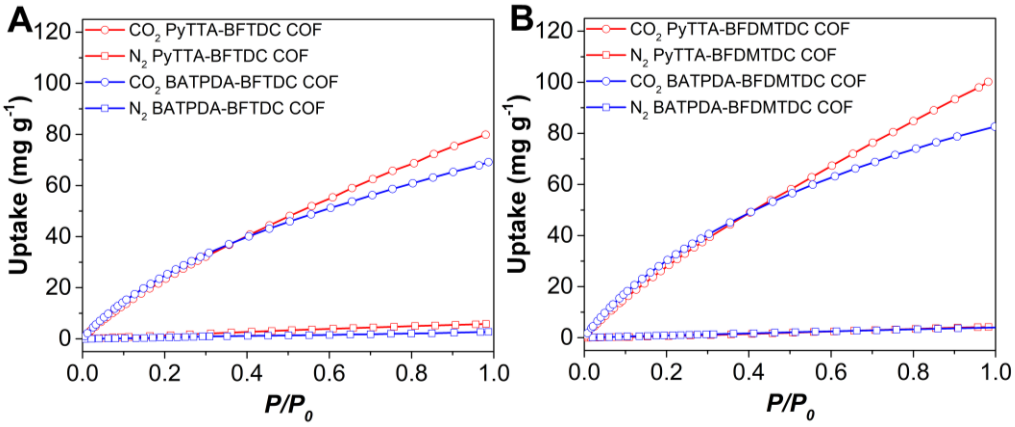

Figure 4. CO_2 and N_2 uptake curves at 273 K for PyTTA-BFTDC COF and BATPDA-BFTDC COF.

Meanwhile, at the same temperature, these 2D [4 + 4] COFs hardly adsorb N_2 owing to the hindrance of supermicropores. Among 2D [4 + 4] COFs, methyl group decorated COFs (24/1 (w/w) and 26/1 (w/w) for PyTTA-BFDMTDC COF and BATPDA-BFDMTDC

COF) revealed higher CO_2/N_2 selectivities than undecorated COFs (14/1 (w/w) and 20/1 (w/w) for PyTTA-BFTDC COF and BATPDA-BFTDC COF) at 1 atm in **Figure 4**. Moreover, 2D [4 + 4] COFs exhibited excellent cycle performances without obvious deterioration in uptake capacity after five cycles (**Figure 5**).

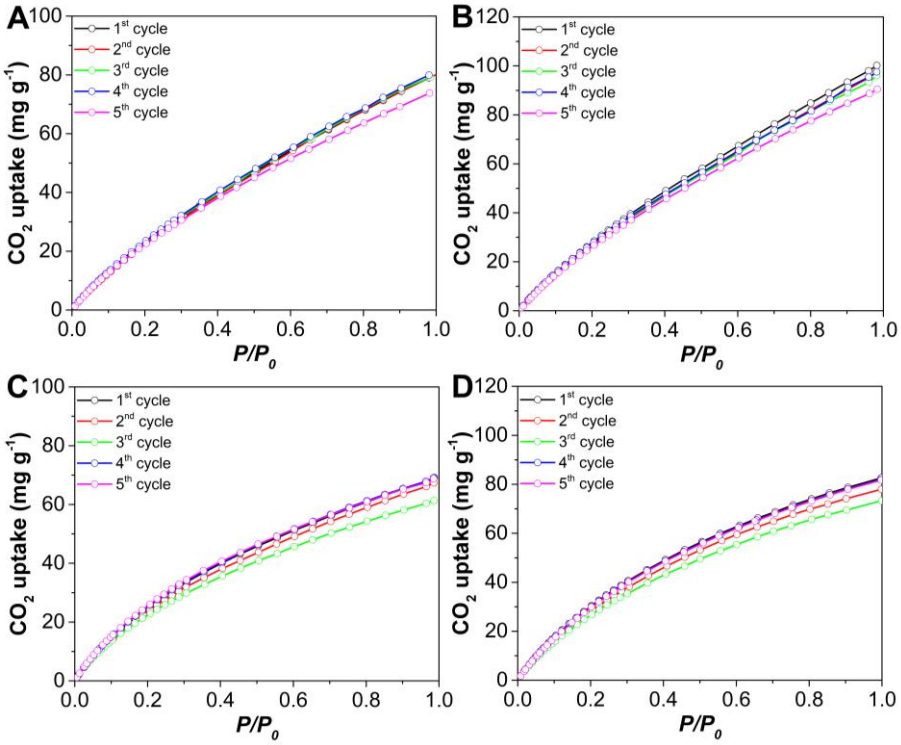

Figure 5. Cycle performances at 273 K of CO_2 uptake for (A) PyTTA-BFTDC COF, (B) PyTTA-BFDMTDC COF, (C) BATPDA-BFTDC COF, and (D) BATPDA-BFDMTDC COF.

In order to further estimate the separation of COFs towards CO_2. We also measured the breakthrough curve (**Figure 6**) of PyTTA-*m*-TPDC 1D COF. The CO_2 selectivity was investigated via column breakthrough tests using binary CO_2/CH_4:20/80 and CO_2/N_2:20/80 gas mixtures at 298 K and atmospheric pressure. These mixtures mimic natural gas upgrading and post-combustion capture applications, respectively. [11,18,19] Remarkably, PyTTA-*m*-TPDC 1D COF showed a high selectivity, as CO_2 was retained for longer times (6.4 minutes versus ~4 minutes for CO_2/CH_4 and 9.4 minutes versus ~3 minutes for CO_2/N_2) under continuous and kinetic flowing gas conditions. These findings show that when CO_2-containing mixtures are in contact with PyTTA-*m*-TPDC 1D COF, CO_2 adsorbs more strongly and faster than N_2 and CH_4, thus occupying all the available space and sorption sites and consequently excluding other gases. [20]

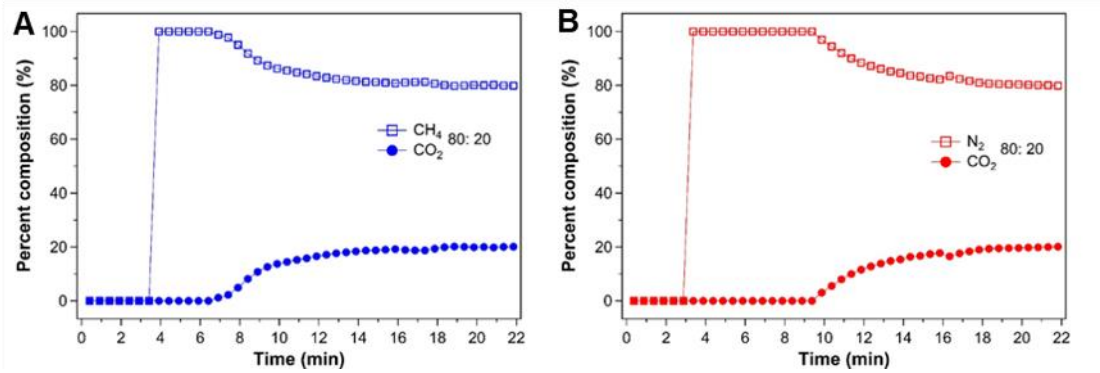

Figure 6. Breakthrough curves of PyTTA-*m*-TPDC 1D COF for mixtures of (a) N_2 and CO_2 (80:20); (b) CH_4 and CO_2 (80:20) at 298 K.

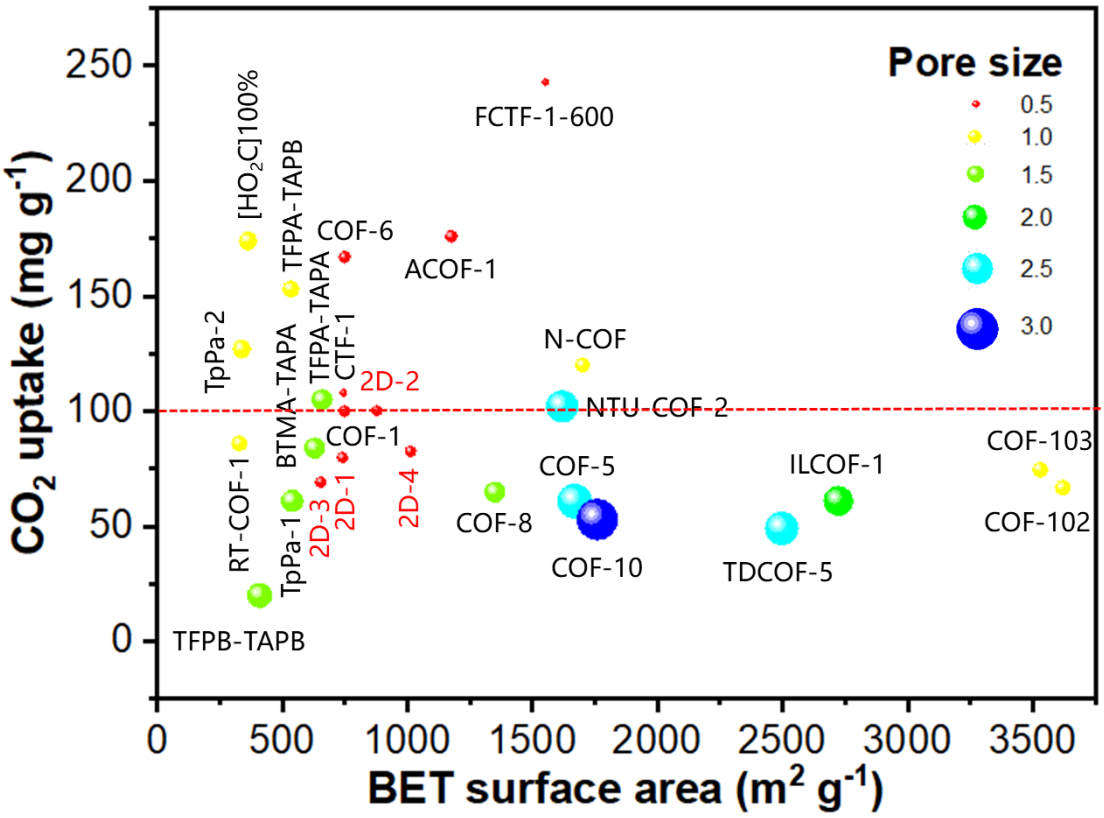

Figure 7. CO_2 uptake comparison between 2D [4 + 4] COFs and other reported COFs (2D-1: PyTTA-BFTDC COF, 2D-2: PyTTA-BFDMTDC COF, 2D-3: BATPDA-BFTDC COF, 2D-4: BATPDA-BFDMTDC COF, COF-1, [21] COF-5, [21] COF-6, [21] COF-8, [21] COF-10, [21] COF-102, [21] COF-103, [21] TDCOF-5, [22] CTF-1, [23] FCTF-1-600, [23] TpPa-1, [24] TpPa-2, [24] [HO_2C]100%, [25] TFPB-TAPB-COF, [26] TFPA-TAPB-COF, [26] BTMA-TAPA-COF, [26] TFPA-TAPA-COF, [26] ACOF-1, [27] N-COF, [28] ILCOF-1, [29] RT-COF-1, [30] NTU-COF-2 [31]).

CO_2 is a significant contributor to global warming, and new technologies and new materials are required to reduce CO_2 emissions to ease the effect of climate change. [32]

Porous materials such as zeolite, MOF and activated carbon have been studied extensively for CO_2 capture. [33] However, the wide pore size distribution, poor stability and sensitivity towards humid conditions, renders these porous materials unsuitable for CO_2 capture. [34] Owing to their inherent ordered pores and designable porous structure, COFs are promising for gas storage like CO_2. In addition, COFs is immune to highly polar gases such as water due to the lack of unsaturated metal ions. Among various COFs, microporous COFs are better candidates to achieve a high CO_2 uptake. Moreover, creating interface on the pore walls by various functional groups that can interact with CO_2 is a promising way to enhance the capacity. In this chapter, we estimate the CO_2 capture performance of 2D [4 + 4] COFs and 1D COFs and analyse the relationship between the performance and the structural properties such as surface area and crystal size. The high capacity, selectivity and separation demonstrate the prospect of these COFs for CO_2 capture applications.

Recent computational and experimental studies for a range of functionalised MOFs and COFs predicted that functional group modification would increase the amount of CO_2 captured by the network. [35] Moreover, polar groups such as carboxylic acid are effective in increasing CO_2 capture, while bulky non-polar groups such as methyl groups have a negative impact. [36] Nevertheless, some researches suggest the methyl groups not only can increase the stability and porosity without decreasing the pore size, but also strengthen CO_2–aromatic interactions due to their electron-donating nature. [16] However, there are scant reports on the use of microporous 2D COFs decorated by materials and 1D COFs as adsorbent for CO_2 capture and separation.

In this chapter, we determined the relationship between CO_2 capture of 2D [4 + 4] COFs with the pore volume, pore size, surface area and crystal size. After decorating methyl groups, the pore size and pore volume doesn't change obviously but the BET surface area is much increased, indicating methyl groups have little impact on the pore structure but produce more microporous site and defect, which are also consistent with the result of *t*-plot and mean crystal size that methyl group decorated COFs have a larger micropore contribution and smaller crystal size compared with their counterparts. These 2D [4 + 4] COFs achieved high CO_2 capacity, better than those of other reported COFs

such as COF-1, COF-5, COF-8 and COF-10. Especially, the CO_2 capacity of PyTTA-BFDMTDC 2D COF can reach 100 mg g^{-1}. The much-enhanced CO_2 capacity and selectivity over N_2 of methyl group decorated COFs may attributed to the increased BET surface area as well as the interaction between CO_2 and methyl groups. This is corresponded with the reported experimental and computational results that electron-donate nature of methyl groups can induce and strengthen the interaction between the aromatic ring and CO_2. Despite similar conclusion has been obtained in MOFs, it's first time to demonstrate the effect and potential of methyl group for CO_2 capture in COFs. Besides, we checked the separation capacity of 1D COFs. The breakthrough tests show that 1D COFs for example PyTTA-*m*-TPDC 1D COF can selectively adsorb CO_2 from the mixture with N_2 and CH_4, indicating their promising potential of natural gas upgrading and post-combustion capture applications. However, different from other crystalline materials such as MOFs, it is hard to synthesize single-crystal COFs to fully deconvolute the effects of other factors such as morphology, amorphous phase and defects.

5. Brief summary

In conclusion, for the first time, the system of 2D [4 + 4] COFs and 1D COFs offers an ideal platform for CO_2 capture and separation. We show here that methyl groups not only increase BET surface area by producing more micropores and defects, but also induce the induced extra interaction, which dictates the CO_2 uptake for 2D [4 + 4] COFs at low pressures (1 atm). The high microporosity of PyTTA-*m*-TPDC 1D COF renders a good potential of CO_2 separation. We hope this strategy and finding will be helpful to promote the application of COFs in gas storage and separation.

References

1. Chu, S. *Science* **2009**, *325*, 1599.
2. Li, J. R.; Sculley, J.; Zhou, H. C. *Chem. Rev.* **2012**, *112*, 869.
3. Morris, R. E.; Wheatley, P. S. *Angew. Chem. Int. Ed.* **2018**, *47*, 4966.

4. Zeng, Y.; Zou, R.; Zhao, Y. *Adv. Mater.* **2016**, *28*, 2855.
5. Nagai, A.; Guo, Z.; Feng, X.; Jin, S.; Chen, X.; Ding, X.; Jiang, D. *Nat*. *Commun*. **2011**, *2*, 536.
6. Du, L.; Lu, Z.; Xu, L.; Ma, M.; Zhang, J. *Eur. J. Inorg. Chem.* **2016**, *29*, 4727.
7. Bessinger, D.; Ascherl, L.; Auras, F.; Bein, T. *J. Am. Chem. Soc.* **2017**, *139*, 12035.
8. Schwab, M. G.; Hamburger, M.; Feng, X.; Shu, J.; Spiess, H. W.; Wang, X.; Antonietti, M.; Müllen, K. *Chem. Commun.* **2010**, *46*, 8932.
9. Altarawneh, S.; Behera, S.; Jena, P.; El-Kaderi, H. M. *Chem. Commun.* **2014**, *50*, 3571.
10. Giacalone, F.; Campisciano, V.; Calabrese, C.; Parola, V. L.; Syrgiannis, Z.; Prato, M.; Gruttadauria, M. *ACS Nano* **2016**, *10*, 4627.
11. Nugent, P.; Belmabkhout, Y.; Burd, S. D.; Cairns, A. J.; Luebke, R.; Forrest, K.; Pham, T.; Ma, S.; Space, B.; Wojtas, L.; Eddaoudi, M.; Zaworotko, M. J. *Nature* **2013**, *495*, 80.
12. Wang, H.; Cao, H.; Zheng, J.; Mathew, S.; Hosono, N.; Zhou, B.; Lyu, H.; Kusaka, S.; Jin, W.; Kitagawa, S.; Duan, J. *Chem. Eur. J.* **2018**, *24*, 6412.
13. Holzwarth, U.; Gibson, N. *Nat. Nanotechnol.* **2011**, *6*, 534.
14. Miranda, M. A. R.; Sasaki, J. M. *Acta Cryst.* **2018**, *A74*, 54.
15. Wang, C.; Li, L.; Tang, S.; Zhao, X. *ACS Appl. Mater. Interfaces* **2014**, *6*, 16932.
16. Torrisi, A.; Mellot-Draznieks, C.; Bell, R. G. *J. Chem. Phys.* **2009**, *130*, 194703.
17. Burtch, N. C.; Jasuja, H.; Dubbeldam, D.; Walton, K. S. *J. Am. Chem. Soc.* **2013**, *135*, 7172
18. Coromina, H. M.; Walsh, D. A.; Mokaya, R. *J. Mater. Chem. A* **2016**, *4*, 280.
19. Yang, Q.; Wiersum, A. D.; Llewellyn, P. L.; Guillerm, V.; Serre, C.; Maurin, G. *Chem. Commun.* **2011**, *47*, 9603.
20. Duan, J.; Higuchi, M.; Horike, S.; Foo, M. L.; Rao, K. P.; Inubushi, Y.; Fukushima T.; Kitagawa, S. *Adv. Funct. Mater.* **2013**, *23*, 3525.
21. Furukawa, H.; Yaghi, O. M. *J. Am. Chem. Soc.* **2009**, *131*, 8875.
22. Kahveci, Z.; Islamoglu, T.; Shar, G. A.; Ding, R.; El-Kaderi, H. M. *CrystEngComm* **2013**, *15*, 1524.
23. Zhao, Y.; Yao, K. X.; Teng, B.; Zhang, T.; Han, Y. *Energy Environ. Sci.* **2013**, *6*, 3684.
24. Kandambeth, S.; Mallick, A.; Lukose, B.; Mane, M. V.; Heine, T.; Banerjee, R. *J. Am. Chem. Soc.* **2012**, *134*, 19524.

25. Huang, N. Chen, X.; Krishna, R.; Jiang, D. *Angew. Chem. Int. Ed.* **2015**, *54*, 2986.
26. Zhai, L.; Huang, N.; Xu, H.; Chen, Q.; Jiang, D. *Chem. Commun.* **2017**, *53*, 4242.
27. Li, Z.; Feng, X.; Zou, Y.; Zhang, Y.; Xia, H.; Liu, X.; Mu, Y. *Chem. Commun.* **2014**, *50*, 13825.
28. Gao, Q.; Bai, L.; Zhang, X.; Wang, P.; Li, P.; Zeng, Y.; Zou, R.; Zhao, Y. *Chin. J. Chem.* **2015**, *33*, 90.
29. Rabbani, M. G.; Sekizkardes, A. K.; Kahveci, Z.; Reich, T. E.; Ding, R.; El-Kaderi, H. M. *Chem. Eur. J.* **2013**, *19*, 3324.
30. de la Pena Ruigomez, A.; Rodriguez-San-Miguel, D.; Stylianou, K. C.; Cavallini, M.; Gentili, D.; Liscio, F.; Milita, S. Roscioni, O. M.; Ruiz-Gonzalez, M. L.; Carbonell, C.; Maspoch, D.; Mas-Balleste, R.; Segura, J. L.; Zamora, F. *Chem. Eur. J.* **2015**, *21*, 10666.
31. Zeng, Y.; Zou, R.; Luo, Z.; Zhang, H.; Yao, X.; Ma, X.; Zou, R.; Zhao, Y. *J. Am. Chem. Soc.* **2015**, *137*, 1020.
32. Haszeldine, R. S. *Science* **2009**, *325*, 1647.
33. D'Alessandro, D. M.; Smit, B.; Long, J. R. *Angew. Chem. Int. Ed.* **2010***, 49*, 6058.
34. Morris, R. E.; Wheatley, P. S. *Angew. Chem. Int. Ed.* **2018**, *47*, 4966.
35. Wilmer, C. E.; Farha, O. K.; Bae, Y. S.; Hupp, J. T.; Snurr, R. Q. *Energy Environ. Sci.* **2012**, *5*, 9849
36. Torrisi, A.; Bell R. G.; Mellot-Draznieks, C. *Cryst. Growth Des.* **2010**, *10*, 2839.

Chapter IV: N,P Co-Doped Porous Carbons Derived from Two-Dimensional Covalent Organic Frameworks for Oxygen Reduction Reaction and Hydrogen Evolution Reaction

Abstract

In Chapter III, 2D COFs with differernt structures were synthesized. In this chapter, in order to utilize the designalibity of introducing heteroatoms and overcome the drawback of low conductivity, a series of metal-free, porous, and N,P co-doped carbon catalysts were facilely prepared from high crystalline 2D COFs. Remarkably, the COF derived N,P co-doped carbon catalysts exhibit excellent tolerances towards methanol crossover, as well as comparable oxygen reduction reaction (ORR) and hydrogen evolution reaction (HER) performances to commercial Pt/C.

1. Introduction

COFs are a class of crystalline porous materials. [1,2] They have been paid much attention on gas storage, catalysts, molecular sieve, and so on because of their large specific areas, high crystallinities and adjustable pore sizes. [3-6] More importantly, diverse active heteroatoms such as B and N and functional groups can be easily designed and incorporated into the skeleton or poral surface of COFs. [7,8] Therefore, COFs have been investigated as catalysts for energy conversion, like carbon dioxide reduction reaction. [9] However, the intrinsically poor conductivities and relative lower content of heteroatoms in most of COFs will result in limited activities of oxygen reduction reaction (ORR) and hydrogen evolution reaction (HER). [10]

Inspired by the excellent electroconductivities and unique properties of heteroatom doped carbon materials, thermally pyrolyzing COFs, followed by heteroatom co-doping, would be a rational way for creating highly efficient and metal-free electrocatalysts. As a precursor, the regular and large pore of COFs are

more preferred, where the heteroatoms can diffuse into the framework in fast and uniform manner. Moreover, as second heteroatoms like P, they can not only bring additional surface defects for enhanced edge effect, but also can stabilize C-N species, [11] modulating the electronic properties and surface polarities to further increase electrochemical activity by co-doping. [12,13] In addition, unlike the strategy of adding extra organic phosphor sources before or after the formation of COFs, [14,15] thermal-assistant phosphorization process ensures the original crystallinity and porosity to the maximum extent before post treatment and avoids the complicated influence of other elements in organic phosphor sources during the calcination, beneficial to produce carbon catalysts with improved activities.

2. Experimental section

2.1 Synthesis

1,3,5-tri-(4-aminophenyl)benzene (TAPB) and DMTA were purchased from TCI. Other required chemicals were Sigma-Aldrich and Aladdin. All chemicals were used as received without any further purification.

2.1.1 Synthesis of TAPB-DMTA COF and other 2D COFs

2.1.1.1 TAPB-DMTA COF

TAPB (14.0 mg), DMTA (11.7 mg), o-dichlorobenzene/n-BuOH (0.5/0.5 ml) and acetic-acid (6 M, 0.1 ml) were put in a Pyrex tube (10 ml). The tubes were evacuated by three freeze–pump–thaw cycles, flame sealed and heated at 120 °C for three days. The precipitate was filtered, washed with THF and then extracted in a Soxhlet with THF for 24 h.

2.1.1.2 PyTTA-BFTDC COF

A Pyrex tube measuring 10 × 8 mm (o.d × i.d) was charged with PyTTA (11.5 mg, 0.02 mmol), BFTDC (9.9 mg, 0.02 mmol), mesitylene (0.48 mL), dioxane (0.32 mL), and 6 M aqueous acetic acid (0.08 mL). The tube was flash frozen at in liquid N_2 bath for three freeze-pump-thaw cycles and flame sealed. The reaction was heated at 120 ºC for 120

hours yielding a yellow precipitate at the bottom of the tube, which was isolated by filtration with THF. The wet sample was then transferred to a Soxhlet extractor and thoroughly washed with THF for 48 h and dried under vaccum at 100 ºC for 6 h.

2.1.1.3 PyTTA-BFDMTDC COF

The synthesis was carried out following the same protocol as for PyTTA-BFTDC COF, by replacing BFTDC with BFDMTDC (10.5 mg, 0.02 mmol) and changing the amount of mesitylene and dioxane to 0.60 mL/0.30 mL.

2.1.1.4 BATPDA-BFTDC COF

The synthesis was carried out following the same protocol as for PyTTA-BFTDC COF, by replacing PyTTA with BATPDA (8.8 mg, 0.02 mmol) and changing the amount of mesitylene and dioxane to 0.60 mL/0.30 mL.

2.1.1.5 BATPDA-BFDMTDC COF

The synthesis was carried out following the same protocol as for PyTTA-BFTDC COF, by replacing PyTTA with BATPDA (8.8 mg, 0.02 mmol), *m*-TPDC with BFDMTDC (10.5 mg, 0.02 mmol) and changing the amount of mesitylene and dioxane to 0.4 mL/0.4 mL.

2.1.2 Synthesis of COF derived N doped carbon

20.0 mg TAPB-DMTA COF, PyTTA-BFTDC COF, PyTTA-BFDMTDC COF, BATPDA-BFTDC COF or BATPDA-BFDMTDC COF, respectively were calcinated in Ar at 1000 °C with a rate of 3 °C min^{-1} and keep it for another 2 h, named as TAPB-DMTA-N-C, PyTTA-BFTDC-N-C, PyTTA-BFDMTDC-N-C, BATPDA-BFTDC-N-C and BATPDA-BFDMTDC-N-C, respectively.

2.1.3 Synthesis of COF derived N,P co-doped carbon

10.0 mg COF derived N doped carbon (TAPB-DMTA-N-C, PyTTA-BFTDC-N-C, PyTTA-BFDMTDC-N-C, BATPDA-BFTDC-N-C and BATPDA-BFDMTDC-N-C) and 270 mg Na_2HPO_2 are placed at two porcelains. NaH_2PO_2 at the upstream side of the furnace. Subsequently, the samples were heated at 400°C for 4 h with a heating speed of 10 °C min^{-1} in Ar atmosphere. The product was filtered, washed with water and dried at 120 °C under vacuum overnight, named as TAPB-DMTA-N,P-C, PyTTA-BFTDC-N,P-C, PyTTA-BFDMTDC-N,P-C, BATPDA-BFTDC-N,P-C and BATPDA-BFDMTDC-N,P-C, respectively.

2.2 Electrochemical test

All electrocatalytic measurements were carried out in a three-electrode cell at ambient conditions. A graphite rod and Ag/AgCl (saturated KCl) were used as the counter and reference electrode, respectively. A catalyst-loaded glassy carbon electrode was used as the working electrode. The catalyst suspensions were prepared by ultrasonically dispersing 5.0 mg of catalysts in 1.0 mL of mixture solution of isopropanol and H_2O (1:4, v/v) and 40 μL of 5% Nafion solution. Ar or O_2 was blown into 0.10 M KOH or 1 M $HClO_4$ for at least 0.5 h to ensure the Ar, O_2-saturated solution for ORR and HER. Then a certain volume of catalyst suspension was pipetted onto the surface of working electrode (rotating disk electrode (RDE) with a diameter of 5 mm and rotating ring-disk electrode (RRDE) with a ring diameter of 5 mm/7mm and a disk diameter of 4 mm) to give a 0.20 mg cm^{-2} loading for all samples. The cyclic voltammetry (CV) profiles for ORR were obtained in Ar- or O_2-saturated 0.10 M KOH solution with a scan rate of 20 mV s^{-1}. RDE tests were performed with a sweep rate of 10 mV s^{-1}. RRDE tests for ORR were performed with a sweep rate of 10 mV s^{-1} at a rotation speed of 1600 rpm. Chronoamperometric tests for ORR without methanol were conducted in O_2-saturated 0.10 M KOH solution at 0.40 V vs. RHE at a rotation speed of 400 rpm. The tests of methanol tolerance for ORR were measured in O_2-saturated 0.10 M KOH solution at 0.60 V vs. RHE at a rotation speed of 1600 rpm by adding the certain amount of methanol at 100 s (~3.4 mL methanol into 80 mL 0.10 M

KOH). All the electrochemical measurements were performed at room temperature. The electron transfer numbers of the oxygen reduction reaction (ORR) were determined from the slopes of the linear lines according to the following K–L equation (1):

$$\frac{1}{j} = \frac{1}{j_k} + \frac{1}{j_L} = \frac{1}{j_k} + \left(\frac{1}{0.2nFD_0^{2/3}\nu^{-1/6}C_0}\right)\omega^{-1/2} \quad (1)$$

where j, j_L, and j_K are the measured current density and diffusion- and kinetic-limiting current densities, respectively; ω is the rotation rate (rpm), n is the electron transfer number, F is the Faraday constant (96485 C mol^{-1}), D_0 is the diffusion coefficient of O_2 (1.9×10^{-5} cm^2 s^{-1} in 0.10 M KOH), v is the kinematic viscosity of the electrolyte (0.01 cm^2 s^{-1}), C_0 is the bulk concentration of O_2 (1.2×10^{-6} mol cm^{-3}).

For the RRDE measurements, the percentage of intermediate production ($\%HO_2^-$) and the electron transfer number (n) were determined by the following equations (2 and 3):

$$\%HO_2^- = 200\frac{I_r/N}{I_d + I_r/N} \quad (2)$$

$$n = 4\frac{I_d}{I_d + I_r/N} \quad (3)$$

where I_d is the disk current, I_r is the ring current, and the N is the current collection efficiency of the Pt ring, which is determined to be 0.37. The areas of the ring and disk in RRDE and the disk in RDE are 18.85 cm^{-2}, 12.57 cm^{-2}, and 19.63 cm^{-2}, respectively.

For HER stability, CV measurements were conducted for 10000 cycles in the region from -0.2 V to 0.2 V vs. RHE under rotating at 1,600 rpm.

3. Characterization

Powder X-ray diffraction (PXRD) data were recorded on a Rigaku model RINT Ultima III diffractometer by depositing powder on glass substrate with 0.02° increment. Nitrogen sorption isotherms were measured at 77 K with a 3 Flex analyzer. Before measurement, the samples were degassed in vacuum at 120 °C for more than 10 h. The Brunauer-Emmett-Teller (BET) method was utilized to calculate the specific surface areas. By using the quenched solid state functional theory (QSDFT) slit/cylindr./sphere pore model, the pore size was derived from the sorption curve. X-ray photoelectron spectroscopy (XPS)

experiments were carried out on an AXIS Ultra DLD system from Kratos with Al K_α radiation as X-ray source for radiation. Raman spectra were recorded on a SEN TERRA spectrometer (Bruker) employing a semiconductor laser (λ = 532 nm). High resolution transmission electron microscope (HR-TEM) images, scanning transmission electron microscope (STEM) and energy-dispersive X-ray spectroscopy (EDS) mappings were obtained by JEOL JEM-ARM200F TEM.

We performed Pawley refinement to optimize the lattice parameters iteratively until the R_{wp} value converges. The pseudo-Voigt profile function was used for whole profile fitting and Berrar–Baldinozzi function was used for asymmetry correction during the refinement processes. The crystalline structures were determined using the density-functional tight-binding (DFTB+) method including Lennard-Jones (LJ) dispersion implemented in Materials Studio version 8.0 (Accelrys). The Coulombic interaction between partial atomic charges was determined using the self-consistent charge formalism. Lennard-Jones-type dispersion was employed in all calculations to describe van der Waals and π-stacking interactions. The lattice dimensions were optimized simultaneously with the geometry. Standard DFTB parameters for X–Y element pair (X, Y = C, O, H, F and N) interactions were employed from the mio-0-1 set and halorg set.

4. Results and discussions

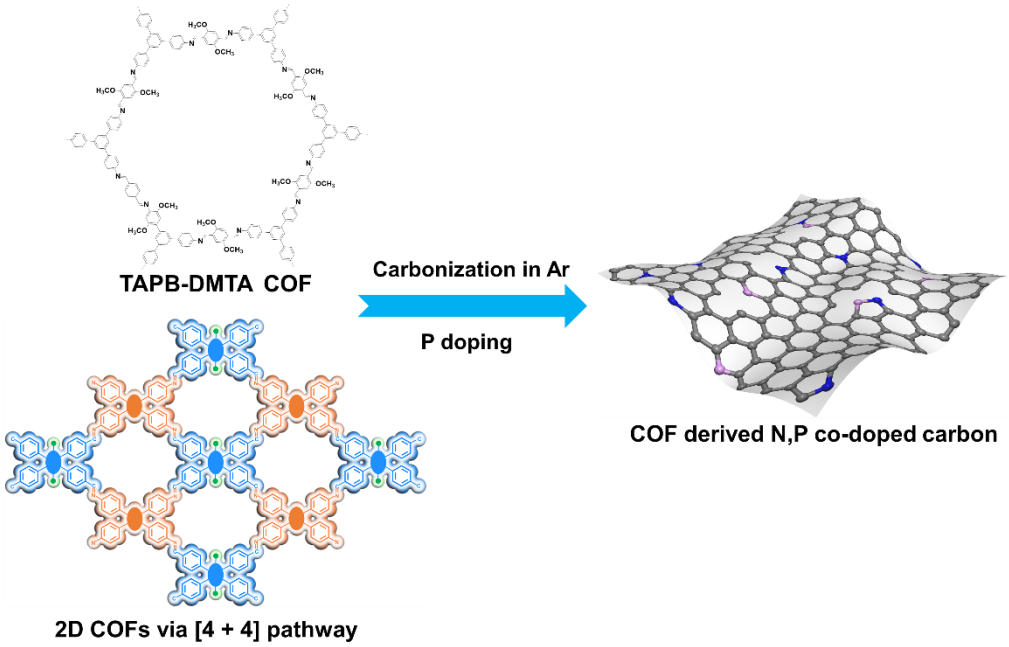

Figure 1. Fabrication process of 2D COF derived N,P co-doped carbon.

We develop N,P co-doped porous carbon catalysts from various 2D COFs including TAPB-DMTA COF and COFs via a [4 + 4] pathway introduced in Chapter II. As shown in **Figure 1**, 2D COFs were synthesized and then used as a precursor to be annealed in Ar at 1000 °C for 2 h to form COF derived N doped carbon, followed by a phosphorization process by reacting with NaH_2PO_2 as the phosphor source at 400 °C for 4 h to form COF derived N,P co-doped carbon. The COF derived N,P co-doped carbon exhibits robust and comparable ORR and HER performances to Pt/C. These results demonstrate the promising prospect of metal-free catalysts based on 2D COFs by co-doping.

Firstly, TAPB-DMTA COF was synthesized according to previous report. [16] As we can see, **Figure 2A** displays the crystalline structure (a = b = 42.9 Å and c = 4.4 Å) of the obtained TAPB-DMTA COF based on space group: P6. A set of strong PXRD peaks of TAPB-DMTA COF with an eclipsed structure at 2.7°, 4.8°, 5.6° and 7.4° in **Figure 2B**, corresponding to (1 0 0), (1 1 0), (2 0 0) and (1 2 0), respectively, demonstrate the high crystallinity of TAPB-DMTA COF. The Pawley refined PXRD pattern is also in good agreement with the experimental result with low R_{wp} and R_p values of 8.72% and 14.37%. The high porosity of the obtained TAPB-DMTA COF is evaluated by N_2 adsorption type IV

isotherm (**Figure 2C**), where the BET surface area and pore size (**Figure 2D**) is calculated as 2067 $m^2 g^{-1}$ and 3.3 nm.

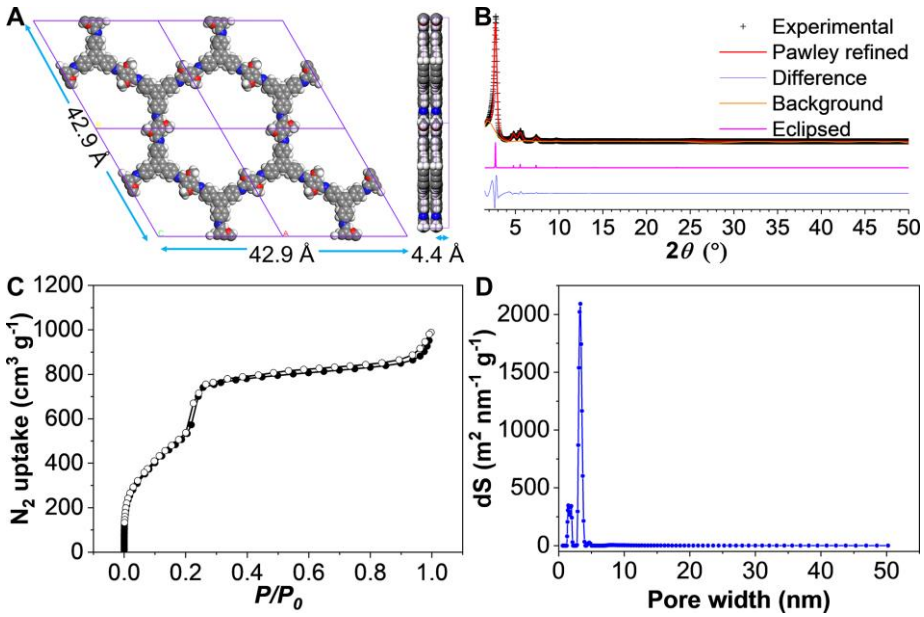

Figure 2. (A) Top view and side view of the crystalline structure, (B) PXRD pattern and Pawley refined result, (C) N_2 adsorption isotherm curve and (D) corresponding pore size distribution for TAPB-DMTA COF.

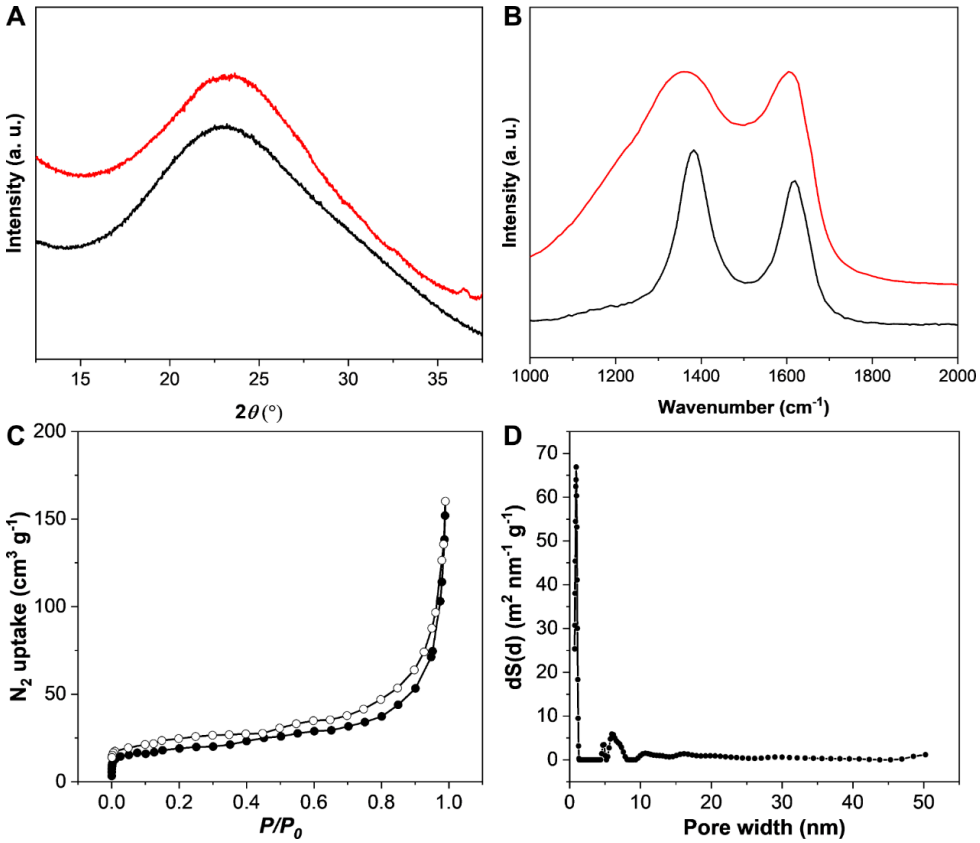

Figure 3. (A) PXRD patterns and (B) Raman spectra of TAPB-DMTA-N-C (black curves) and TAPB-DMTA-N,P-C (red curves); (C) N_2 adsorption isotherm curve and (D) corresponding pore size distribution for TAPB-DMTA-N,P-C.

When TAPB-DMTA COF was used as a precursor, TAPB-DMTA-N-C and TAPB-DMTA-N,P-C were obtained via carbonization and following phosphorization. The PXRD peak (**Figure 3A**) at ~23° from the diffraction of (0 0 2) graphitic carbon planes, suggests the presence of long-range order in TAPB-DMTA-N-C and TAPB-DMTA-N,P-C. [17] Raman spectra in **Figure 3B** show that the intensity ratios (I_D/I_G) of D band (1359 cm^{-1}) to G band (1604 cm^{-1}) for TAPB-DMTA-N,P-C is 1.20, which is higher than that of TAPB-DMTA-N-C (0.99), revealing a lower graphitization degree and more defects due to the introducing of P. [11,18] The BET specific surface area and the corresponding pore size of TAPB-DMTA-N,P-C are determined by N_2 adsorption–desorption analysis as 67 m^2 g^{-1} and 0.80 nm (**Figure 3C** and **Figure 3D**). The porous structure of TAPB-DMTA-N,P-C can also be investigated by high-resolution transmission electron microscope (HRTEM) in **Figure 4A** and **Figure 4B**. Furthermore, from the HRTEM image in **Figure 4B,** the crystalline lattice in local ordered carbon of around 0.38 is corresponded well to the (0 0 2) facets of the graphite, which is consistent with the result of PXRD patterns. Energ-dispersive X-ray spectroscopy (EDS) mappings in **Figure 4C** also confirm the uniform distribution of N and P in TAPB-DMTA-N,P-C.

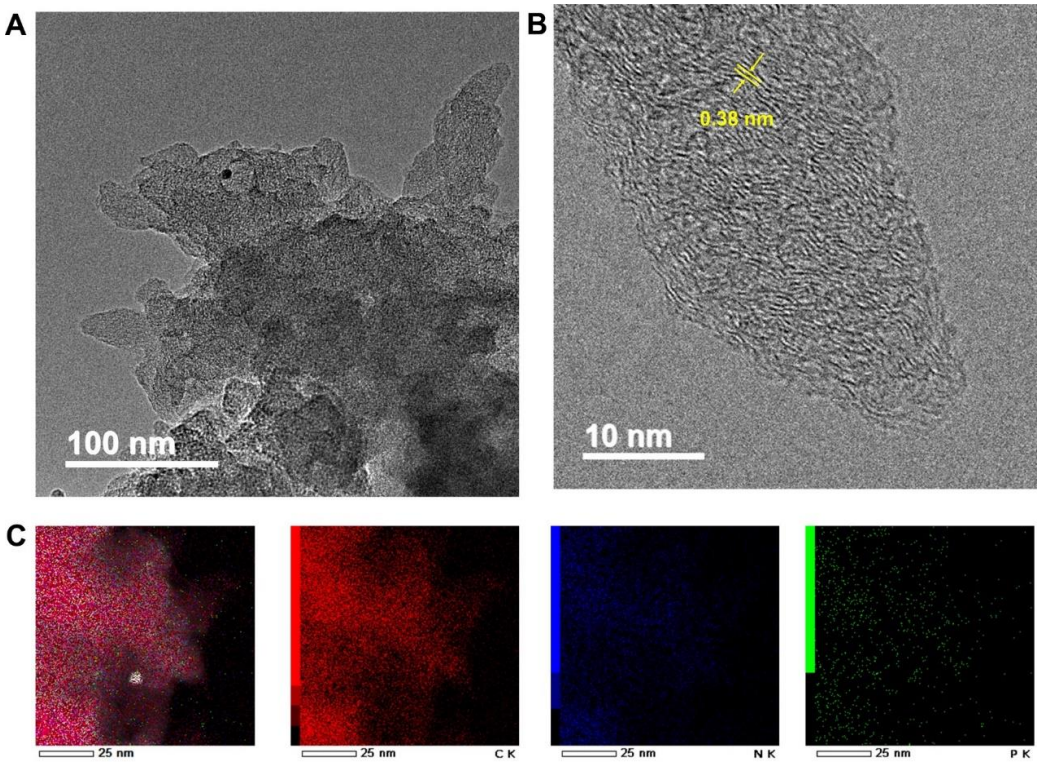

Figure 4. (A), (B) HRTEM images and (C) EDS mappings of TAPB-DMTA-N,P-C.

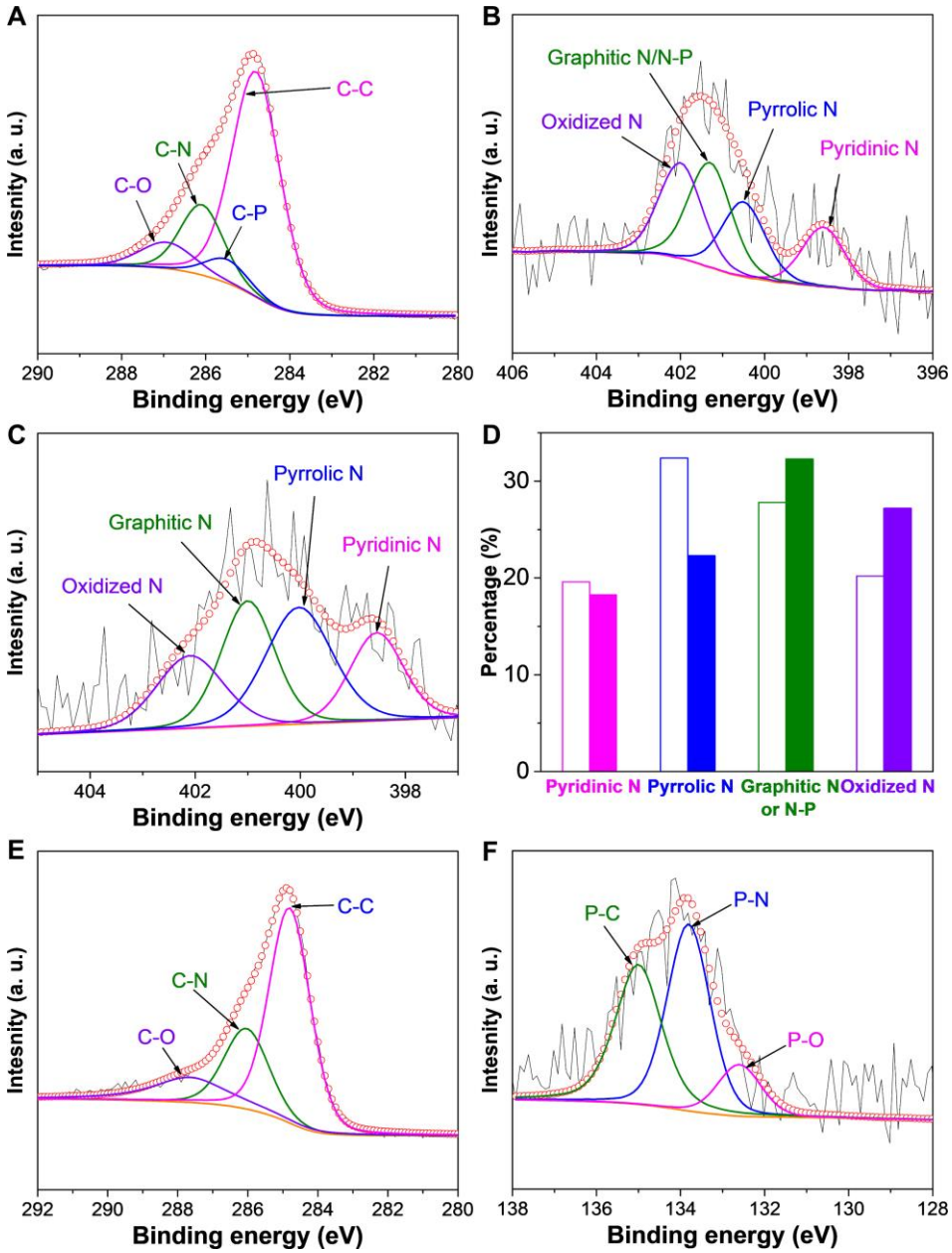

Figure 5. XPS spectra of (A) C 1s, (B) N 1s and (F) P 2p for TAPB-DMTA-N,P-C; XPS spectrum of N 1s (C) and C 1s (E) for TAPB-DMTA-N-C; (D) Normalized ratios of various nitrogen types in TAPB-DMTA-N,P-C and TAPB-DMTA-N-C from the XPS results (Unfilled patterns is for TAPB-DMTA-N-C and filled patterns is for TAPB-DMTA-N,P-C).

In **Figure 5A**, the X-ray photoelectron spectrum (XPS) C 1s spectrum for TAPB-DMTA-N,P-C can be deconvoluted into four different bands at 284.8, 285.5, 286.2 and 287.3 eV, which correspond to C-C, C-P, C-N and C-O, respectively. [19] This indicates the most of oxygen-contained groups are thermal reduced and P is doped into the skeleton successfully. Typical XPS N 1s for TAPB-DMTA-N,P-C is provided in **Figure 5B**. As we can see, pyridinic (398.6 eV), pyrrolic (400.5 eV), graphitic (and N-P) (401.3 eV) and oxidized pyridinic (402.0 eV) N all exists. [20,21] The high ratio of pyridinic and pyrrolic N make TAPB-

DMTA-N,P-C effictive towards ORR. [22,23] Moreover, the normalized ratios (**Figure 5D**) of pyridinic (18.3%) and pyrrolic N (22.3%) are a little lower, while the normalized ratios of graphitic (and N-P) (32.3%) and oxidized pyridinic N (27.2%) are higher than those (19.6%, 32.4%, 27.8% and 20.2%, respectively) of TAPB-DMTA-N-C (**Figure 5C**). The increased ratio of graphitic N (and N-P) suggests P bonds with N successfully. Furthermore, the decreased ratios of pyridinic and pyrrolic N are attributed to the fact that P prefers to bond with pyridinic and pyrrolic N apart from C and the low residual O (**Figure 5E**). In the high-resolution P 2p spectrum of TAPB-DMTA-N,P-C (**Figure 5F**), besides P-C and P-O bonding at 132.6 eV and 134.6 eV, the band at 133.6 eV reveals the formation of P-N, [24] which is consistent to the result of XPS N 1s. Therefore, the local order crystalline structures, microposity and rich defective sites, likely make TAPB-DMTA-N,P-C highly conductive, facilitative to the diffusion of reactants, and more active as a brilliant electrocatalyst.

We evaluate the ORR performance of TAPB-DMTA-N,P-C by linear sweep voltammetry (LSV). In **Figure 6A**, TAPB-DMTA-N,P-C exhibits a remarkable ORR activity, as displayed by the onset potential (~0.87 V vs. RHE) and the diffusion-limiting current density (~5.6 mA cm^{-2} at 0.40 V vs. RHE), comparable to those (~0.94 V vs. RHE and ~4.7 mA cm^{-2}) of Pt/C. Moreover, the half-wave potential of TAPB-DMTA-N,P-C from the LSV curve can reach 0.81 V (vs. RHE), which is only 40 mV more negative than that of Pt/C (0.85 V vs. RHE). By contrast, TAPB-DMTA-N-C exhibits a much lower ORR performance (an onset potential of ~0.69 V vs. RHE, a diffusion-limiting current density of ~2.2 mA cm^{-2} and a half-wave potential of 0.64 V vs. RHE). The much enhanced ORR activity of TAPB-DMTA-N,P-C is ascribed to more active sites after phosphorization. The formation of P-C and P-N results in the strong synergistic effect of N,P co-doping that the overpotential of N,P co-doping carbon is even smaller than that of Pt. [11] The electrocatalytic activity of TAPB-DMTA-N,P-C is also confirmed by the well-defined cathodic peak at 0.82 V vs. RHE in O_2-saturated 0.10 M KOH solution compared with Ar-saturated solution using cyclic voltammetry (CV) measurements (**Figure 6B**). In addition, LSV curves after

subtracting the background under Ar (**Figure 6C** and **Figure 6D**) in **Figure 6E** show a good linearity. From the correponding Koutecky–Levich (K–L) plot (**Figure 6F**), the electron transfer number (*n*) of TAPB-DMTA-N,P-C is calculated as around 4.0 (Equation (1)). A

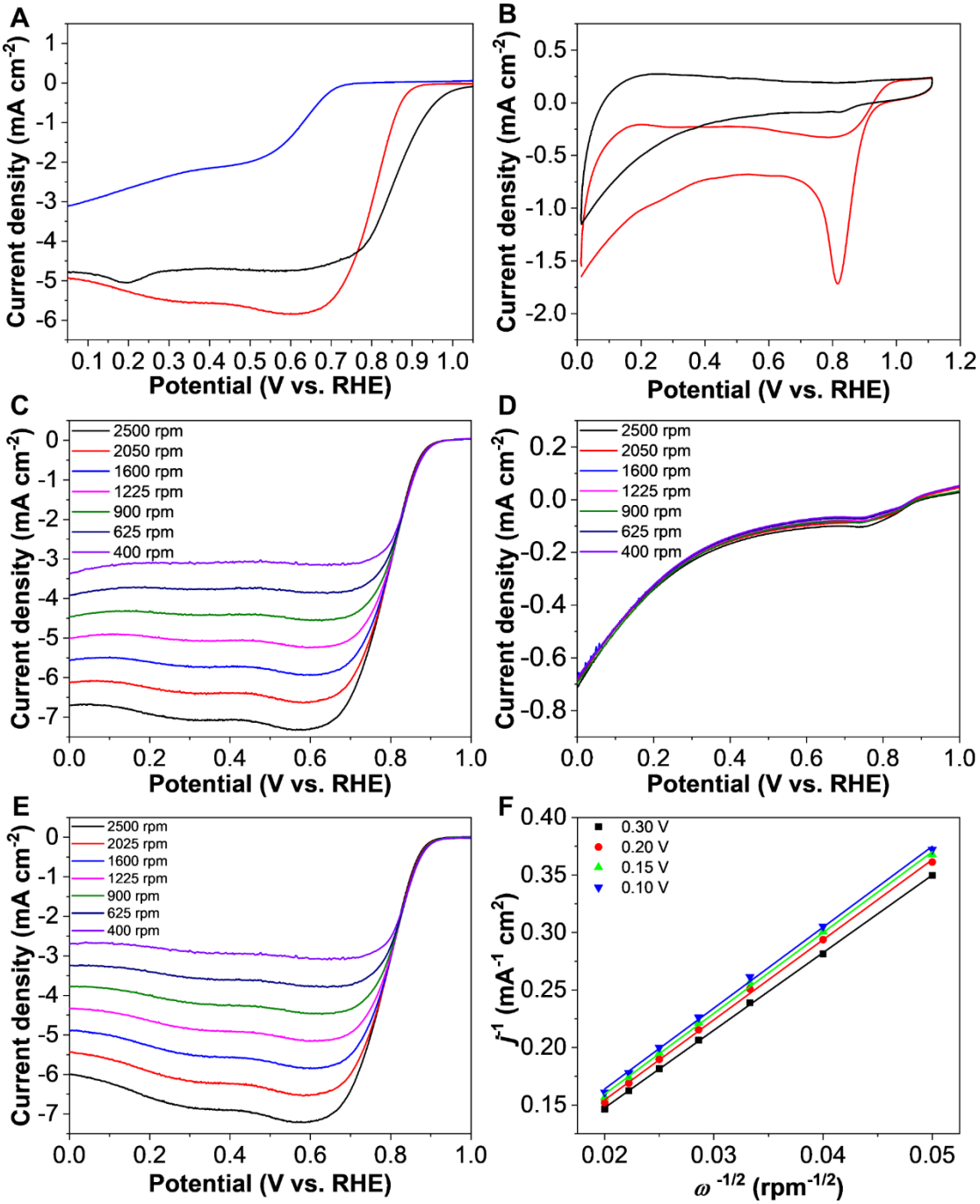

Figure 6. (A) LSV curves of TAPB-DMTA-N-C (blue), TAPB-DMTA-N,P-C (red) and Pt/C (black) at a rotation speed of 1600 rpm, respectively; (B) CV curves under O_2 (red) and Ar (black), (C) LSV curves before subtracting the background under Ar at various rotation speeds, (D) background under Ar at various rotation speeds, (E) LSV curves after subtracting the background under Ar at various rotation speeds and (F) K−L plots for TAPB-DMTA-N,P-C.

rotating ring-disk electrode (RRDE) technique is futher employed to monitor the amount of H_2O_2 generated during the ORR process. In **Figure 7A**, TAPB-DMTA-N,P-C shows a high limited current density from ORR, whereas the current density associated with H_2O_2 oxidation obtained on the Pt-ring is below 20% (Equation (2) and **Figure 7B**). The corresponding values for *n* (Equation (3)) calculated from RRDE voltammograms (**Figure 7C**) are between 3.45 and 3.95 in the range from 0 V to 0.80 V, in accordance with the corresponding data obtained from the K–L plot in **Figure 6F**, suggesting a four-electron

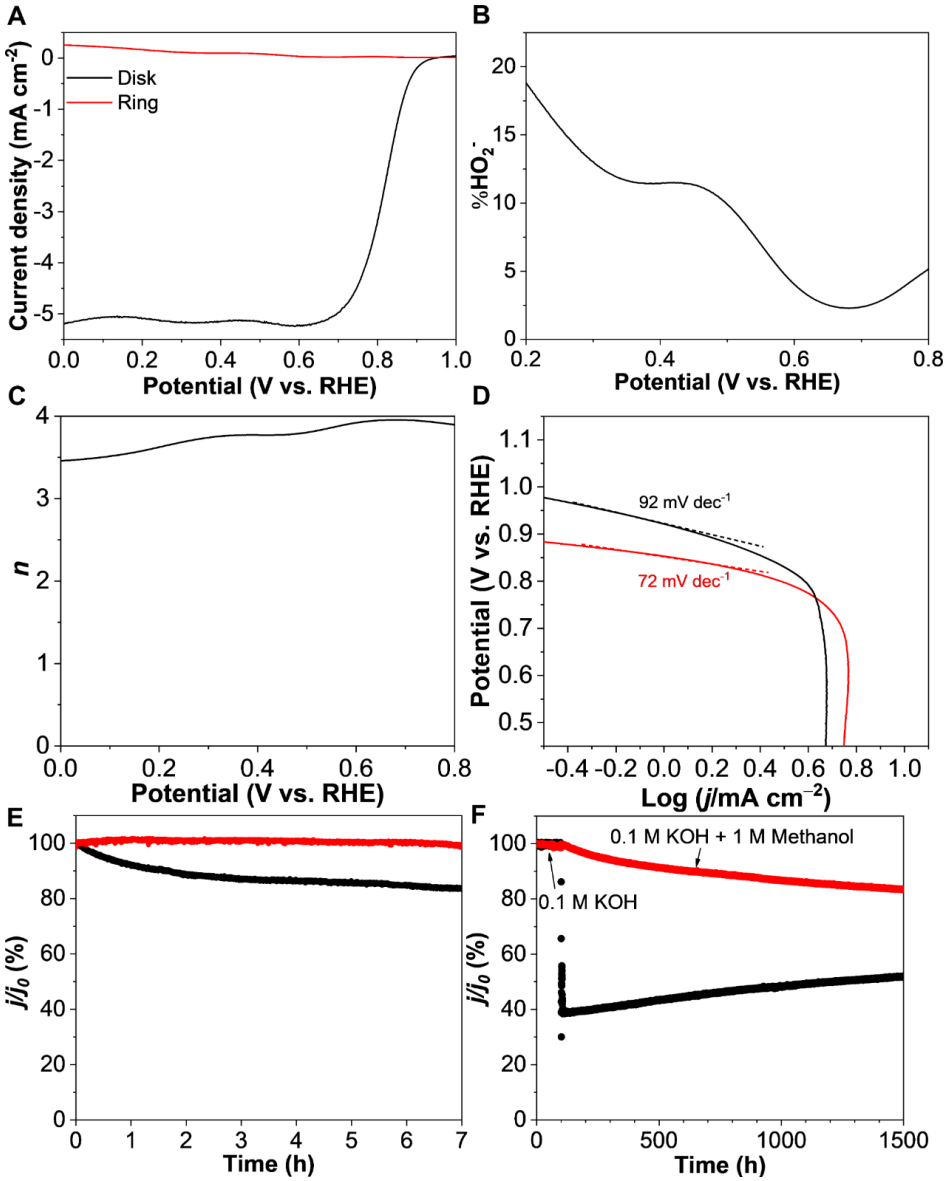

Figure 7. (A) RRDE curves at a rotation speed of 1600 rpm, (B) Peroxide percentage ($\%HO_2^-$) as a function of the electrode potential at 1600 rpm and (C) The corresponding *n* as a function of the electrode potential for TAPB-DMTA-N,P-C; (D) Corresponding Tafel plots, (E) Chronoamperometric profiles and (F) responses after injecting methanol of TAPB-DMTA-N,P-C (red curves) and Pt/C (black curves).

pathway for ORR. The smaller Tafel slope (72 mV dec^{-1}) than that of Pt/C (92 mV dec^{-1}) (**Figure 7D**) once again certifies the excellent ORR activity of TAPB-DMTA-N,P-C. In addition, TAPB-DMTA-N,P-C also demonstrates an excellent durability. As shown in **Figure 7E**, TAPB-DMTA-N,P-C can maintain a higher current retention of 99% after 7 h of continuous operation compared with Pt/C (88%). More importantly, TAPB-DMTA-N,P-C exhibits a remarkable tolerance towards methanol crossover. When injecting methanol into the electrolyte, no obvious disturbance of the current can be observed for TAPB-DMTA-N,P-C (**Figure 7F**). By comparison, the current for commercial Pt/C catalyst has a significant decrease to 38%. After 1500 s, the current density of TAPB-DMTA-N,P-C remains 83%, better than that Pt/C catalyst (53%). This indicates a good immunity of TAPB-DMTA-N,P-C towards methanol crossover as a promising metal-free electrocatalyst for direct methanol fuel cells.

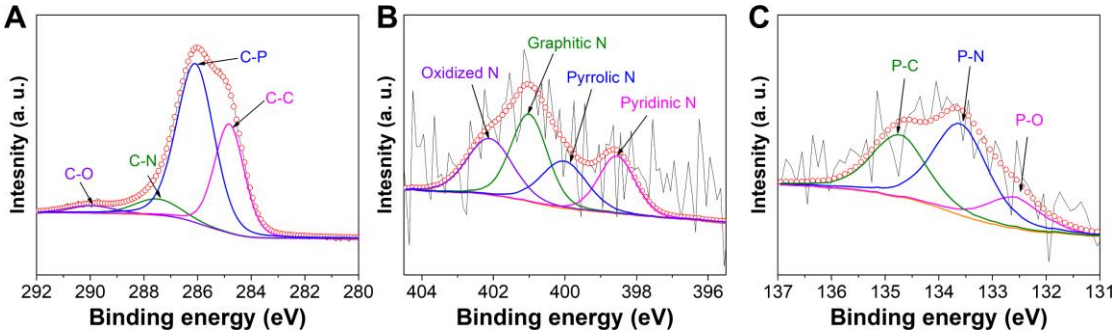

Figure 8. XPS spectra of (A) C 1s, (B) N 1s and (D) P 2p for PyTTA-BFTDC-N,P-C.

We also syntheized PyTTA-BFTDC-N,P-C, PyTTA-BFDMTDC-N,P-C, BATPDA-BFTDC-N,P-C and BATPDA-BFDMTDC-N,P-C using PyTTA-BFTDC COF, PyTTA-BFDMTDC COF, BATPDA-BFTDC COF and BATPDA-BFDMTDC COF as precursors, respectively, in the same way. PyTTA-BFTDC-N,P-C was taken as an typical example. C-P and C-N at 285.5 and 286.2 eV in XPS C 1s spectrum (**Figure 8A**) as well as P-C and P-N in XPS P 2p spectrum (**Figure 8C**) confirmed the successful doping of N and P. XPS N 1s for PyTTA-BFTDC-N,P-C provided in **Figure 8B** also can be deconvoluted into four bands (pyridinic (398.6 eV), pyrrolic (400.5 eV), graphitic (and N-P) (401.3 eV) and oxidized pyridinic (402.0 eV) N). Moreover, The ratio of pyridinic and pyrrolic N (~20%) for PyTTA-BFTDC-N,P-C is close to those of TAPB-DMTA-N,P-C.

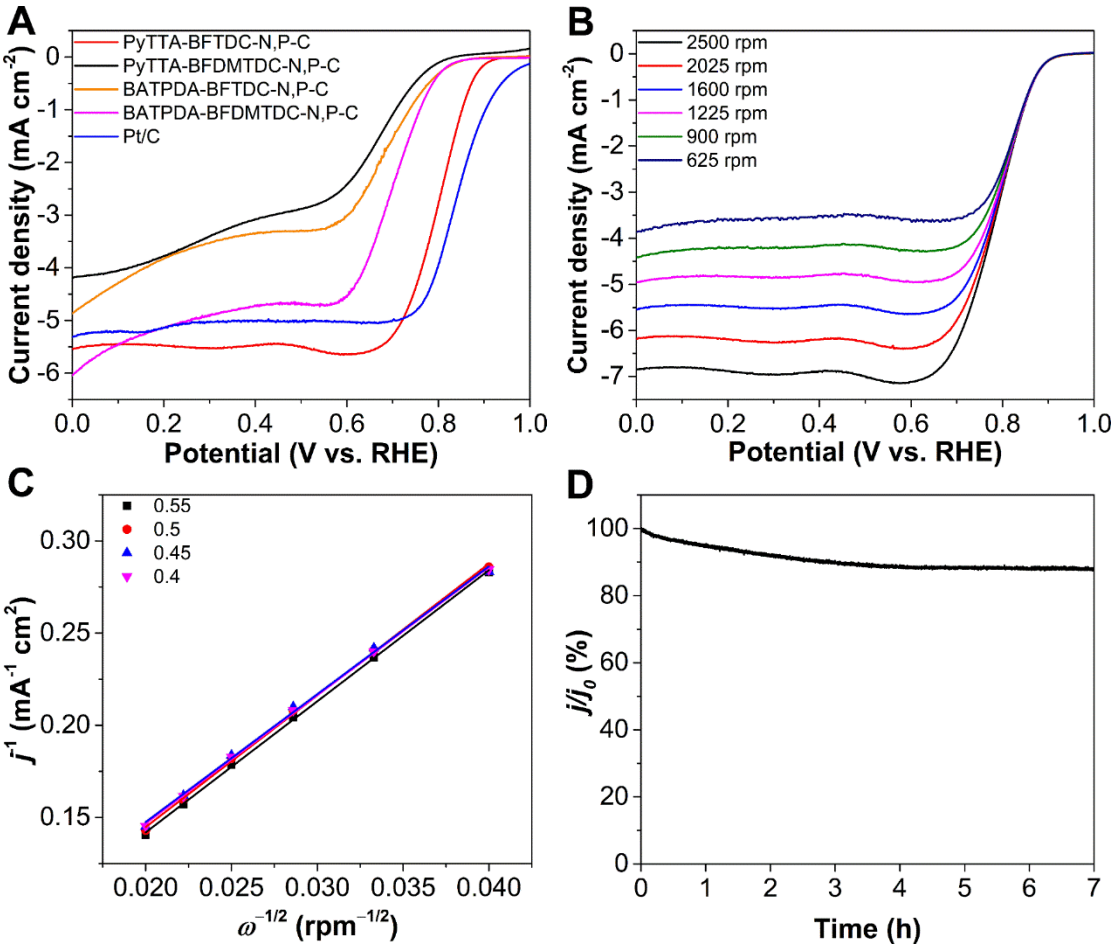

Figure 9. (A) Comparison of LSV curves at a rotation speed of 1600 rpm; (B) LSV curves at various rotation speeds, (C) the corresponding K−L plots and (D) chronoamperometric profiles of PyTTA-BFTDC-N,P-C.

The ORR performances of PyTTA-BFTDC-N,P-C, PyTTA-BFDMTDC-N,P-C, BATPDA-BFTDC-N,P-C and BATPDA-BFDMTDC-N,P-C were evaluated by LSV. In **Figure 9A**, PyTTA-BFTDC-N,P-C exhibits the best ORR activity among them, as displayed by the onset potential (~0.88 V vs. RHE) and the diffusion-limiting current density (~5.5 mA cm^{-2} at 0.30 V vs. RHE), comparable to those (~0.92 V vs. RHE and ~5.0 mA cm^{-2}) of Pt/C. Moreover, the half-wave potential of PyTTA-BFTDC-N,P-C from the LSV curve can reach 0.81 V (vs. RHE), which is only 20 mV more negative than that of Pt/C (0.83 V vs. RHE). By contrast, PyTTA-BFDMTDC-N,P-C, BATPDA-BFTDC-N,P-C and BATPDA-BFDMTDC-N,P-C exhibit much lower ORR performances with half-wave potentials of 0.67 V, 0.68 V and 0.70 V vs. RHE, respectively. An increased current with increasing rotation speed was observed. (**Figure 9B**). In addition, LSV curves in **Figure 9C** show a good

linearity. From the correponding Koutecky–Levich (K–L) plot (**Figure 9C**), the electron transfer number (*n*) of PyTTA-BFTDC-N,P-C is calculated as around 4.0, suggesting a four-electron pathway for ORR. **Figure 9D** shows only 12% current reduction for PyTTA-BFTDC-N,P-C catalyst after a 7 h chronoamperometric test, indicating high ORR stability.

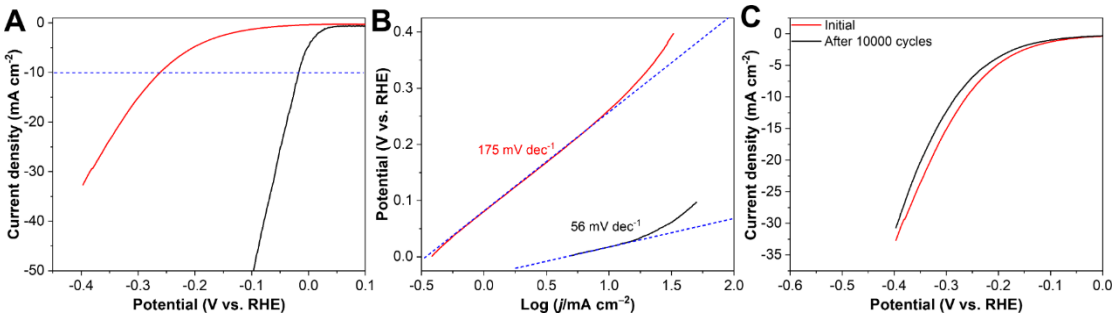

Figure 10. (A) The polarization curves and (B) Corresponding Tafel plots of PyTTA-BFTDC-N,P-C (red) and Pt/C (black); (C) LSV curves of PyTTA-BFTDC-N,P-C before and after 10000 CV cycles.

Besides the good ORR performance, PyTTA-BFTDC-N,P-C displays a high HER activity in acid solution. As displayed in **Figure 10A**, an impressive HER activity (η≈260 mV) is attained for PyTTA-BFTDC-N,P-C at the current density of 10 mA cm^{-2}. This overpotential is much lower than that of metal-free catalysts recently reported in acid media (**Table 2**). Moreover, PyTTA-BFTDC-N,P-C presents a low Tafel slope of ≈175 mV dec^{-1} (**Figure 10B**). Furthermore, the durability test (**Figure 10C**) shows that the polarization curve of PyTTA-BFTDC-N,P-C in acidic conditions exhibits no obvious shift after 10000 CV cycles, indicating it is stable in acidic electrolyte.

These results reveal N,P co-doped porous carbon derived from 2D COFs is one of the best previously reported metal-free catalysts even superior to some metal-based catalysts (**Table 1** and **2**). The much enhanced ORR and HER activity with a long-term stability of N,P co-doped carbon catalyst is ascribed to more active sites after phosphorization. N doping the conductuve graphtic carbon converted from thermally stable framework of COFs leads to more electrons attracted toward the N-doped section due to the electronegativity of N is larger than that of C, enhancing the electronic/ionic conductivity of N-doped carbon. [25] By contrast, strong hybridization between P and C gives rise to structural distortion, decreased conductivity but defects. [26] The formation of N-C, P-C and P-N results in the strong synergistic effect of N,P co-doping by generating more "C^{+}"

centers. [27] P doping not only brings additional surface defects for enhanced edge effect, but also can stabilize C-N species, helpful to increase the stability. [24] Theoretical analysis also indicates the ORR catalytic mechanism of N,P co-doped carbon. Density functional theory (DFT) methods reveal that the minimum overpotential of N,P co-doped carbon for ORR is even smaller than that of Pt. [11] And the density of state (DOS) demonstrates the DOS near Fermi level of N-P-C is obviously stronger than N-C, bonding with HOO*. [28] We anticipate that our method and result will also be useful for other COF derived co-doped carbon catalysts.

Table 1. The ORR performance comparison of metal-free and metal-carbon catalysts in O_2-saturated aqueous 0.1 M KOH solutions at a rate constant of 1600 rpm.

Catalysts	Half-wave potential (V)	Diffusion-limiting current density (mA cm^{-2})	References
TAPB-DMTA-N,P-C	**0.81 (vs. RHE)**	**5.7 (at 0.4 V vs. RHE)**	**This work**
PyTTA-BFTDC-N,P-C	**0.81 (vs. RHE)**	**5.5 (at 0.4 V vs. RHE)**	**This work**
C-COP-4	0.78 (vs. RHE)	~5.5 (at 0.4 V vs. RHE)	*Adv. Mater.* **2014**, *26*, 3315.
NPMC-1000	0.85 (vs. RHE)	~4.5 (at 0.4 V vs. RHE)	*Nat. Nanotechnol.* **2015**, *10*, 444.
PA@TAPT-DHTACOF$_{1000NH3}$	0.87 (vs. RHE)	7.2 (at 0 V vs. Ag/AgCl)	*Adv. Mater.* **2018**, *30*, 1706330.
MPSA/GO-1000	<0.80 (vs. RHE)	< 5.0	*Angew. Chem. Int. Ed.* **2016**, *55*, 2230.
N-S-G	<-0.3 V (vs. Ag/AgCl)	N/A	*Angew. Chem. Int. Ed.* **2012**, ***51***, 11496.
M-CMP2-800	<-0.14 V (vs. Ag/AgCl)	5.4 (at -0.6 V vs. RHE)	*Angew. Chem. Int. Ed.* **2016**, *55*, 6858.
N-HsGDY-900 °C	0.85 (vs. RHE)	6.2 (at 0.2 V vs. RHE)	*Nat. Commun.* **2018**, *9*, 3376.
h-Mn_3O_4-TMSLs	0.84 (vs. RHE)	5.7 (at 0.2 V vs. RHE)	*J. Am. Chem. Soc.* **2017**, *139*, 12133.
Mo–N/C@MoS_2	0.81 (vs. RHE)	5.3 (at 0 V vs. RHE)	*Adv. Funct. Mater.* **2017**, *27*, 1702300.
S,N-Fe/N/C-CNT	0.85 (vs. RHE)	6.67 (at 0.2 V vs. RHE)	*Angew. Chem. Int. Ed.* **2017**, *56*, 610.
Fe-TA-800	<0.80(vs. RHE)	~5.5 (at 0.2 V vs. RHE)	*Angew. Chem. Int. Ed.* **2016**, *55*, 1.
Co_3O_4/rmGO	0.83 (vs. RHE)	~5.0 (at 0.4V vs. RHE)	*Nat. Mater.* **2011**, *10*, 780.
N-CNTs-650	0.85 (vs. RHE)	~5.0 (at 0.4V vs. RHE)	*J. Am. Chem. Soc.* **2017**, *139*, *8212.*

Table 2 The overpotential (vs. RHE at 10 mA cm^{-2}) comparison of metal-free and metal-carbon catalysts in acid mediums.

Catalysts	Overpotential (mV)	References
PyTTA-BFTDC-N,P-C	**260 (1 M $HClO_4$)**	**This work**
MPSA/GO-1000	~200 (0.5 M H_2SO_4)	*Angew. Chem.* **2016**, *128*, 2270.
1T-MoS_2 sheets	187 (0.5 M H_2SO_4)	*J. Am. Chem. Soc.* **2013**, *135*, 10274.
N,P-doped graphene	420 (0.5 M H_2SO_4)	*ACS Nano* **2014**, *8*, 5290.
C_3N_4@N-doped graphene	240 (0.5 M H_2SO_4)	*Nature Commun.* **2014**, *5*, 3783.
g-C_3N_4 nanoribbons on graphene sheets	207 (0.5 M H_2SO_4)	*Angew. Chem. Int. Ed.* **2014**, *53*, 13934.
CoP/CNT	226 (0.5 M H_2SO_4)	*Angew. Chem. Int. Ed.* **2014**, *53*, 6710.
NS co-doped graphene 500C	276 (0.5 M H_2SO_4)	*Angew. Chem. Int. Ed.* **2015**, *54*, 2131.

5. Brief summary

In summary, a new kind of porous and metal-free N,P co-doped carbon via carbonizing and phosphorizing was facilely prepared. The comparable and robust ORR/HER performance as well as the good methanol tolerance make COF derived N,P co-doped carbon a promising candidate of ORR/HER catalysts. It also may be a harbinger for broad applicability of this methodology for synthesizing various metal-free electrocatalysts based on co-doped COF-derived carbon.

References

1. Diercks, C. S.; Yaghi, O. M.; *Science* **2017**, *355*, eaal1585.
2. Ding, S.; Wang, W.; *Chem. Soc. Rev.* **2013**, *42*, 548.
3. Feng, X.; Ding X.; Jiang, D. *Chem. Soc. Rev.* **2012**, *41*, 6010.
4. Lin, S.; Diercks, C. S.; Zhang, Y.-B.; Kornienko, N.; Nichols, E. M.; Zhao, Y.; Paris, A. R.; Kim, D.; Yang, P.; Yaghi, O. M.; Chang, C. J. *Science* **2015**, *349*, 1208.

5. Kandambeth, S.; Biswal, B. P.; Chaudhari, H. D.; Rout, K. C.; Kunjattu, S.; Mitra, H. S.; Karak, S.; Das, A.; Mukherjee, R.; Kharul, U. K.; Banerjee, R. *Adv. Mater.* **2017**, *29*, 1603945.
6. Zou, C. C.; Li, Q. Q.; Hua, Y. Y.; Zhou, B. H.; Duan J. G.; Jin, W. Q. *ACS Appl. Mater. Interfaces* **2017**, *9*, 29093.
7. Nath, B.; Li, W.-H.; Huang, J.-H.; Wang, G.-E.; Fu, Z.-h.; Yao M.-S.; Xu, G. *CrystEngComm* **2016**, *18*, 4259.
8. Lin, C.-Y.; Zhang, D.; Zhao, Z.; Xia, Z. *Adv. Mater.* **2018**, *30*, 1703646.
9. Côté, A. P.; Benin, A. I.; Ockwig, N. W.; O'Keeffe, M.; Matzger, A. J.; Yaghi, O. M. *Science* **2005**, *310*, 1166.
10. Xiang, Z.; Cao, D.; Huang, L.; Shui, J.; Wang M.; Dai, L. *Adv. Mater.* **2014**, *26*, 3315.
11. Zhang, J.; Zhao, Z.; Xia, Z.; Dai, L. *Nat. Nanotechnol.* **2015**, *10*, 444.
12. Liang, J.; Jiao, Y.; Jaroniec, M.; Qiao, S. Z. *Angew. Chem. Int. Ed.* **2012**, *51*, 11496.
13. Zhang, J.; Qu, L.; Shi, G.; Liu, J.; Chen, J.; Dai, L. *Angew. Chem. Int. Ed.* **2016**, *55*, 2230.
14. Xu, Q.; Tang, Y.; Zhang, X.; Oshima, Y.; Chen Q.; Jiang, D. *Adv. Mater.* **2018**, *30*, 1706330.
15. Li, Z.; Zhao, W.; Yin, C.; Wei, L.; Wu, W.; Hu, Z.; Wu, M. *ACS Appl. Mater. Interfaces* **2017**, *9*, 44519.
16. Xu, H.; Gao J.; Jiang, D. *Nat. Chem.* **2015**, *7*, 905.
17. Tang, J.; Salunkhe, R. R.; Liu, J.; Torad, N. L.; Imura, M.; Furukawa S.; Yamauchi, Y. *J. Am. Chem. Soc.* **2015**, *137*, 1572.
18. Zan, Y.; Zhang, Z.; Liu, H.; Dou M.; Wang, F. *J. Mater. Chem. A* **2017**, *5*, 24329.
19. Wang, Z.; Li, P.; Chen, Y.; He, J.; Liu, J.; Zhang W.; Li, Y. *J. Power Sources* **2014**, *263*, 246.
20. Yang, C.; Chen, Z.; Shakir, I.; Xu Y.; Lu, H. *Nano Res.* **2016**, *9*, 951.
21. Wang, C.; Sun, L.; Zhou, Y.; Wan, P.; Zhang X.; Qiu, J. *Carbon* **2013**, *59*, 537.
22. Guo, D.; Shibuya, R.; Akiba, C.; Saji, S.; Kondo T.; Nakamura, J. *Science* **2016**, *351*, 361.

23. Lv, Q.; Si, W.; He, J.; Sun, L.; Zhang, C.; Wang, N.; Yang, Z.; Li, X.; Wang, X.; Deng, W.; Long, Y.; Huang C.; Li, Y. *Nat. Commun.* **2018**, *9*, 3376.
24. Chai, G.-L.; Qiu, K.; Qiao, M.; Titirici, M.-M.; Shang C.; Guo, Z. *Energy Environ. Sci.* **2017**, *10*, 1186.
25. Asefa, T. *Acc. Chem. Res.* **2016**, *49*, 1873.
26. Wang, X.; Sun, G.; Routh, P.; Kim, D.-H.; Huang, W.; Chen, P. *Chem. Soc. Rev.* **2014**, *43*, 7067.
27. Gong, K. P.; Du, F.; Xia, Z. H.; Durstock, M.; Dai, L. M. *Science* **2009**, *323*, 760.
28. Gao, J.; He, C.; Liu, J.; Ren, P.; Lu, H.; Feng, J.; Zou, Z.; Yin, Z.; Wen, X.; Tan, X. *Catal. Sci. Technol.* **2018**, *8*, 1142.

Chapter V: Summary and Perspectives

In chapter I, I summarized the chemical science of porous materials mainly COFs developed in recent years. I illustrated the design principle of COFs based on topology diagram, the synthetic method and applications of COF and COF-derived materials.

In chapter II, I designed and synthesized stable, crystalline, and microporous 2D COFs via [4 + 4] pathway. In addition, I first developed a series of 1D COFs with microporosity, high crystallinity, high stability based on the geometrical matching between V-type linkers and tetrahedral knots. The modification of linkers also achieves the introducing of heteroatoms, alkyl chains and aromatic groups into 1D COFs to realize their functionalization.

In chapter III, we used 2D [4 + 4] COFs and 1D COFs to capture and separate CO_2. Methyl group decorated COFs achieve an enhanced capture (100 mg g^{-1}) and separation (w/w, 26/1, CO_2 over N_2) of CO_2 at 1 atm and 273 K due to the increased microporosity and the strong affiliation between COFs and CO_2 induced by methyl groups. And 1D COFs also exhibit a good selectivity for CO_2 separation.

In chapter IV, I synthesized porous and metal-free N,P co-doped carbon via carbonizing and phosphorizing 2D [4 + 4] COFs and TAPB-DMTA COF. COF derived N,P co-doped carbons exhibit remarkable performances as ORR/HER electrocatalysts with the half-wave potential of 0.81 V vs. RHE in alkaline medium and overpotential of 260 mV at 10 mA cm^{-2} in acid medium.

In chapter V, I summarized the results of this work and show the perspectives of COF based materials.

Due to the large surface area, ordered pores and good stability, various COFs have been synthesized for CO_2 capture. Modifying COFs with “active” groups such as carboxyl groups and amine groups helps to build the interaction between functional groups and CO_2 to enhance the capacity. We found “inert” group such as electron-donating methyl group also can achieve it by increase van der Waals interactions.

Various 2D and 3D COFs have been designed and synthesized, but 1D COFs have not been reported. By considering the good geometric matching between linkers and knots, 1D COFs and functionalized 1D COFs have been synthesized successfully.

However, the conductivity of COFs is too poor to be utilized as electrocatalysts for ORR, HER and so on. Owing to the thermal stability and designable heteroatoms, COFs might be ideal precursors for metal-free carbon nanomaterials. By co doping with N and P, COF derived N,P co-doped carbon catalysts exhibit an excellent performance for ORR and HER.

Through the three-year research work, I have designed, synthesized and modified 1D and 2D COFs. They and their derived carbons have been applied in the field of gas storage and electrochemistry.

Since the structure of 1D COFs at atomic level is not very clear, the future work will be focused on synthesis of single-crystal 1D COFs or monolayered 1D COFs, from which the precise structure can be verified easily. Moreover, other heteroatom doped or co-doped carbons from 1D, 2D and 3D COFs will be explored to build a systematic relationship between the structure and electrochemical performance.

List of Publications

[1]. Designing Covalent Organic Frameworks from Two Dimension to One Dimension, 日本化学会北陸地区講演会と研究発表会. December 2017, Ishikawa, Japan, Style of Presentation: Poster.

[2]. Imine Bonded Covalent Frameworks Constructed by One-Dimensional Chains, The 98th CSJ (The Chemical Society of Japan) Annual Meeting. March 2018, Funabashi, Japan, Style of Presentation: Oral.

[3]. COF Derived N,P Co-Doped Carbon as a Metal-Free Catalyst for Highly Efficient Oxygen Reduction Reaction, the 4th International Symposium on Process Chemistry (ISPC 2019), July 2019, Kyoto, Japan, Style of Presentation: Poster.

[4]. N, P Co-Doped Carbons from 2D [4 + 4] Covalent Organic Frameworks as Bifunctional Electrocatalysts for Oxygen Reduction and Hydrogen Evolution Reactions, **Chao Yang**, Shanshan Tao, Ning Huang, Xiaobin Zhang, Jingui Duan,* Rie Makiura,* and Shinya Maenosono*. *ACS Appl. Mater. Interfaces* (Under review)

[5]. Design and Fabrication of One-Dimensional Covalent Organic Frameworks, **Chao Yang**, Shanshan Tao, Lipeng Zhai, Xianzhu Zhong, Xiaobin Zhang, Yoshifumi Oshima, Jingui Duan, Matthew A. Addicoat, Shinya Maenosono*. (Ready to submit)

[6]. COF derived N,P Co-Doped Carbon as a Metal-Free Catalyst for Highly Efficient Oxygen Reduction Reaction, **Chao Yang**, Shinya Maenosono, Jingui Duan*, Xiaobin Zhang. *ChemNanoMater* **2019**, *5*, 957-963.

[7]. 2D MOF-Derived Co@C Hybridized with Graphene as High-Performance Electrocatalysts for Zn-Air Batteries, **Chao Yang**, Haofan Wang, Wei Hong, Shinya Maenosono, Xiaobin Zhang, Qiang Xu*. (Ready to submit)

[8]. Recent Advances in Two-Dimensional Materials for Electrochemical Energy Storage and Conversion, **Chao Yang**, Qiang Xu*. *Flat Chem* (Ready to submit).

[9]. Co-N/C@MoS_2 Electrocatalysts for Oxygen Reduction Reaction and Zn-Air Batteries, **Chao Yang**, Shinya Maenosono, Xiaobin Zhang, Qiang Xu*. (In preparation).

Acknowledgements

I have been in Japan for almost three years since I came to Komatsu city in October, 2016. I wrote my thesis with a fully thankful heart. During the study and living at JASIT and Kyoto University, I received countless amounts of help and support from many peoples. Here, I express my thankfulness to them.

Firstly, I would like to thank my supervisors in JAIST, Prof. Donglin Jiang and Prof. Shinya Maenosono. Under their kind guidance, I have learned a lot of things. Since I entered JAIST, Prof. Jiang taught me how to design, synthesize, characterize organic molecules and COFs by himself. His encouragement and help make me to be familiar with and expert at organic systems since I focused on inorganic materials before.

After April 2018, I moved to Kyoto University to start a new research in AIST-Kyoto University, Chemical Energy Materials Open Innovation Laboratory (ChEM-OIL). I am very grateful for the supervision from Prof. Qiang Xu. He and the members of ChEM-OIL led me to enter the world of MOFs. I am deeply impressed on their serious-minded attitudes towards science.

I also owe my sincere gratitude to professors, my friends and my lab mates in JAIST, Prof. Yuki Nagao, Prof. Noriyoshi Matsumi, Dr. Xiaobin Zhang, Dr. Shanshan Tao, Dr. Ping Wang, Dr. Lipeng Zhai, Dr. Qing Xu, Dr. Sasanka Dalapati, Dr. Qiuhong Jiang, Mr. Zhongping Li, Mr. Zhanzhao Li, Mr. Weiming Jiang, Miss Yuan Zhao, Dr. Guangtao Wang, Prof. Yu Feng, Dr. Juan Li, Dr. Enquan Jin, for their kind help and encouragements in not only research but also everyday life. I will be grateful for the help in ChEM-OIL from Professor Jingui Duan, Dr. Wei Hong, Dr. Haofan Wang, Dr. Liyu Chen, Dr. Yongsheng Wei, Dr. Chunchao Hou, Dr. Gang Wang, Dr. Lu Zhai, Dr. Deshan Bian, Dr. Jinfa Chang, Miss Bing Li, Miss Ruo Zhao, Miss Xinran Li, Dr. Chih-Yao Chen, Dr. Osamu Yamada, Dr. Keigo Kubota, Dr. Tagashi Kajiwara, Dr. Miyuki Ikeda, Miss Makiko Sumino. I also acknowledge Dr. Matthew A. Addicoat in Nottingham Trent University for his help with the structural calculation. I am grateful to the help from Professor Rie Makiura in Osaka Prefecture

University, too.

I gratefully appreciate the scholarship of Chinese Scholarship Council (CSC) for supporting my study in Japan during the past three years.

Last but not least, I would like to thank my families for all their love, supports and encouragements. Especially I want to thank my wife and son. I can not persist until now without their understanding and accompanies.

Chao Yang

2019.09.20